Vol. 7 No. 2
October 2023

ISSN 2579-5821
e-ISSN 2579-5546

S3 sinta
Science and Technology Index

Jurnal Geocelebes

Published by:
Geophysics Department
Hasanuddin University
Makassar, Indonesia

JURNAL GEOCELEBES
Geophysics Department | Faculty of Mathematics and Natural Sciences | Hasanuddin University

Volume 7 Nomor 2, Oktober 2023

P-ISSN: 2579-5821
E-ISSN: 2579-5546

Diterbitkan oleh:
Departemen Geofisika, FMIPA
Universitas Hasanuddin

JURNAL GEOCELEBES
Volume 7 Nomor 2, Oktober 2023

ISSN: 2579 – 5821 (Cetak)
ISSN: 2579 – 5546 (Online)
Alamat URL: http://journal.unhas.ac.id/index.php/geocelebes

Diterbitkan berkala dua kali setahun oleh/ **Published periodically two times annually by**
Dept. Geofisika Universitas Hasanuddin/ **Geophysics Dept., Hasanuddin University**

Dewan Redaksi/ Editor Board

Sekretariat/ Secretariat:
Departemen Geofisika, FMIPA Universitas Hasanuddin
Gedung MIPA, Kampus Unhas Tamalanrea - Jalan Perintis Kemerdekaan, Makassar, Sulawesi Selatan, 90245.
E-mail: geocelebes@sci.unhas.ac.id

Jurnal Geocelebes adalah jurnal ilmiah yang diterbitkan oleh Departemen Geofisika Universitas Hasanuddin. Jurnal ini diperuntukkan sebagai sarana publikasi ilmiah di bidang geofisika mulai topik teoritik hingga topik topik aplikasi geofisika di berbagai bidang. Artikel yang dimuat merupakan hasil penelitian yang orisinal, tinjauan (*review*) tentang kemajuan terkini dari suatu topik tertentu, studi kasus aplikasi geofisika ataupun resensi tentang perangkat lunak yang berkaitan dengan geofisika. Makalah dapat dikirimkan ke alamat email redaksi dalam bentuk *softcopy* dengan menggunakan template yang telah disediakan. Setiap makalah yang diterima akan ditinjau kelayakannya melalui proses *reviewing* yang ketat oleh Dewan Redaksi.

DAFTAR ISI

JURNAL GEOCELEBES

Volume 7, Nomor 2, Oktober 2023

ISSN: 2579 – 5821 (Cetak)
ISSN: 2579 – 5546 (Online)

Alamat URL: http://journal.unhas.ac.id/index.php/geocelebes

KATA PENGANTAR

Jurnal Geocelebes yang dikelola oleh Departemen Geofisika, Fakultas Matematika dan Ilmu Pengetahuan Alam Universitas Hasanuddin Makassar telah memasuki tahun ke-tujuh. Dewan Redaksi mengucapkan syukur kepada Tuhan Yang Maha Esa atas pencapaian ini serta ungkapan terima kasih atas komitmen Tim Pengelola, Tim Editor Isi dan Layout, dalam menjalankan amanah ini. Secara khusus Dewan Redaksi mengucapkan terima kasih dan penghargaan setinggi-tingginya kepada seluruh penulis yang telah memasukkan karya ilmiahnya dan kepada Tim Mitra Bestari yang telah bersedia meluangkan waktu untuk memberikan saran dan koreksi yang membangun pada setiap artikel di setiap terbitan Jurnal Geocelebes.

Pada edisi Volume 7 Nomor 2 Oktober 2023 terdapat sepuluh artikel. Artikel yang diterbitkan yang secara umum membahas implementasi peran geosains khususnya geofisika dalam ekplorasi sumber daya alam dan bidang lainnya yang sesuai dengan fokus dan cakupan bidang yang diterbitkan oleh Jurnal Geocelebes. Bahasa yang digunakan pada volume ini dan kedepannya adalah Bahasa Inggris yang menunjukkan Jurnal Geocelebes layak menjadi jurnal internasional ke depannya. Jurnal Geocelebes menerima partisipasi dari akademisi, peneliti, praktisi industri, mahasiswa dan lainnya di bidang geosains baik dalam perspektif teoretik maupun aplikasi, baik yang berkaitan tentang bawah permukaan (litosfer) maupun atas permukaan (atmosfer), yang tentunya akan melalui serangkaian proses yaitu *submitting*, *editing*, dan *reviewing*.

Dewan Redaksi Jurnal Geocelebes membuka diri atas saran dan kritikan yang membangun demi perbaikan ke depan. Segala saran dan kritikan dapat dikirimkan melalui email geocelebes@sci.unhas.ac.id

Makassar, Oktober 2023

Dewan Redaksi Jurnal Gecelebes

ISSN: 2579-5821 (Print)
ISSN: 2579-5546 (Online)
URL address: http://journal.unhas.ac.id/index.php/geocelebes
DOI: 10.20956/geocelebes.v7i2.23710

Jurnal Geocelebes Vol. 7 No. 2, October 2023, 99 – 107

Determination of Seawater Intrusion Zones Using the Resistivity Method in Kelurahan Soreang, Maros District, South Sulawesi Province

Syamsuddin*, Muhammad Fajar, Andry Harmaji Wirawan, Nurul Salsabila, Rezky, Muhammad Fawzy Ismullah Massinai, Selfiana, Bambang Harimei

Geophysics Department, Mathematics and Natural Sciences Faculty, Hasanuddin University, Makassar, 90245, Indonesia

*Corresponding author. Email: syamsuddin@fmipa.unhas.ac.id

Manuscript received: 26 October 2022; Received in revised form: 26 May 2023; Accepted: 31 May 2023

Abstract

The seawater intrusion into the groundwater layer is one of the factors that can disrupt groundwater quality in Soreang Village, Maros Regency. This is a serious problem for the community in the area, so it is necessary to identify the seawater intrusion zone. Previous study using the resistivity method is in regional scale. In this study, two intersecting lines with a length of 470 meters each were acquired using the Wenner-Schlumberger array with a spacing of 10 meters to get local scale. Based on the resistivity value of the study area, there are three layers interpreted as a layer of fill (1 - 1000 Ωm), alluvium layer (1 - 6 Ωm) and limestone layer (≥ 7 Ωm). The seawater intrusion zone in the study area is in the alluvium layer with varying depths up to 40 meters subsurface. The results of this study can be a reference for the community or government in the search for fresh water.

Keywords: resistivity; seawater intrusion; Soreang; Wenner-Schlumberger.

Citation: Syamsuddin., Fajar, M., Wirawan, A. D., Salsabila, N., Rezky., Massinai, M. F. I., Selfiana. and Harimei, B. (2023). Determination of Seawater Intrusion Zones Using the Resistance Method in Kelurahan Soreang, Maros District, South Sulawesi Province. *Jurnal Geocelebes*, 7(2):99–107, doi: 10.20956/geocelebes.v7i2.23710

Introduction

The problem of fresh water availability in coastal areas is a crucial issue (Jeuken et al., 2017; Rahman et al., 2017; Huq, & Easher, 2021). This is the case faced by the community in Soreang Village, Maros Regency. This area is close to the coast and surrounded by river tributaries that are still influenced by tides. Communities around the area have difficulty obtaining a fresh water source, especially when entering the dry season, well water that was originally fresh becomes very salty. Therefore, a study was conducted with the aim to identify the area and depth of seawater intrusion that is expected to be anticipated by the community in Soreang Village, Maros Regency.

Geophysical methods are considered capable to address the problem. Identification of groundwater in coastal areas using the resistivity method has been carried out by Haroon et al. (2021) on the Maltese Island coast and Masciopinto et al. (2017) on the Bari coast. Both studies successfully identified the presence of freshwater. In South Sulawesi, similar research was conducted by Rahmaniah et al. (2021), but this research is considered too regional so it needs to be done more locally, especially in the Soreang Village area, Maros Regency.

The resistivity method is one of the geophysical methods used for subsurface investigations by utilizing the nature of electricity flow in the earth. This method includes measuring the potential difference and electric current that occurs due to the

injection of electric current into the earth through a pair of current electrodes and the potential difference is measured through a pair of potential electrodes (Sufiyanussuari et al., 2021).

Regional Geology

The geology of Maros Regency is unique because in combination with alluvium deposits (Qac), there are also many limestones, making it famous for its karsts. The forming limestones are members of the Tonasa Formation that experienced tectonics, and intrusion by igneous rocks. In the geological view, limestone types and tectonic influences are two factors that play a role in karstification or karst formation (Arsyad et al., 2020). In addition, there are also other factors such as; enough rainfall, temperature, and forest cover (Diah et al., 2021).

Seawater Intrusion

Seawater intrusion or seepage into aquifers on land is basically the process of seawater pressing into fresh groundwater in aquifers in coastal areas (Motalebbian et al., 2019; Prusty, & Farooq, 2020; Costall et al., 2020; Moore, & Joye, 2021). If the hydrostatic balance between fresh underground water and saline underground water in coastal areas is disturbed as shown in Figure 1, movement and seawater intrusion will occur. The continuous exploitation of groundwater causes a lot of empty space in the aquifer layer which results in the seawater intrusion into the soil layer resulting in a difference in groundwater level lower than the sea level (Ardaneswari et al., 2016; Alfarrah, & Walraevens, 2018; Guo et al., 2019).

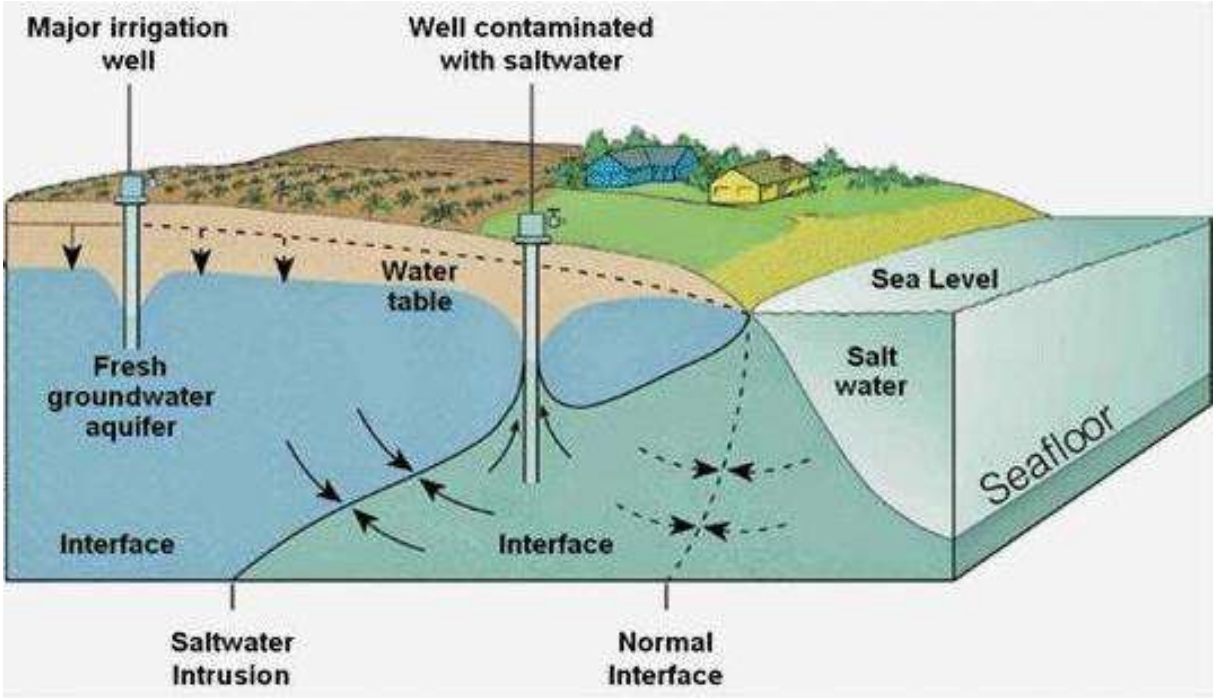

Figure 1. The relationship between freshwater and saltwater (Abd-Elaty et al., 2018).

The main causes of saltwater intrusion include (Abd-Elaty et al., 2018; Prusty, & Farooq, 2020):

1) Overabstraction of the aquifers
2) Seasonal changes in natural groundwater flow
3) Tidal effects
4) Barometric pressure
5) Seismic waves
6) Dispersion
7) Climate change – global warming and associated sea level rise.

Resistivity Method

The resistivity method is one of the geoelectric methods used for subsurface investigations by utilizing the nature of electricity flow within the earth's surface and how to detect it on the earth's surface. This method includes measuring the potential difference and electric current that occurs due to the injection of electric current into the earth through a pair of current electrodes (A and B in Figure 2). The potential difference is measured through a pair of potential electrodes (M and N in Figure 2) (Sufiyanussuari et al., 2021). If ΔV is the potential difference, I is the current and K is the geometry factor, then the resistivity can be written as (Riwayat et al., 2018):

$$\rho = K\frac{\Delta V}{I} \quad (1)$$

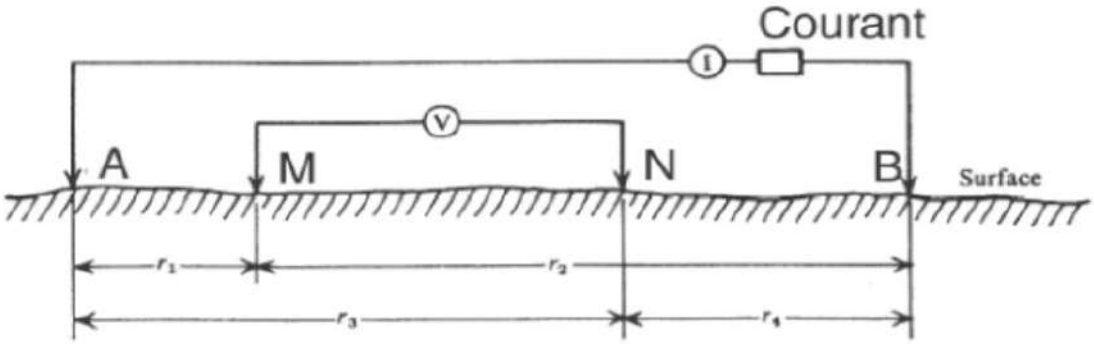

Figure 2. Two current electrodes and two potential electrodes on the surface; Courant is power in French (Baba et al., 2014).

Figure 3. Measurement line map.

Research Methods

This research was conducted in Soreang Village, Maros Regency, South Sulawesi with a total of 2 lines with a length of 470 meters each. The research was conducted using the Wenner-Schlumberger array resistivity method. This array is believed to be better than other configurations such as Dipole-Dipole (Hermawan, & Putra, 2016). The data obtained are current value, potential value, and resistivity value. After data acquisition, data processing and inversion are carried out to produce a subsurface resistivity distribution value at the research location in the form of a 2D cross section.

Figure 3 displays the two measurement lines. Line 1 (yellow color) in the direction of Southwest - Northeast along the Makassar - Parepare railway construction site and Line 2 (red color) in the direction of Southeast - Northwest. In addition, there are also sondir data as support in this study.

Results and Discussion

The data from the measurement of the resistivity method in the field is processed to obtain the resistivity cross section of the inversion results for all measurement lines, as described below:

Line 1

Sondir with a total of 10 data points and half of the measured line length is a former excavation that has been filled into overburden. The combination of 2D resistivity cross section of inversion results of line 1 with sondir data is depicted in Figure 4.

Based on the resistivity value of the inversion results and geological information in the study area, it can be indicated that there are 3 layers. Layer 1 imaged in gray is interpreted as overburden material which has a resistivity value of 1 - 1000 Ωm. Layer 2 with a resistivity value range of 1 - 6 Ωm (blue color) is interpreted as alluvium deposits consisting of clay, silt, and sand. Layer 3 with a resistivity value ≥ 7 Ωm (green color) is interpreted as limestone. The interpretation results are tied to the sondir data and provide the same layer information. The sondir data provides information that from the top soil up to 22 meters down is an alluvium deposit consisting of silt, clay, and sand, while at a depth of 22 meters it states as a limestone layer which is estimated to be continuous and massive downwards, as shown in Figure 5.

Based on the resistivity values in Figure 5, it can be determined which zones are indicated to be in contact with seawater or to be areas of seawater intrusion. Figure 6 provides an overview of the parts identified as seawater intrusion zones marked with dotted lines and angles.

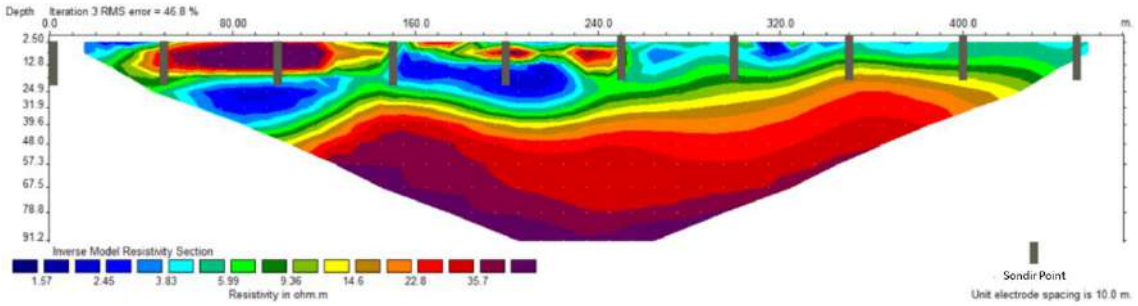

Figure 4. The position of the sondir with respect to line 1.

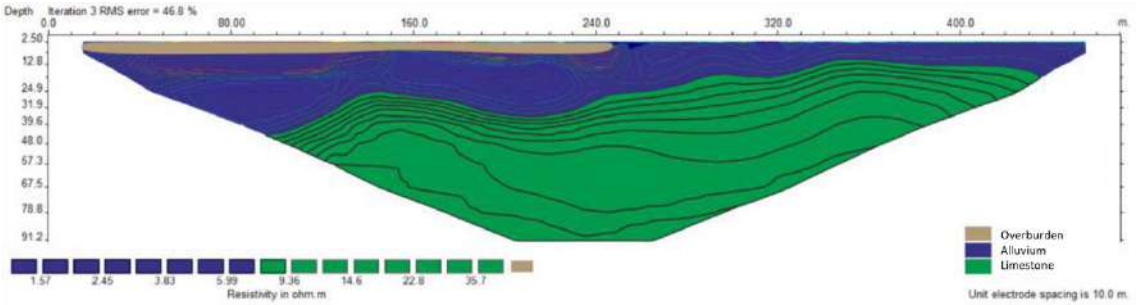

Figure 5. Interpretation of 2D cross-section of the inversion results of line 1 tied to the sondir data.

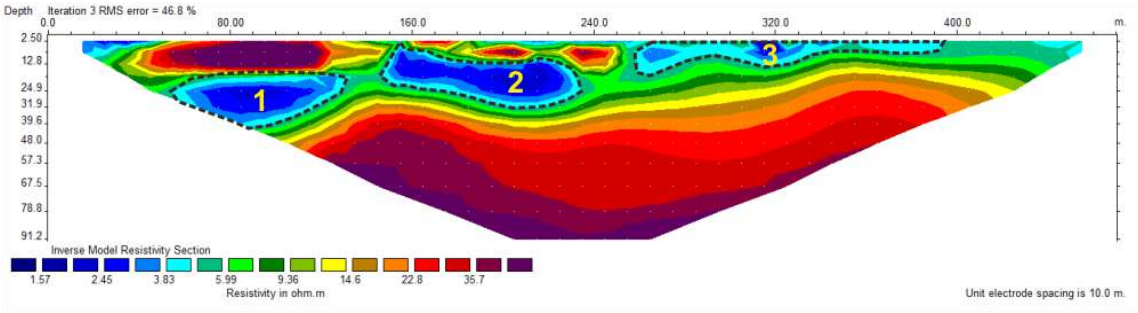

Figure 6. Seawater intrusion zone of line 1.

The seawater intrusion zone is indicated in layer 2 which is an alluvium deposit. This layer has three indicated sections, section 1 is located at electrode 6 (measuring point 50 meters) to electrode 14 (measuring point 130 meters) which is estimated that seawater intrusion starts from a depth of 40 - 20 meters below the surface section 2 is located at electrode 16 (measuring point 150 meters) to electrode 24 (measuring point 230 meters) which is estimated that intrusion starts from a depth of 32 - 2.5 meters below the surface. Section 3 is located at electrode 25 (measuring point 240 meters) to electrode 40 (measuring point 400 meters) and it is estimated that the intrusion starts from a depth of 16 meters and continues to the surface.

Line 2

Based on the variation of resistivity values and regional geological information in the study area, in line 2, 3 layers were identified as obtained similar with line 1. Layer 1, which is considered as overburden material, is only a few meters in the middle of the line. While layer 2, which is interpreted as an alluvium layer, dominates the surface with a depth that varies between 10 - 20 meters from the surface (Figure 7).

Figure 8 shows the seawater intrusion zone on line 2 is also in layer 2 which is marked with dotted lines and numbers. Based on the resistivity analysis in Line 2, there are two sections indicated as seawater intrusion zones in the alluvium layer. Section 1 is located at electrode 1 to electrode 20 (about 200 meters along the line) with a depth of up to 13 meters. Section 2 is at electrode 22 to electrode 48 or 260 meters long and has depths varying up to 26 meters subsurface, including under layer 1.

The relation between the interpretation of Line 2 and Line 1 can be seen after the two cross-sections are combined, as shown in Figure 9.

Figure 9 is a combination of Figure 5 and Figure 7, showing the intersection of the two lines above. Figure 9 (a) and (b) are shown, just to show the connection at the intersection of the two lines seen from different directions. Although the intersection is not exactly right, it still has the same pattern, so it is considered that they are related and mutually reinforcing.

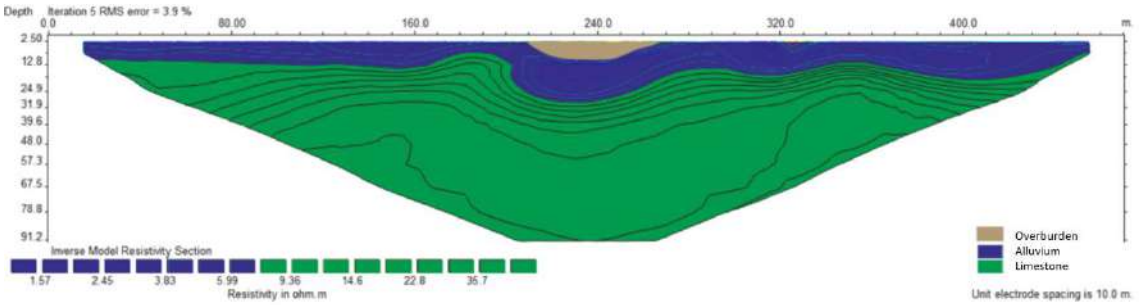

Figure 7. Layer distribution of inversion results on line 2.

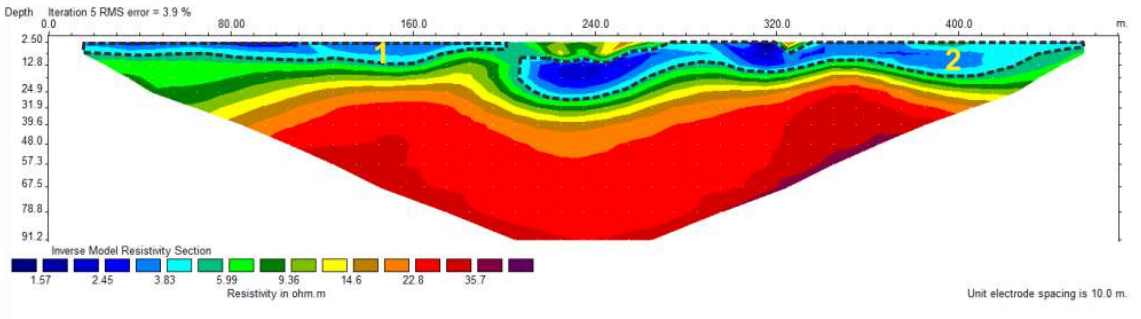

Figure 8. Seawater intrusion zone of line 2.

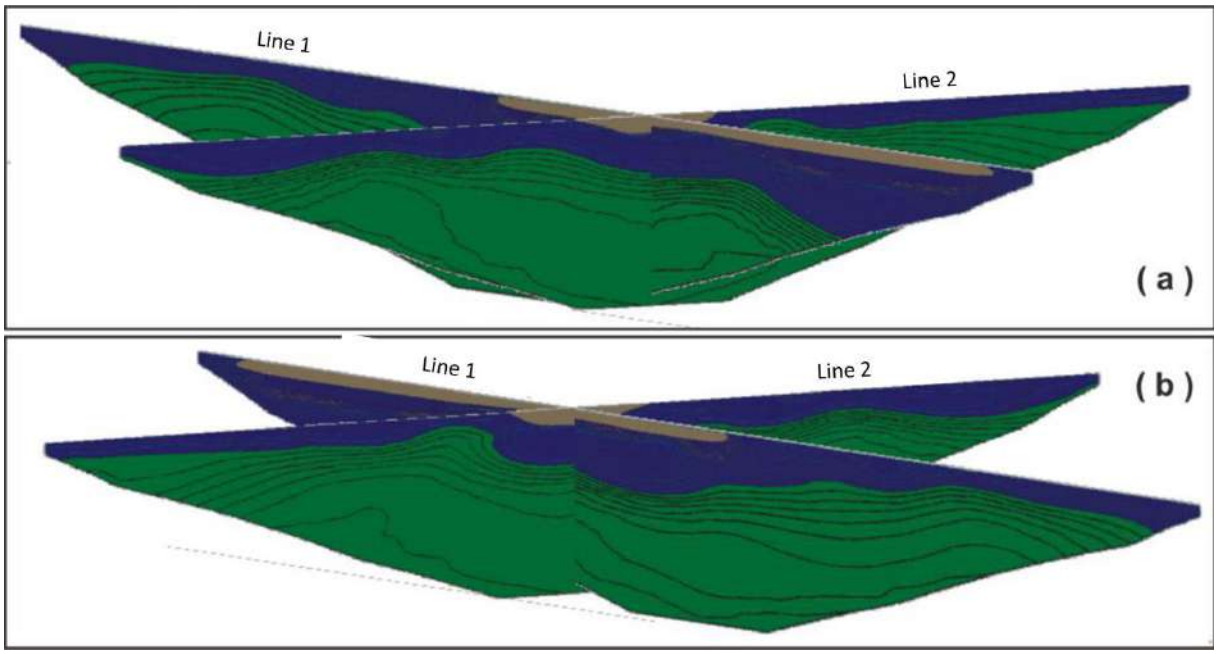

Figure 9. (a) from the west, and (b) from the east.

Conclusion

The subsurface structure in the study area consists of two layers, the first is alluvium deposits (silt, clay, and sand) with a resistivity range of 1 - 6 Ωm and the second is limestone with a resistivity value between ≥ 7 Ωm.

Seawater intrusion is in the alluvium layer with a resistivity value of 1 - ≤ 5 Ωm with varying depths. Line 1 has 3 zones with varying depths ranging from 20 - 40 meters below the surface, 2.5 - 32 meters of subsurface and 16 meters from the surface. The intrusion zone on line 2 has a depth that varies from the surface to 26 meters of subsurface.

Acknowledgments

We gratefully acknowledge the funding from LP2M Hasanuddin University through PDPA research grant. We thank to Geophysics Department, Hasanuddin University (UNHAS) for supporting this research.

Author Contribution

Syamsuddin, MF, AHW, NS, R, MFIM, Selfiana, BH conceived the study; Syamsuddin and MFIM contributed to the writing of the manuscript. All authors contributed to the preparation of the manuscript. All authors have read and approved the final manuscript.

Conflict of Interest

The authors declare no conflict of interest.

References

Abd-Elaty, I., Abd-Elhamid, H.F., & Negm, A.M. (2018). Investigation of Saltwater Intrusion in Coastal Aquifers. In: Negm, A. (eds) *Groundwater in the Nile Delta*, 329–353. Springer, Cham. https://doi.org/10.1007/698_2017_190

Alfarrah, N., & Walraevens, K. (2018). Groundwater Overexploitation and Seawater Intrusion in Coastal Areas of Arid and Semi-Arid Regions. *Water*, 10(2), 143. https://doi.org/10.3390/w10020143

Ardaneswari, T.A., Yulianto, T., & Putranto. T.T. (2016). Analisis Intrusi Air Laut Meggunakan Data Resistivitas dan Geokimia Airtanah di Dataran Aluvial Kota Semarang. *Youngster Physics Journal*. 5(4), pp.335–350. https://ejournal3.undip.ac.id/index.php/bfd/article/view/14116

Arsyad, M., Ihsan, N., & Tiwow, V. A. (2020). Analysis of mineral sediment characteristics of Bantimurung Bulusaraung National Park in the Karst Maros Region. *Journal of Physics: Conference Series*, 1572(012007), 1–7. https://doi.org/10.1088/1742-6596/1572/1/012007

Baba, K., Bahi, L., Ouadif, L., & Cherradi, C. (2014). Application des méthodes d'analyses statistiques multivariées à la délimitation des anomalies de Sidi Chennane (Multivariate Statistical Analysis tool for the interpretation of geoelectrical data: application to Sterile Bodies in the Sidi Chennane phosphatic deposit (Morocco)). *Journal of Materials and Environmental Science*, 5(4), 1005–1012. https://www.jmaterenvironsci.com/Document/vol5/vol5_N4/124-JMES-631-2014-Baba.pdf

Costall, A. R., Harris, B. D., Teo, B. Schaa, R., Wagner, F. M., & Pigois, J. P. (2020). Groundwater Throughflow and Seawater Intrusion in High Quality Coastal Aquifers. *Scientific Reports*, 10, 9866. https://doi.org/10.1038/s41598-020-66516-6

Diah, H., Adji, T. N., & Haryono, E. (2021). Perbedaan Tingkat Perkembangan Karst Daerah Peralihan antara Basin Wonosari dan Karst Gunungsewu. *Media Komunikasi Geografi*, 22(1), 51–61. https://doi.org/10.23887/mkg.v22i1.30885

Guo, Q., Huang, J., Zhou, Z., & Wang, J. (2019). Experiment and Numerical Simulation of Seawater Intrusion under the Influences of Tidal Fluctuation and Groundwater Exploitation in Coastal Multilayered Aquifers. *Flow, Transport, and Reactions in Coastal Aquifers*, 2019, 2316271. https://doi.org/10.1155/2019/2316271

Haroon, A., Micallef, A., Jegen, M., Schwalenberg, K., Karstens, J., Berndt, C., Garcia, X., Kühn, M.,

Rizzo, E., Fusi, N. C., Ahaneku, C. V., Petronio, L., Faghih, Z., Weymer, B. A., De Biase, M., & Chidichimo, F. (2021). Electrical resistivity anomalies offshore a carbonate coastline: Evidence for freshened groundwater? *Geophysical Research Letters*, 48, e2020GL091909. https://doi.org/10.1029/2020GL091909

Hermawan, O. R. & Putra, D. P. E. (2016). The Effectiveness of Wenner-Schlumberger and Dipole-dipole Array of 2D Geoelectrical Survey to Detect the Occurring of Groundwater in the Gunung Kidul Karst Aquifer System, Yogyakarta, Indonesia. *Journal of Applied Geology*, 1(2), 71–81. https://core.ac.uk/download/291851623.pdf

Huq, H., & Easher, T. H. (2021). Coastal Water: Wisdom, Destruction, Conflicts and Contestation – A Case of Southwest Coastal Region of Bangladesh. *IntechOpen*. https://doi.org/10.5772/intechopen.95002

Jeuken, A., Termansen, M., Antonellini, M., Olsthoorn T., & van Beek, E. (2017). Climate Proof Fresh Water Supply in Coastal Areas and Deltas in Europe. *Water Resource Management*, 31, 583–586. https://doi.org/10.1007/s11269-016-1560-y

Masciopinto, C., Liso, I., Caputo, M., & De Carlo, L. (2017). An Integrated Approach Based on Numerical Modelling and Geophysical Survey to Map Groundwater Salinity in Fractured Coastal Aquifers. *Water*, 9(11), 875. https://doi.org/10.3390/w9110875

Motallebian, M., Ahmadi, H., Raoof, A., & Cartwright, N. (2019). An alternative approach to control saltwater intrusion in coastal aquifers using a freshwater surface recharge canal. *Journal of Contaminant Hydrology*, 222, 56–64. https://doi.org/10.1016/j.jconhyd.2019.02.007

Moore, W. S., & Joye, S. B. (2021). Saltwater Intrusion and Submarine Groundwater Discharge: Acceleration of Biogeochemical Reactions in Changing Coastal Aquifers. *Frontiers Earth Science*, 9, 600710. https://doi.org/10.3389/feart.2021.600710

Prusty, P., & Farooq, S. H. (2020). Seawater intrusion in the coastal aquifers of India - A review. HydroResearch, 3, 61–74. https://doi.org/10.1016/j.hydres.2020.06.001

Rahman, M. T. U., Rasheduzzaman M., Habib, M. A., Ahmed, A., Tareq, S. M., & Muniruzzaman, S. M. (2017). Assessment of fresh water security in coastal Bangladesh: An insight from salinity, community perception and adaptation. *Ocean & Coastal Management*, 137, 68–81. https://doi.org/10.1016/j.ocecoaman.2016.12.005

Rahmaniah., Wahyuni, A., Massinai, M. F. I., Mun'im, A., & Massinai, M. A. (2021). Resistivity Method for Characterising Subsurface Layers of Coastal Areas in South Sulawesi, Indonesia. *Journal of Geoscience, Engineering, Environment, and Technology*, 6(4), 217–225. https://doi.org/10.25299/jgeet.2021.6.4.6242

Riwayat, A. I., Nazri, M. A. A., & Abidin, M. H. Z. (2018). Application of Electrical Resistivity Method (ERM) in Groundwater Exploration. Journal of Physics: Conference Series, 995(012094), 1–9. https://doi.org/10.1088/1742-6596/995/1/012094

Sufiyanussuari, S. A., Tajudin, S. A., Azmi, M. I. S., Zahari, M. N. H., & Muztaza, N, M. (2021). Groundwater Pathway Mapping Using Electrical Resistivity Tomography (ERT) Method. *Journal of Sustainable Underground*

Exploration, 1(1), 32–37. https://publisher.uthm.edu.my/ojs/index.php/j-sue/article/view/10164

ISSN: 2579-5821 (Print)
ISSN: 2579-5546 (Online)
URL address: http://journal.unhas.ac.id/index.php/geocelebes
DOI: 10.20956/ geocelebes.v7i2.22348

Jurnal Geocelebes Vol. 7 No. 2, October 2023, 108 – 116

Analysis of Seismotectonic Parameters and Earthquake Return Periods in The Nias Area (1980-2021)

Riski Efrina[1], Lailatul Husna Lubis[1*], Ratni Sirait[1], Novita Sari[2]

[1]Physics Study Program, Faculty of Science and Technology, State Islamic University North Sumatra, 20371, Indonesia
[2]BMKG Class 1 Geophysics Station Deli Serdang, North Sumatra, 20353, Indonesia

*Corresponding author. Email: lailatulhusnalubis@uinsu.ac.id

Manuscripts received: 27 August 2022; Received in revised form: 13 December 2022; Accepted: 27 January 2023

Abstract

The Nias Islands region is an area prone to earthquakes with a very high level of earthquake activity. One reason is the source of the subduction zone which is in the northwest of the Nias Islands. The aim of this work is to determine the b-value, seismic index, and earthquake return period using probabilistic techniques. For the years 1980 to 2021, the Meteorology, Climatology and Geophysics Agency (BMKG) published data with a magnitude of 3-6.7 and a depth (H) of 10-300 Km. The research results obtained by calculating the highest b-value is 0.791 in South Nias district and the highest a-value is in the South Nias district of 3.97. Calculation of the highest seismicity index with a magnitude of 6.7 in South Nias district with a-value of 7.223191 with an earthquake return period of 14 years.

Keywords: a-value; b-value; likelihood; return period; seismicity index.

Citation: Efrina, R., Lubis, L. H., Sirait, R., and Sari, N. (2023). Analysis of Seismotectonic Parameters and Earthquake Return Periods in The Nias Area (1980-2021). *Jurnal Geocelebes,* 7(2), 108–116, doi: 10.20956/geocelebes.v7i2.22348

Introduction

Indonesia is a country with a high level of earthquake risk. This is due to the geographical location of Indonesia which is a meeting place Among three the earth's plates which are Eurasian, Australian, and Pacific (Madlazim, 2013; Aslamia & Supardi, 2022).

Geological phenomenon what raises the potential for large earthquakes is the movement of these plates. Earthquakes may occur at the boundary between plates and faults which can occur at any time. Friction between these plates creates pressure and fractures which result in shifting of rocks (Feng et al., 2022).

Geologically, the seismicity of the Sumatra region has a complex rock structure and has experienced collisions from tectonic processes several times. Because its position lies at the confluence of the Eurasian plate to the east and the Australian plate to the west. As a result of the activity of these plates, at any time it can cause earthquakes and tsunamis. In addition, areas that are classified as vulnerable are water areas. Under these conditions, the Sumatra region is very active in seismic activity (Madlazim, 2013; Anwar, 2019).

One of the many small islands to the west of the island of Sumatra is the Nias Archipelago. The cause of the seismicity was due to seismic activity in the Sumatra region based on BMKG monitoring data obtained on the occurrence of a 7.6 Nias seismicity in 1961 (BMKG, 2019). This is most likely caused by the collision of the two plates (BNPB, 2018).

Collision between the two plates produces tectonics that form a subduction zone in the northwest of the island of Sumatra which consists of the Mentawai fault and the Semangko fault which extends from Aceh to Lampung. these tectonic plates will move, collide and rub against each other, so that energy will one day be released to achieve balance, in the form of the 1961 Nias earthquake which had a magnitude of 7.6 (Damayanti et al., 2020; Lubis et al., 2022).

Precautions from earthquakes need to be carried out with a study of seismotectonics in the Nias Islands region. Seismotectonic parameters can be in the form of rock fragility (b-value), seismic activity (a-value), the average number of events earthquake (seismicity index) and earthquake return period based on seismotectonic parameter values by using the relationship between frequency and magnitude of earthquakes by calculating using the likelihood method.

In order to limit infrastructure damage due to large earthquakes, which can even trigger a tsunami, then need for knowing the value of seismotectonic parameters that can be used by local governments as a guideline for building earthquake-resistant infrastructure is very important.

This technique has the benefit of enabling statistical calculations of earthquake parameter values, rock fragility values, and predictions of earthquake return periods. The likelihood method is a statistical approach that is suitable for solving problems involving seismotectonics (Suwandi et al., 2017; Ernandi & Madlazim, 2020).

Based on Geological data for the Nias Islands region (Djamal et al., 1994), most of Nias Island consists of sedimentary rocks of Tertiary age called the Bancuh Complex, which consists of a bed mass of scaly clay and sedimentary rocks such as claystone, marl, sandstone, limestone and alternating sandstone, claystone, siltstone, conglomerate, and tuff. Quarter sediments, on the other hand, consist of alluvial deposits from rivers, swamps, and beaches as well as reef limestone.

The fault, which is in the same direction as the Nias Islands from northwest to southeast, dominates the geological structure of the Nias Islands. Previous tectonic activity has resulted in the formation of this geological structure pattern. There are many active faults in these islands. In conclusion, shallow earthquakes are common. According to Weiss et al. (2018), these faults are located in the accretion wedge zone, which originates at the tertiary start, close to the impact zone. Continuous collisions will result in greater seismic activity.

The geological features that are likely to be the source of earthquakes in the Nias Islands can be seen in Figure 1. Lithologically, the constituent rocks are dominated by Alluvium (Qa), the Gunungsitoli Formation in blue (Qtgs), the Gomo Formation in brown (Tmpg), the Lolomatua Formation with yellow (Tml), Bancuh Complex Formation in red (Tomm).

The rock type most vulnerable to earthquakes is the Bancuh Complex rock type with red color (Tomm). Where this rock type is composed by the morphology of the coastal plains, rivers, swamp hills, and mountains. The shock effect increases with weathering of Pre and Tertiary rocks and quarterly deposits, which are usually crushed, fragmented and uncompacted. (Djamal et al., 1994).

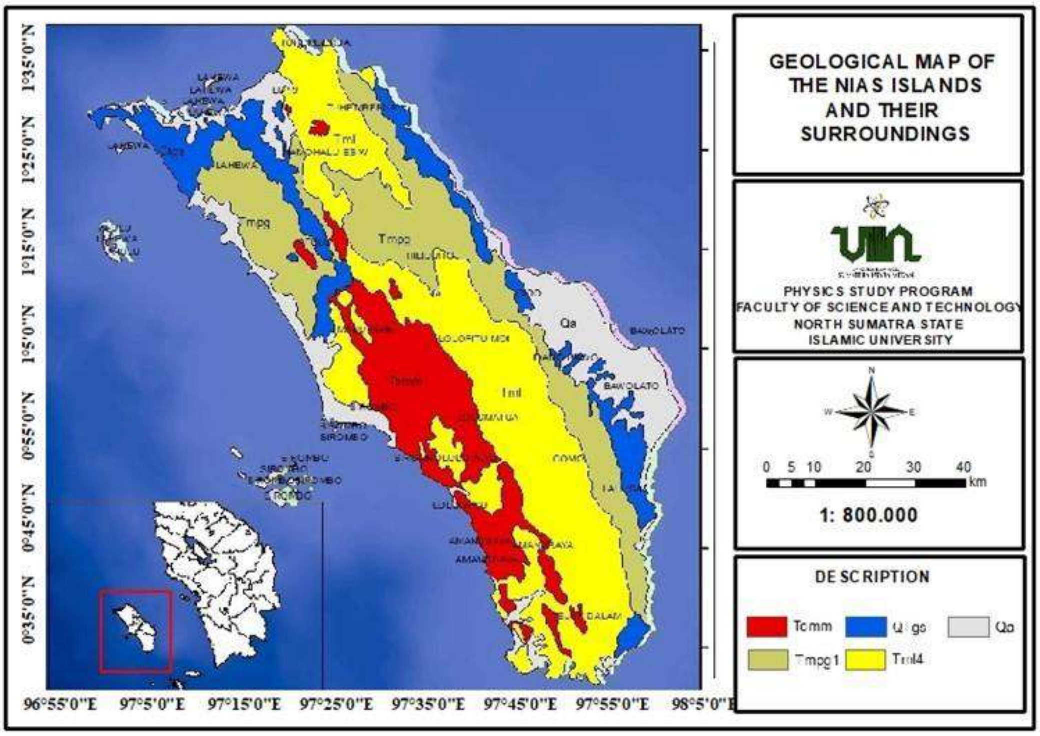

Figure 1. Geological Map of Nias Islands.

Materials and Methods

The research location is located at the location coordinates 0°10'0" - 1°30'0" N and 97°0'3" - 97°0'56" E with an area of 1,004.06 km^2. Nias islands region based on each region as in Figure 2.

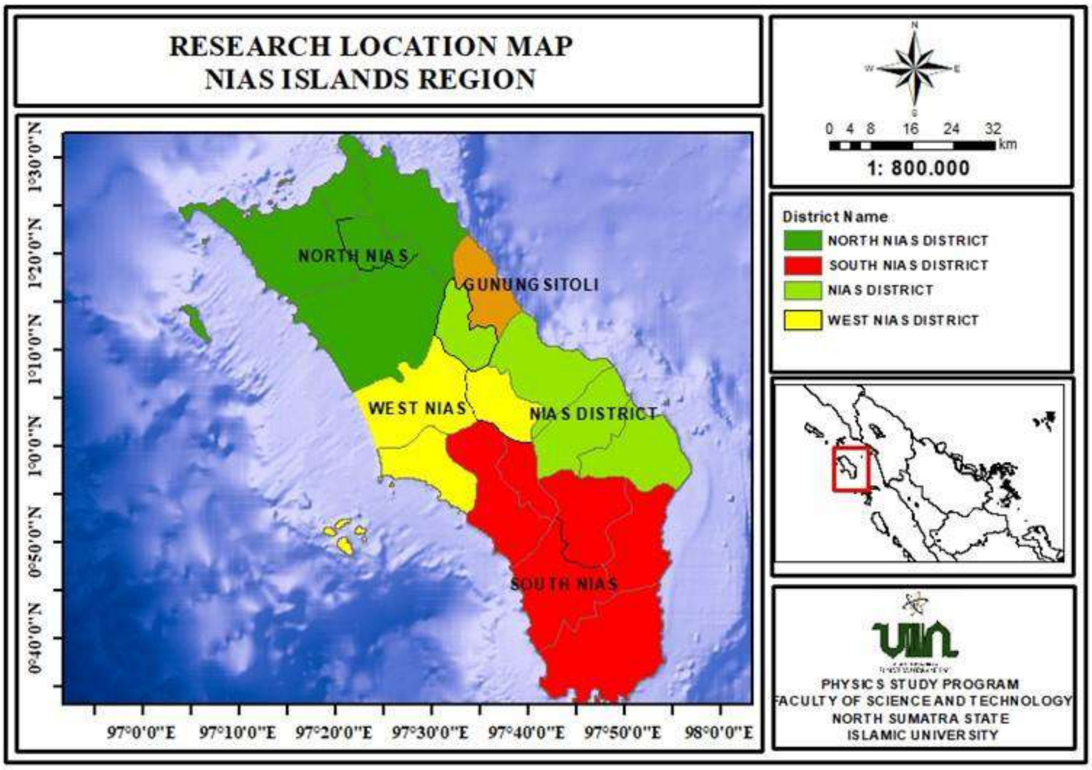

Figure 2. Map of research locations.

The equipment and supplies used were a laptop for data processing, Microsoft Excel software for sorting data, and ArcGIS 10.8 software for making geological maps of the Nias Islands and research location maps.

The data source used is the Deli Serdang Class 1 Geophysics Station which provides earthquake parameter data in the form of area coordinates (latitude and longitude), year, month, date, magnitude, depth, and time of origin with magnitude 3–10 and depth (H) 1– 300 km, which is a shallow to deep depth with a high damage potential. The 41-year period covered by the study's seismic data spanned from January 1, 1980 to December 31, 2021.

Data processing is carried out using Microsoft Excel software for sorting data such as coordinates (latitude and longitude), year, month, date, magnitude and depth in each area. After that, the data processing is done manually. The steps in processing earthquake data include:

1. Examining the literature that supports the study of b-value and a-value seismotectonic analysis on the Nias Islands is known as a literature review .
2. By dividing the five regencies in the study area into equal parts, the b-value, a-value, seismic index, and earthquake return period were determined.
3. Mapping was carried out using the seismicity index level mapping using Arcgis 10.8 software .
4. Equations (1) and (2) are used to calculate b-values and a-values using the maximum likelihood method (Kijko et al., 2022; Zaccagnino et al., 2022):

$$b = \frac{log\ e}{\bar{M} - M_0} \quad (1)$$

$$a = \log N + (b \ln 10) + M_0 . b \quad (2)$$

5. Furthermore, according to Welkner (1965) the calculation of the seismicity index to describe the number of earthquakes per year with a magnitude greater than the smallest magnitude. According to Welkner (1965) with a seismicity index of "N (M ≥ 3)" using equation (3).

$$N_1\ (\bar{M} \geq 3.0) = 10^{a_1' - 3.b} \quad (3)$$

Divide the a-value by the study period (T) to determine the number of earthquakes each year.

$$a_1 = a - \log T$$

$$a' = a_1 - (\log b) . (\ln 10)$$

$$a_1' = a' - \log T \quad (4)$$

6. The determination of the return period of an earthquake uses equations (5) and (6) to see the possibility of damaging earthquakes occurring in the future. Where the maximum magnitude of the earthquake return period has the highest annual average cumulative frequency (T) (Fidia et al., 2018; Septiani & Pujiastuti, 2021):

$$N_1^{(M>6.7)} = N_1^{(M>3)} . 10^{-2.b} \quad (5)$$

$$\theta = \frac{1}{N_1\ (\bar{M} \geq M_0)} \quad (6)$$

Research Result

Results of manual calculation of b-value and a-value

If the b-value is reached, the calculation results used to determine the degree of fragility of the rock (b-value) shows a relatively high indicator of rock fragility and relatively low association with fractures. Meanwhile, relatively strong assertiveness correlates with a relatively low b-value.

The results of calculating the level of earthquake activity (a-value) show that if the a-value is reached, the higher the a-value, the more frequent earthquakes occur in that location, and the lower the a-value, the more frequent earthquakes occur in that area.

The seismic parameters b-value and a-value are combined for the analysis because they can help predict the likelihood of major

earthquakes in a given area. Where the a-value is a seismicity constant and the b-value is a fracture distribution constant whose value is directly proportional to the a-value.

Based on the results of manual calculations (Table 1), the highest b-value results were found in South Nias district of 0.791. While the lowest b-value of 0.446 is found in North Nias district. The results of the highest a-value were found in the South Nias district of 3.97. While the lowest a-value is in North Nias district with a-value of 2.67.

Table 1. A-value and b-value based on the five districts in the Nias Islands using manual calculations.

No	Research Area	b-values	a-values
1	Nias Regency	0.555	2.83
2	South Nias Regency	0.791	3.97
3	North Nias Regency	0.446	2.67
4	West Nias Regency	0.517	2.79
5	Mount Sitoli	0.740	3.09

Seismicity index value results

The seismicity index is needed to determine the typical number of earthquakes per year with a certain magnitude. Where the magnitude is greater than the smallest magnitude ($M \geq 3$) If the earthquake seismicity index value is N ($(M \geq 3)$ in a period of 41 years in each region, with a high seismicity index value, then the area is classified as prone to earthquakes.

The results of calculating the seismicity index for five areas in the Nias archipelago and its surroundings with $M \geq 3$ range from 0.09677 to 7.22319.

Whereas for the South Nias region it is 7.22319 which has a greater seismic index than other regions. In other words, the South Nias region has a lot of earthquake activity and is vulnerable to earthquake-related disasters. Statistics on the occurrence of earthquakes in South Nias Regency, which is higher than other locations, is proof of this claim. Meanwhile, Nias Regency has a low seismicity index compared to other values, which is 0.09677. Based on previous research by Nfingrum et al. (2022) the results of a high seismic vulnerability index value will be vulnerable to earthquake disasters and alluvium type factors consisting of gravel, sand can also affect disasters in the area.

As a result, the selected earthquake data is very helpful for various tasks such as designing earthquake resistant structures or preparing areas for potential earthquakes. Table 2 displays the results of manually calculating the seismic index values as follows.

Table 2. Seismicity index calculation.

Area	A value	a_1	a'	a'_1	$N_1 = (M \geq 3)$
Nias Regency	2.83	1.21953	1.80823	0.19544	0.09677
South Nias Regency	3.97	2.36147	2.59498	0.98220	7.22319
North Nias Regency	2.67	1.06079	1.866888	0.25410	0.45536
West Nias Regency	2.79	1.18551	1.84369	0.23090	0.14840
Mount Sitoli	3.09	1.48344	1.784171	0.17138	0.73701

Earthquake return period

The probability of a destructive earthquake occurring is based on five areas in the Nias Islands and its surroundings. Based on Table 3. The highest destructive earthquake index value with the fastest repetition rate with a magnitude (M) of 6.7, which is in the South Nias Regency area of 0.0571 for 14 years. While the index value of the lowest destructive earthquake with the longest

earthquake repetition rate was 5.8, which is in the Nias district of 0.0005 for 1861 years.

Table 3. Destructive earthquake index value and return period.

Area	Destructive earthquake index value	Return Period Value	Magnitude (M)
Nias Regency	0.0005	1861 year	5.8
South Nias Regency	0.0571	14 years	6.7
North Nias Regency	0.0020	491 years	6
West Nias Regency	0.0007	1301 years	5.6
Mount Sitoli	0.0054	183 years	5.3

Discussion

B-value which describes the level of fragility of rocks is one of the benchmarks of tectonic conditions in a region. Areas that have large rock characteristics will easily experience cracks and are relatively unable to withstand the weak level of rock fragility. Meanwhile, the relatively low b-value parameter correlates with relatively high fractures (Naimi-Ghassabian et al., 2016). Where is the area with a high level of rock fragility, which is in South Nias Regency with a b-value of 0.791.

The Bancuh rock complex (Tomm) which is composed of the morphology of the coastal plains, valleys and hills dominates the geology of this area. Pre-tertiary (metamorphic and metasedimentary rocks) and quaternary deposits form these rock conditions (alluvial, coastal, riverine, and marshy). The pre-tertiary rock has been weathered, and the quarterly deposits in the south Nias region have been decomposed, loose and not yet compacted, which amplifies the effects of the shaking.

In addition to the level of rock fragility, the level of seismic activity also affects this area where the value of the level of seismic activity (a-value) in this area is 3.97 which means this area is very active in seismicity. The Australian plate immigrates from the northwest and subducts into the European continental plate, and the South Nias Regency area is close to this convergence point (megathrust zone). Where this area stretches from the northwest-southeast region of Nias Island.

Based on Damayanti et al. (2020) and Lubis et al. (2022) the main fault line that cuts through Nias Island in a northwest-southeast direction, known as the Nias fault line, is the main contributor to earthquakes in South Nias Regency apart from the megathrust zone. The Nias-Ordi-Bahorok fault line, which originates from the western part of Pini Island and crosses Sumatra, is another important fault line in the southern part of Nias Island. The potential for earthquakes in this region is quite large due to the causes of earthquakes which can also result in disasters such as tsunamis and landslides.

If it is associated with the seismicity index which describes the number of annual earthquakes the highest occurs in the South Nias Region, which is 7.223191. When planning earthquake-resistant buildings or preparing an area for possible earthquakes, for example, this value is very helpful.

While the return period shows the possibility of damaging earthquakes in the future. The return period of this seismicity is seen by determining the magnitude of the greatest seismicity, which is the magnitude (M) 6.7. Where the shortest area of repetition is South Nias Regency for 14 years.

In the previous study, Daiana et al. (2021) conducted research using seismicity analysis of b-value studies using earthquake data from 1914 to 2020 (Case study: Bengkulu Province). The results show that the environment closest to the coast has the largest a- and b-values, which is in the range of 3.05 – 3.2. The mainland

area of Bengkulu Province has a high level of seismicity, according to the variation in the b-value. This is possible because the rocks that make up Pre-Tertiary and Tertiary rocks, as well as quarterly deposits, are usually decomposed, loose, and soft in coastal areas, which can increase the impact of earthquake shocks.

Conclusion

From the results of the analysis of seismotectonic parameters and earthquake return periods in the Nias region in 1980-2021 it can be concluded that: first, the calculated b-value for Nias district is 0.555, South Nias district is 0.791, North Nias district is 0.446, West Nias district is 0.517, and Gunung Sitoli is 0.740. While the results of the calculation of the a-value for Nias district is 2.83, South Nias district is 3.97, North Nias district is 2.67, West Nias district is 2.79, and Gunungsitoli is 3.09. The second, the Seismicity Index value in each region with a magnitude greater than the smallest magnitude ($M \geq 3$) Nias district is 0.096770, South Nias district is 7.223191, North Nias is 0.455368, West Nias is 0.148408, and Gunungsitoli is 0.73701. The last, the return period value for each region is Nias district of 0.0005 with destructive earthquakes (M) 5.8 with a predicted return period of 1861 years, South Nias District of 0.0571 with destructive earthquakes (M) 6.7 for 14 years, North Nias of 0, 0020 with destructive earthquakes (M) 6 for 491 years, West Nias for 0.0007 for destructive earthquakes (M) 5.6 for 1301 years, and Gunungsitoli for 0.0054 with destructive earthquakes (M) 5.3 for 183 years.

Acknowledgements

The authors thanks Agus Riyanto, Head of Class 1 Geophysics Station Deli Serdang who has helped and provided data for data processing.

Author Contribution

In the preparation of this research journal, each author contributed to several parts, which are for data processing and library resources by Riski Efrina, journal compilation by Lailatul Husna Lubis while observers and supervisors in compiling this journal were Ratni Sirait and Novita Sari.

Conflict of Interest

In this study there were no funds or finances issued, either between the authors or the parties involved in this research. so that the author can account for it with the rules in the Journal of Geocelebes.

References

Anwar, S. (2019). Mengukur Peluang Kejadian Gempa Bumi dengan Lompatan Magnitudo di Wilayah Pulau Sumatera. *Jurnal Lingkungan dan Bencana Geologi*, 10(3), 159–170. http://dx.doi.org/10.34126/jlbg.v10i3.263

Aslamia, H., & Supardi, Z. A. I. (2022). Analisis Parameter a-Value Dan b-Value sebagai Mitigasi Bencana Gempa Bumi di Nusa Tenggara Timur. *Jambura Physics Journal*, 4(1), 14–27. https://doi.org/10.34312/jpj.v4i1.13815

BMKG. (2019). *Katalog Gempabumi Signifikat dan Merusak 1821-2018*. https://cdn.bmkg.go.id/web/katalog-gempabumi-signifikan-dan-merusak-1821-2018.pdf.

BNPB. (2018). *Rencana Kontinjensi Menghadapi Bencana Tsunami Provinsi Sumatera Barat*. https://bnpb.go.id/uploads/24/rencana-kontigensi-tsunami-sumatera-barat.pdf.

Daiana, S. T., Nurhidayah, & Handayani, L. (2021). Studi B-Value sebagai Analisis Seismisitas Berdasarkan Data Gempabumi Periode 1914–2020 (Studi Kasus: Provinsi Bengkulu). *Jurnal Sain dan Teknologi Mitigasi*

Bencana, 16(1), 30–41. https://doi.org/10.29122/jstmb.v16i1.4860.

Damayanti, C., Yamko, A. K., Souisa, C. J., Barends, W., & Naroly, I. L. P. T. (2020). Pemodelan Segmentasi Mentawai-Pagai: Studi Kasus Gempa Megathrust di Indonesia. *Jurnal Geosains Dan Remote Sensing*, 1(2), 105–110. https://doi.org/10.23960/jgrs.2020.v1i2.56

Djamal, B., Gunawan, W., Simandjuntak, T. O., & Ratman, N. (1994). *Peta Geologi Lembar Nias, Sumatera*. Puslitbang Geologi. https://geologi.esdm.go.id/geomap/pages/preview/peta-geologi-lembar-nias-sumatera.

Ernandi, F. N., & Madlazim. (2020). Analisis variasi a-value dan b-value dengan menggunakan software zmap v. 6 sebagai indikator potensi gempa bumi di wilayah Nusa Tenggara Barat. *Jurnal Inovasi Fisika Indonesia (IFI*), 9(3), 24–30. https://doi.org/10.26740/ifi.v9n3.p24-30

Feng, C., Gao, G., Zhang, S., Sun, D., Zhu, S., Tan, C., & Ma, X. (2022). Fault slip potential induced by fluid injection in the Matouying enhanced geothermal system (EGS) field, Tangshan seismic region, North China. *Natural Hazards and Earth System Sciences*, 22, 2257–2287. https://doi.org/10.5194/nhess-22-22257-2022

Fidia, R., Pujiastuti, D., & Sabarani, A. (2018). Korelasi Tingkat Seismisitas dan Periode Ulang Gempa Bumi di Kepulauan Mentawai dengan Menggunakan Metode Guttenberg-Richter. *Jurnal Fisika Unand*, 7(1), 84–89. https://doi.org/10.25077/jfu.7.1.84-89.2018

Kijko, A., Vermeulen, P. J., & Smit, A. (2022). Estimation Techniques for Seismic Recurrence Parameters for Incomplete Catalogues. *Surveys in Geophysics*, 43, 597–617. https://doi.org/10.1007/s10712-021-09672-2

Lubis, L. H., Ayundita, A. A., Sari, N., & Wardono, W. (2022). Aktivitas Seismisitas Di Wilayah Sumatera Bagian Utara Menggunakan Arc-Gis Periode 2020-2021. *Jurnal Kumparan Fisika*, 5(2), 91–98. https://doi.org/10.33369/jkf.5.2.91-98

Madlazim, M. (2013). Kajian Awal tentang B Value Gempa Bumi di Sumatra. *Jurnal Penelitian Fisika dan Aplikasinya (JPFA)*, 3(1), 41–46. https://doi.org/10.26740/jpfa.v3n1.p41-46.

Naimi-Ghassabian, N., Khatib, M., Nazari, H., & Heyhat, M-R. (2016). Fractal dimension and earthquake frequency-magnitude distribution in the North of Central-East Iran Blocks (NCEIB). *Geopersia*, 6(2), 243–264. https://doi.org/10.22059/jgeope.2016.58670.

Ningrum, R. W., Amelia, R. N., Taib, S., Achmad, R., & Aswan, M. (2022). Mapping of Seismic Vulnerability Potential for Earthquake Disaster Migitation in South Morotai. *Jurnal Geocelebes*, 6(1), 37–46. https://doi.org/10.20956/geocelebes.v6i1.19150.

Septiani, I., & Pujiastuti, D. (2021). Analisis Seismisitas Wilayah Kepulauan Maluku Periode 1970-2019 dengan Menggunakan Metode Likelihood. *Jurnal Fisika Unand*, 10(4), 461–466. https://doi.org/10.25077/jfu.10.4.461-466.2021

Suwandi, E. A., Sari, I. L., & Waslaluddin, W. (2017). Analisis Percepatan Tanah Maksimum, Intensitas Maksimum Dan Periode Ulang Gempa Untuk Menentukan Tingkat Kerentanan Seismik Di Jawa Barat (Periode Data Gempa Tahun 1974-2016). *Wahana Fisika*, 2(2), 78–96. https://ejournal.upi.edu/index.php/wafi/issue/view/953

Weiss, J. R., Ito, G., Brooks, B. A., Olive, J-A., Moore, G. F., & Foster, J. H. (2018). Formation of the frontal thrust zone of accretionary wedges. *Earth and Planetary Science Letters*, 495, 87–100. https://doi.org/10.1016/j.epsl.2018.05.010

Welkner, P. M. (1965). Statistical Analysis of Earthquake Occurrence in Japan, 1926–1956. *Bulletin of the International Institute of Seismology and Earthquake Engineering*, 2, 1–27.

Zaccagnino, D., Telesca, L., & Doglioni, C. (2022). Correlation between seismic activity and tidal stress perturbations highlights growing instability within the brittle crust. *Scientific Reports*, 12, 7109. https://doi.org/10.1038/s41598-022-11328-z

ISSN: 2579-5821 (Print)
ISSN: 2579-5546 (Online)
URL address: http://journal.unhas.ac.id/index.php/geocelebes
DOI: 10.20956/geocelebes.v7i2.23759

Jurnal Geocelebes Vol. 7 No. 2 October 2023, 117 – 129

Identification of Mount Sirung Geothermal Potential based on Land Surface Temperature and 3D Gravity Model

Ayu Alvita Primastika[1]*, Dhika Faiz Fadrian[2], Fardhan Rafshan Zani[2], Nanda Ridki Permana[3]

[1]GeoXplore Indonesia, Kincir Air Street, Pondok Manggis Block B6, Bojong Baru, Bojonggede, Bogor, West Java, 16920, Indonesia.
[2]Department of Physics, Faculty of Science and Technology, Syarif Hidayatullah State Islamic University Jakarta, 95 Ir. H. Juanda Street, Cempaka Putih, Ciputat, South Tangerang, Banten, 15412, Indonesia.
[3]PT Minelog Services Indonesia, Bumi Serpong Damai (BSD), Industrial Estate and Warehouse Techno Park Block G1 Number 10, Sector 11 Street, Setu, South Tangerang, Banten, 15220, Indonesia.

*Corresponding author. Email: ayu.alvitaa@gmail.com

Manuscript received: 24 November 2022; Received in revised form: 29 January 2023; Accepted: 31 January 2023

Abstract

According to the Ministry of Energy and Mineral Resources 2021 data, first ranks in the list of 10 provinces with the lowest electrification ratio in Indonesia. One of the geothermal prospect areas in East Nusa Tenggara is Mount Sirung. This research was conducted in August 2022 which aims to identify geothermal systems. Gravity data was obtained from the GGMPlus 2013 with a total of 3819 data. Land Surface Temperature (LST) is used as supporting data with a surface temperature approximately 26.1 – 29.5°C because there are manifestations of hot springs at Mount Sirung. Based on the derivative analysis, there are four trajectories in the northwest-southeast direction with reverse faults and normal faults as the geothermal control system of Mount Sirung. The results of 3D gravitational inversion modeling are estimated that there is clay interspersed with breccia with a density of 2.34 – 2.39 g/cm^3 as clay cap at 0 – 600 m, and lava interspersed with sandy tuff as a reservoir with a density of 1.98 – 2.03 g/cm^3 at 700 – 1400 m. Based on these results and discussions, Mount Sirung is proven to have geothermal potential which can be utilized as a source of electrification in East Nusa Tenggara.

Keywords: derivative analysis; geothermal; gravity; Land Surface Temperature; Mount Sirung.

Citation: Primastika, A .A., Fadrian, D. F., Zani, F. R., and Permana, N. R. (2023). Identification of Mount Sirung Geothermal Potential based on Land Surface Temperature and 3D Gravity Model. *Jurnal Geocelebes*, 7(2), 117–129, doi: 10.20956/geocelebes.v7i2.23759

Introduction

Indonesia is a country that is crossed by the Ring of Fire so that it has a very large geothermal resource, covering about 40% of the world's potential or 29,544 MW. However, only about 7.2% is used as domestic electrical energy (Gunawan et al., 2021). Geothermal potential is shown by the existence of 117 active volcanoes scattered throughout the country, one of which is the East Nusa Tenggara area with a total potential of 980 Mwe spread over about 24 locations (Ministry of Energy and Mineral Resources, 2017).

East Nusa Tenggara ranks first in the list of 10 provinces with the lowest electrification ratio in Indonesia at 88.81% (Ministry of Energy and Mineral Resources, 2021). Therefore, the government is obliged to conduct a geothermal demand survey as one of the sources of geothermal power plants, especially in East Nusa Tenggara (Yudha et al., 2022).

One of the geothermal prospect areas in East Nusa Tenggara is Mount Sirung, located on Pantar Island at the eastern end of the Flores to Alor Island range. Mount Sirung has a hypothetical geothermal

resource of 45 Mwe. The manifestation of Mount Sirung consists of 4 hot springs located on a fault line with an average spring pH of 6.03 – 7.17 (Hadi & Kusnadi, 2015).

Research conducted by Wachidah & Minarto (2018) using the gravity method with derivative analysis shows that there is a northeast-southwest direction fault as a rock constituent of breccia tuff, lapilli tuff, tuff, dacite breccia, and andesite intrusion (Wachidah & Minarto, 2018). Another study conducted by Sidik et al. (2014) using the gravity method showed that there were three faults on three measurement tracks as an early indication of gold mineralization (Sidik et al., 2014). The mineralization process is the result of a chemical process between hydrothermal fluid and the rocks it passes through, so that primary minerals are converted into alteration minerals which can be an indication of geothermal prospect (Rey & Poluakan, 2020).

Based on the background and previous research, this study aims to analyze the geothermal potential of Mount Sirung based on surface temperature, the type of faults that control the geothermal system, and the subsurface structure of the geothermal manifestation of Mount Sirung using geophysical methods. One of the geophysical methods that can be used is the gravity method with derivative analysis correlated with Land Surface Temperature (LST) data.

Regional Geology of Mount Sirung

The lithology of Mount Sirung is composed of the Upper Miocene aged Alor Formation (Tmpa) in the form of lava, breccia, and coarse-grained passive tuff. Old volcanic rocks (Qtv) of Pleistocene age in the form of lavas, breccias, agglomerates, tuffs, volcanic sands, and rocky passive tuff. Coral limestone (Ql) and young volcanic rocks (Qhv) of Holocene age are lava, breccia, agglomerate, pebbles, sand, and volcanic ash (Koesoemadinata & Noya, 1969).

The geological structure at Mount Sirung (Figure 1) is a northeast-southwest trending fault with a distribution of volcanic rocks and limestone that overlies the overlying volcanic rocks. Another structure caused by volcanic processes is the caldera around the summit of Mount Sirung which forms a permeable zone where fluid accumulates as a geothermal prospect location (Sugianto et al., 2017; Rahadinata et al., 2019).

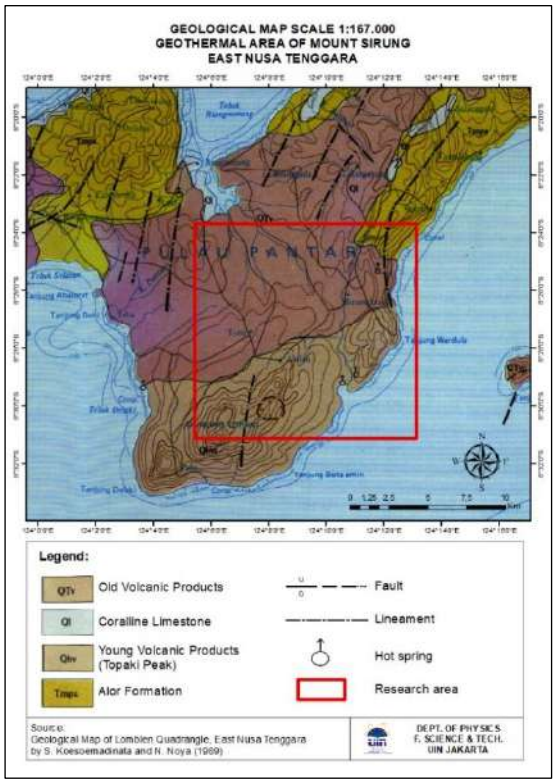

Figure 1. Geological map of Mount Sirung (Koesoemadinata & Noya, 1969).

Literature Review

Geothermal system is a system of heat in a certain volume that comes from magma kitchens, intrusion bodies, or heat due to earth's core pressure. The geothermal system component (Figure 2) consists of three main components, which is the presence of permeable reservoir rock, the presence of fluid that carries heat, and the heat source itself (Ashat et al., 2019). The freezing of magma as a heat source produces igneous rocks that conductively

flow heat to the surrounding rocks. The propagating heat heats the fluid in the reservoir (Luthfi et al., 2020). The fluid moves upward through the hot springs to the surface to meet the clay cap as a geothermal fluid trap (Sarkowi et al., 2021). Based on the geological structure, geothermal systems in Indonesia are divided into three, which are volcanic, volcanic-tectonic, and non-volcanic geothermal systems (Salam et al., 2017).

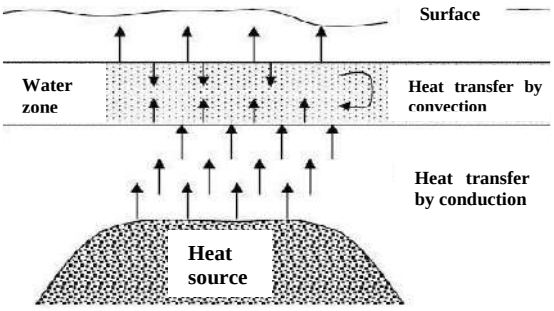

Figure 2. Water circulation or convection on geothermal system (Saptadji, 2001).

The gravity method is a method of measuring gravitational acceleration in the subsurface due to differences in rock density and differences in the earth's topography. The gravity method is based on Newton's II law:

$$F = G\frac{m_1 m_2}{r^2} \quad (1)$$

where F is the force on m_1 due to m_2 (Newton), G is the gravitational constant, m is the mass (kg), and r is the distance between m_1 and m_2 (m) (Imran et al., 2021).

Bouguer Correction (BC) is carried out to reduce the effect of gravity between the measurement point and the reference point, with the equation:

$$BC = 0.04193\ x\ \rho\ x\ h\ mGal/ft \quad (2)$$

where ρ is the Bouguer mass density (kg/m^3) and h is the height of the measurement point from the spheroid plane (m) (Sugita et al., 2020).

Free Air Correction (FAC) is performed due to altitude differences with the assumption that mass is concentrated at the center of the earth, with the equation:

$$FAC = 0{,}3086\ x\ h\ mGal \quad (3)$$

where h is the point height (m) (Sugita et al., 2020).

Terrain Correction (TC) is carried out because of the increase or decrease in measured gravity values due to irregular altitude, with the equation:

$$TC = \frac{0.04193}{n}\rho\left\{(r^2 - r^1) + \sqrt{r_1^2 + L^2} - \sqrt{r_2^2 + L^2}\right\} \quad (4)$$

where n is the number of compartments, r_1 is the inner radius (m), r_2 is the outer radius (m), and L is the height difference of measurement points (m) (Reynolds, 1997).

First Horizontal Derivative (FHD) is an analysis of the rate of change of horizontal gravity (mGal/m) based on the limit of gravity density contrast to show the geological structure of faults, with the equation:

$$\frac{\delta_g}{\delta_x}(x_n, y_n) = \sqrt{\left(\frac{\delta_g}{\delta_x}\right)^2 + \left(\frac{\delta_g}{\delta_y}\right)^2} \quad (5)$$

where $\left(\frac{\delta_g}{\delta_x}\right)^2$ and $\left(\frac{\delta_g}{\delta_y}\right)^2$ are the first derivative of gravity with respect to x and y data (Yulistina, 2018; Sehah et al., 2021).

Second Vertical Derivative (SVD) is a second derivative that can analyze shallow geological structures by interpreting the zero value as the outline of the rock body, with the equation:

$$\frac{\delta^2 \Delta g}{\delta z^2} = -\left(\frac{\delta^2 \Delta g}{\delta x^2} + \frac{\delta^2 \Delta g}{\delta y^2}\right) \quad (6)$$

where $g''_{max} > g''_{min}$ is the normal fault and $g''_{max} < g''_{min}$ is the reverse fault (Ibrahim et al., 2022; Permana et al., 2022a).

Land Surface Temperature (LST) is the average surface temperature controlled by the energy balance of atmosphere, material

emissivity, and thermal properties of the surface, with the equation:

$$T_S = \frac{BT}{\left\{1+\left[\left(\frac{\lambda BT}{\rho}\right) ln\, \varepsilon\lambda\right]\right\}} \quad (7)$$

where T_S is land surface temperature (°C), BT is brightness temperature (°C), λ is the emission wavelength, ε is emissivity, and ρ is spectral radiance (Imran et al., 2021).

Inversion modeling is an analysis process with a statistical approach in the form of curve matching between observational data and mathematical models (Hartini, 2020), with the equation:

$$m = F^{-1}(d) \quad (8)$$

where F is the operator associated with the model, m is the model calculation data, and d is the model observation data (Permana et al., 2022b). In this research, the inversion process is used to analyze the subsurface according to the results of the projection of the gravity anomaly of the research area.

Methods

The research was conducted in August 2022, with the research location at Mount Sirung, East Nusa Tenggara (9058450.00 m S – 9073207.00 m S and 621089.00 m E – 633540.00 m E) UTM 51 L zone (Figure 3) suspected of having geothermal manifestations (Ministry of Energy and Mineral Resources, 2017).

The data used is gravity satellite was obtained from the GGMPlus 2013. The amount of data used is 3819 data, consisting of gravity disturbance (gd), geoid, and Digital Elevation Model (DEM), corrected with gravity correction that produces Complete Bouguer Anomaly (CBA). Residual anomalies generated from anomaly separation are used to analyze fault types with derivative analysis in the form of First Horizontal Derivative (FHD) and Second Vertical Derivative (SVD) and for processing 3D inversion modeling of subsurface gravity data of Mount Sirung (Figure 4).

The results of gravity data processing are correlated with Land Surface Temperature (LST) data and regional geological data to analyze the subsurface geothermal structure of Mount Sirung.

Figure 3. Research area (Google Earth, 2022).

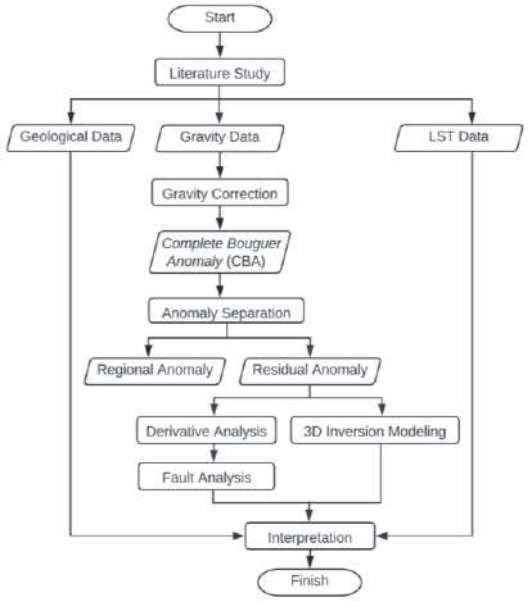

Figure 4. Research flowchart.

Results and Discussion

Complete Bouguer Anomaly (CBA) Map

Based on the results of the data processing, the complete Bouguer anomaly map (Figure 5) shows three different anomaly patterns. The low anomaly of 100.34 – 111.73 mGal is suspected as a lava interspersed with sandy tuff. The medium anomaly of 113.91 – 155.52 mGal is suspected as a breccia. The high anomaly of 157.29 – 170.87 mGal is suspected as a clay interspersed with breccia.

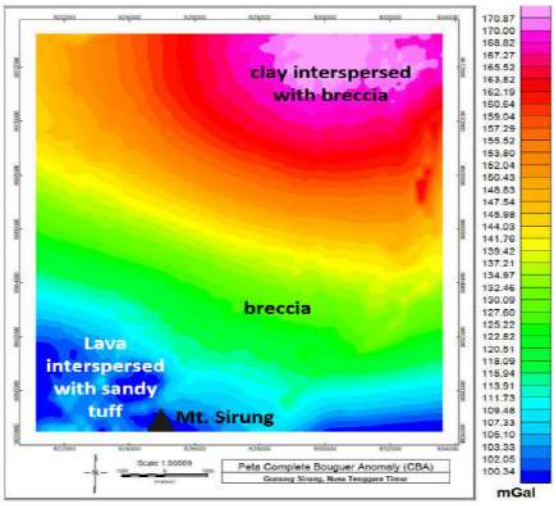

Figure 5. Complete Bouguer Anomaly (CBA) map.

Anomaly Separation

The contour of regional anomaly (Figure 6) is smoother than residual anomaly because it represents deep subsurface material, while residual anomaly represents shallow subsurface material. Separation of the anomalies is carried out with a Bandpass filter. Regional anomaly value ranges from 99.69 – 169.43 mGal.

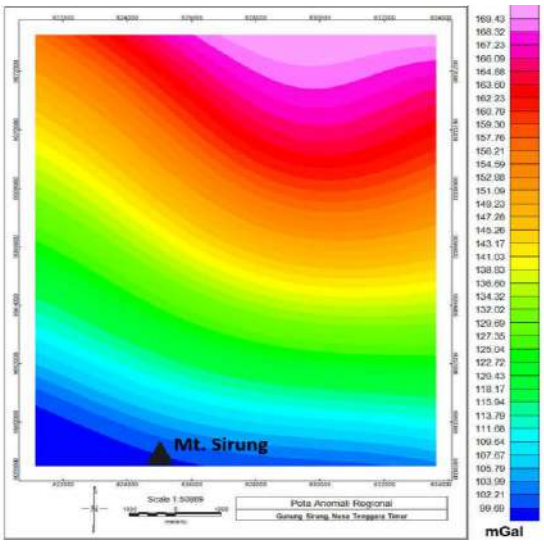

Figure 6. Regional anomaly map.

In the residual anomaly (Figure 7), low anomaly value of -5.07 – (-2.02) mGal is suspected as a lava interspersed with sandy tuff. The medium anomaly of -1.76 – 1.79 mGal is suspected as a breccia. The high anomaly of 1.97 – 5.22 mGal is suspected as a clay interspersed with breccia.

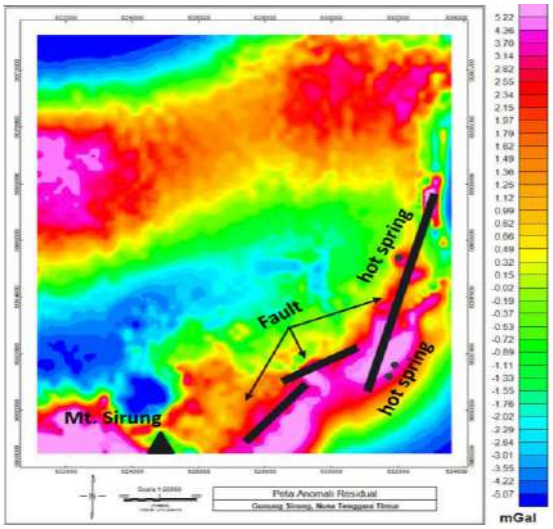

Figure 7. Residual anomaly map.

Land Surface Temperature (LST) Map

Geothermal potential can be recognized based on the distribution of surface temperature values that are higher than the surrounding area because surface temperature is associated with subsurface heat sources (Cahyono et al., 2019). Based on the results of overlaying the land surface temperature map (Figure 8) with the residual anomaly map, Mount Sirung has a surface temperature approximately 26.1 – 29.5°C. This area has a high temperature because there are manifestations of hot springs.

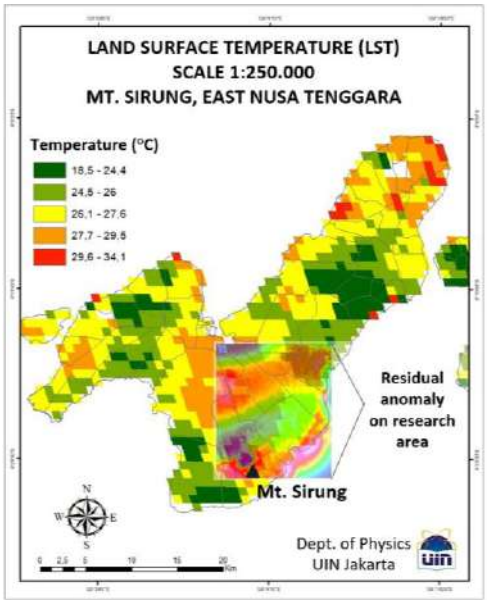

Figure 8. Land Surface Temperature (LST) map.

Derivative Analysis

Derivative analysis is carried out to determine the type of fault using the First Horizontal Derivative (FHD) (Figure 9) and Second Vertical Derivative (SVD) (Figure 10) methods by analyzing the maximum and minimum derivative values. The slicing trajectory is carried out in a northwest-southeast direction perpendicular to the main fault source (Figure 11). The main fault of Mount Sirung (Table 1 and Figure 12) is suspected to be at the contrast of low anomaly and high anomaly, which produces hot springs in the northeast and southwest directions (Koesoemadinata & Noya, 1969).

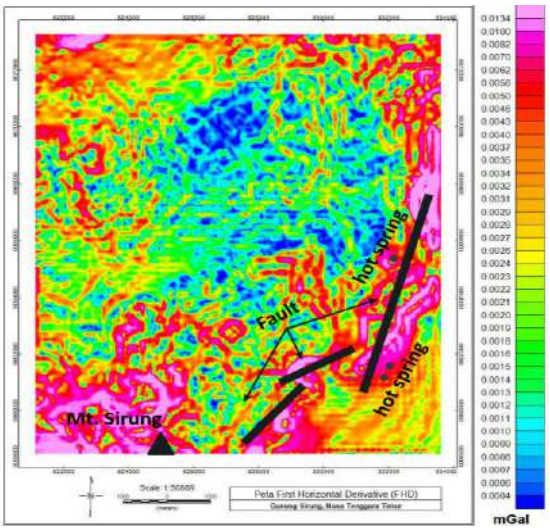

Figure 9. First Horizontal Derivative (FHD) map.

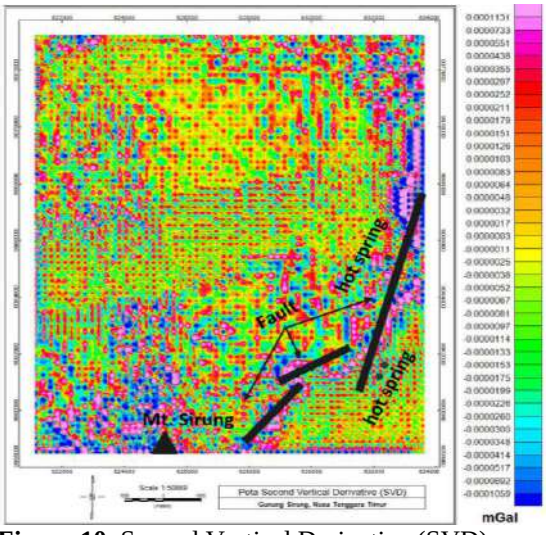

Figure 10. Second Vertical Derivative (SVD) map.

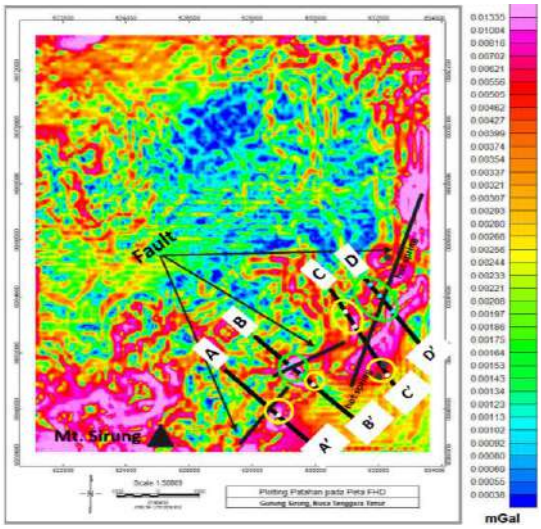

Figure 11. Fault plotting on First Horizontal Derivative (FHD) map.

Table 1. Fault analysis on Mount Sirung.

Line	Fault	Type	SVD		Coordinates	
			Max	Min	E	N
A-A'	P1	Reverse fault	1	3.1	628825.9	9059799.2
B-B'	P1	Normal fault	1	0.77	629194.8	9061560.5
	P2	Normal fault	1	0.69	629561.1	9061220.1
	P3	Reverse fault	0.12	0.27	629927.3	9060879.7
C-C'	P1	Reverse fault	0.04	0.14	630953.3	9063462.1
	P2	Reverse fault	0.16	0.32	631259.6	9062946.2
	P3	Reverse fault	0.14	0.53	632280.5	9061226.3
D-D'	P1	Normal fault	0.27	0.12	631733.5	9064423.6
	P2	Normal fault	0.6	0.09	632033.5	9064023.6
	P3	Normal fault	1	0.43	632453.5	9063463.6

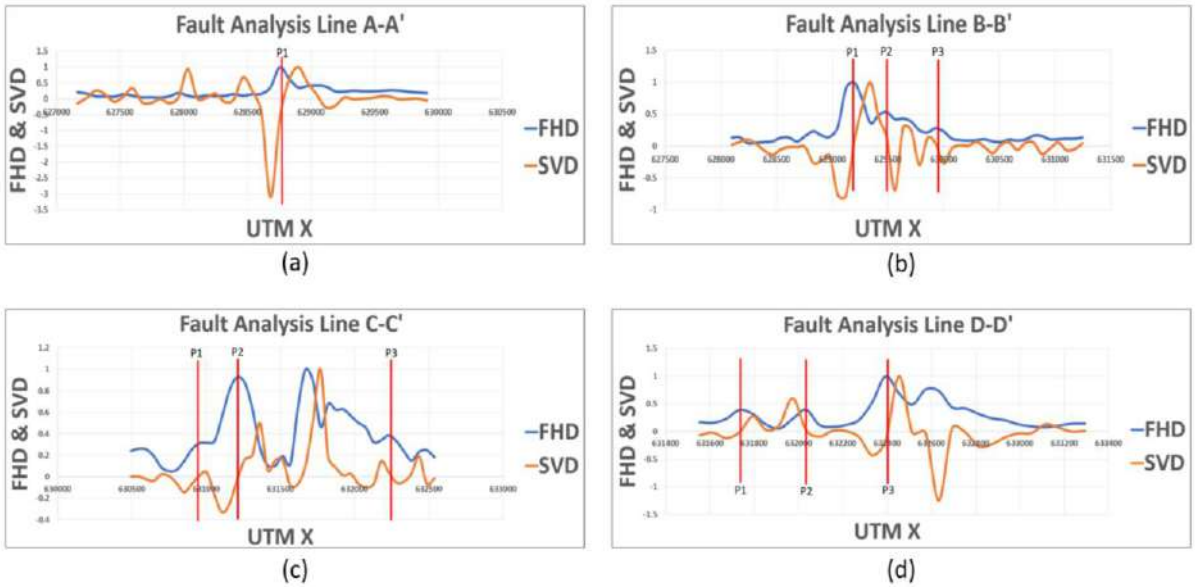

Figure 12. Fault analysis on Mount Sirung: (a) line A-A', (b) line B-B', (c) line C-C', (d) line D-D'.

3D Gravitational Inversion Modeling

Inversion modeling is used to identify the subsurface based on residual anomaly maps in three-dimensional form. This study consists of five slicing passes perpendicular to the main fault source (Figure 13–17).

The blue-green colored layer is suspected as a reservoir in the form of lava interspersed with sandy tuff with a low density of 1.98 – 2.03 g/cm^3. The white-yellow colored layer is suspected as a breccia with medium density of 2.16 – 2.21 g/cm^3. The red colored layer is suspected as a clay cap in the form of clay interspersed with breccia with high density of 2.34 – 2.39 g/cm^3.

Lava interspersed with sandy tuff has a large porosity that can store and drain large amounts of fluid. Clay interspersed with breccia is an impermeable layer, which can only store a limited amount of fluid because it has a small porosity (Darsono et al., 2017; Sugito et al., 2019).

Based on Table 2, the results of 3D gravitational inversion modeling show that there is agreement between the processed data and the theory. The low-density of Mount Sirung reservoir is located under a higher density clay cap as a trap for geothermal fluids (Sarkowi et al., 2021). The existence of geothermal manifestations can also be proven by the presence of hot springs (Figure 15) in the northeast of the study area (Koesoemadinata & Noya, 1969).

The presence of faults is characterized by the contrast of rock density between high density and low density. The fault will form a fracture to control fluid movement as the geothermal manifestation of Mount Sirung.

Isosurface is a representation of the value distribution of a material in three-dimensional form to see the distribution of each material (Sari et al., 2022). Top of reservoir modeling is depicted with an isosurface density of 2.19 g/cm^3. This modeling can show the distribution of lava interspersed with sandy tuff in the Gunung Sirung geothermal manifestation area (Figure 18).

Table 2. Depth analysis geothermal structure on Mount Sirung.

Line	Depth (m)	
	Reservoir (Lava interspersed with sandy tuff)	**Clay cap (Clay interspersed with breccia)**
L1 – L1’	600 – 1200	0 – 400
L2 – L2’	1000 – 1200	0 – 800
L3 – L3’	800 – 1400	0 – 600
L4 – L4’	700 – 1200	0 – 600
L5 – L5’	500 – 1400	0 – 400

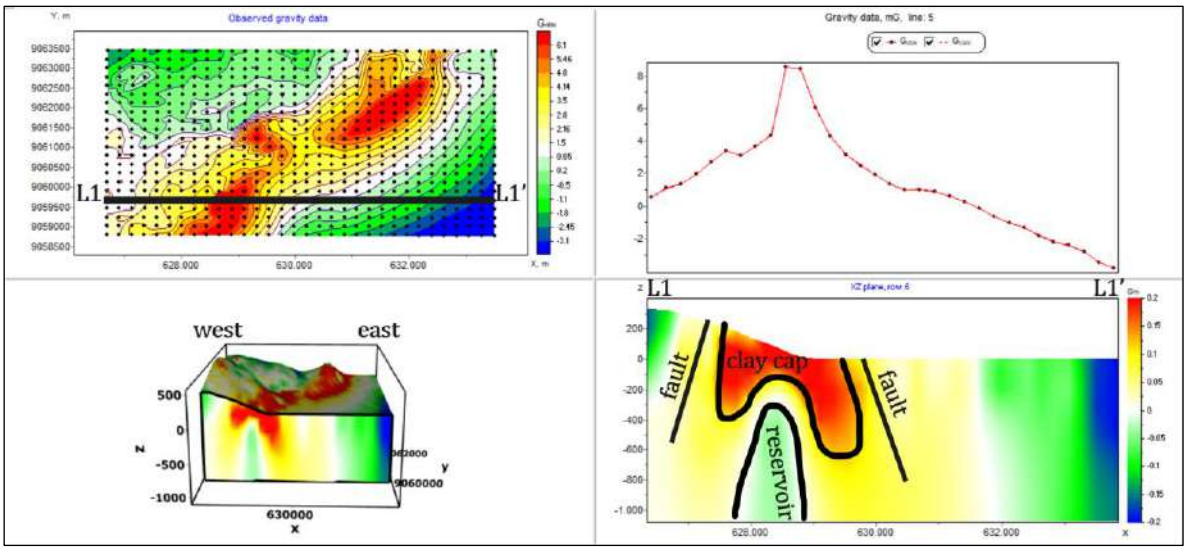

Figure 13. 3D gravitational inversion modeling line L1 – L1’ on Mount Sirung.

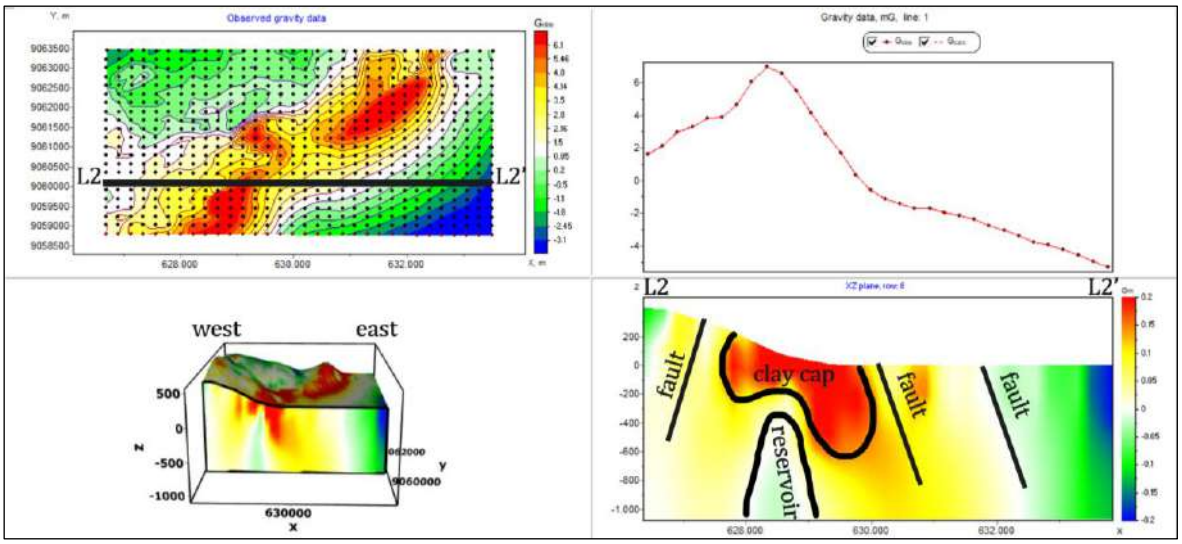

Figure 14. 3D gravitational inversion modeling line L2 – L2’ on Mount Sirung.

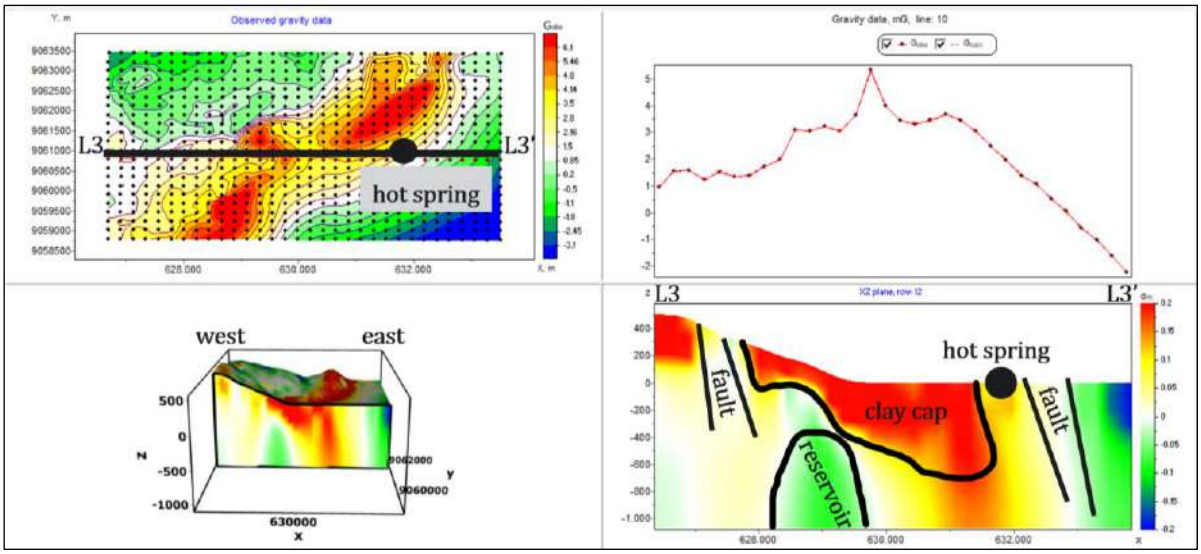

Figure 15. 3D gravitational inversion modeling line L3 – L3' on Mount Sirung.

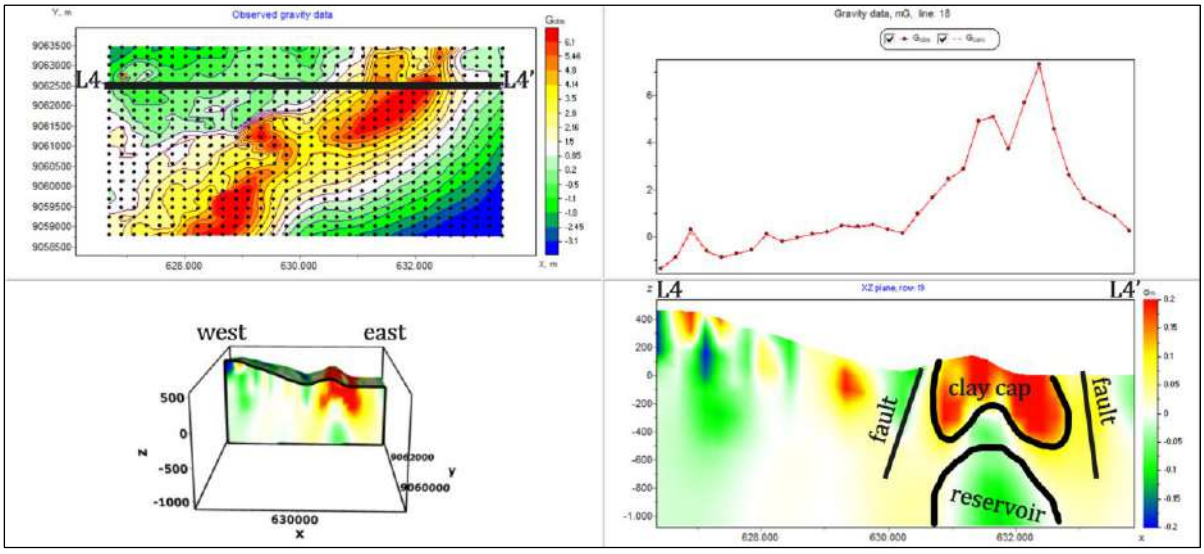

Figure 16. 3D gravitational inversion modeling line L4– L4' on Mount Sirung.

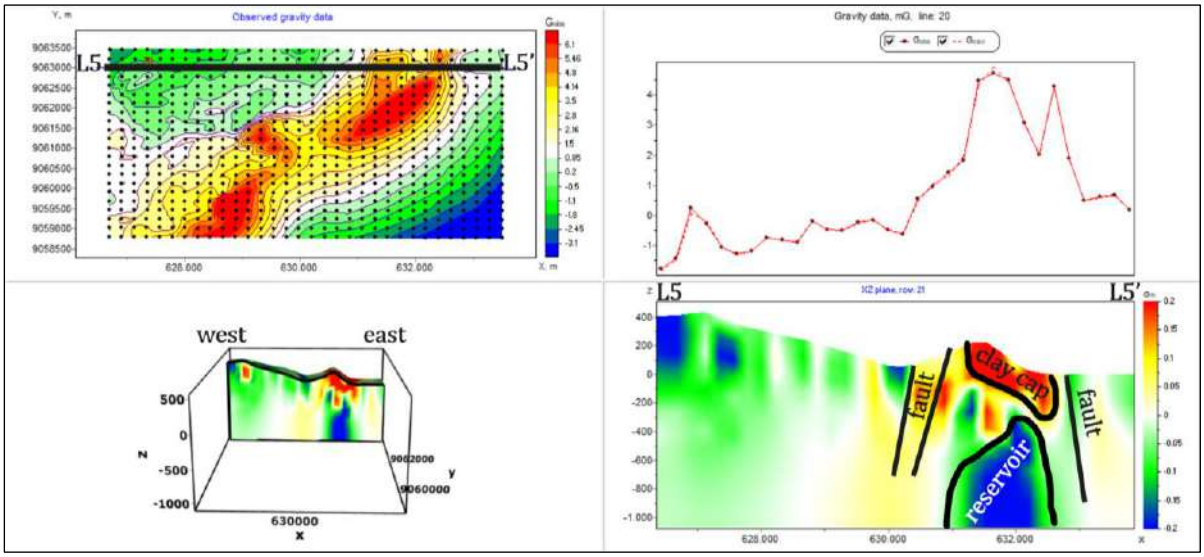

Figure 17. 3D gravitational inversion modeling line L5 – L5' on Mount Sirung.

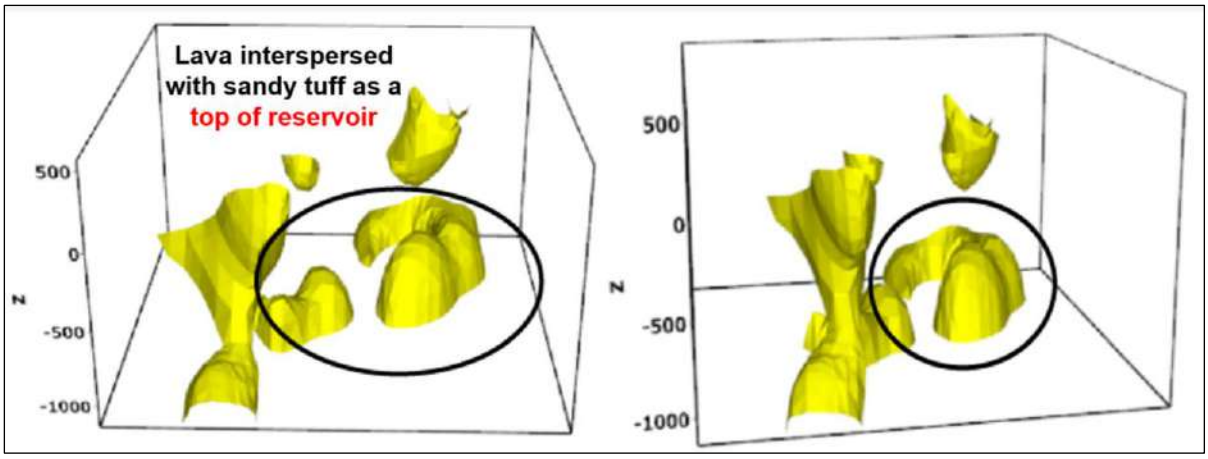

Figure 18. Isosurface top of reservoir on Mount Sirung.

Conclusion

Based on the Land Surface Temperature (LST) map, the research area at Mount Sirung has a surface temperature approximately 26.1 – 29.5°C, which is a high temperature because there are manifestations of hot springs.

Based on derivative analysis with the First Horizontal Derivative and Second Vertical Derivative methods, there are four trajectories with rising faults and normal faults as the geothermal control system of Mount Sirung in the northwest-southeast direction.

Based on 3D gravity inversion modeling, it is suspected that there are three types of rocks, which is clay interspersed with breccia as a clay cap with a density of 1.5 2.34 – 2.39 g/cm^3 at 0 – 600 m, and lava interspersed with sandy tuff as a reservoir with a density of 1.98 – 2.03 g/cm^3 at 700 – 1400 m.

Acknowledgements

The authors acknowledged PT Minelog Services Indonesia, GeoXplore Indonesia, and Syarif Hidayatullah State Islamic University Jakarta has providing facilities during the implementation of this research.

Author Contribution

Conception and data acquisition: NRP, DFF, and FRZ. Data interpretation and statistical analysis: AAP and NRP. Report writing publications: AAP. Performed the analysis: AAP, DFF, and FRZ. All authors reviewed the results and approved the final version of the manuscript.

Conflict of Interest

All authors have seen and agree with the contents of the manuscript and there is no financial interest to report. All authors certify that the submission is original work and is not under review at any other publication.

References

Ashat, A., Pratama, H. B., & Itoi, R. (2019). Updating conceptual model of Ciwidey-Patuha geothermal using dynamic numerical model. *IOP Conference Series: Earth and Environmental Science*, 254,012010. http://dx.doi.org/10.1088/1755-1315/254/1/012010

Cahyono, B. E., Jannah, N., & Suprianto, A. (2019). Analisis Sebaran Potensi dan Manifestasi Panas Bumi Pegunungan Ijen berdasarkan Suhu Permukaan dan Geomorfologi. *Natural B*, 5(1), 19–27. https://natural-b.ub.ac.id/index.php/natural-

b/article/view/452/

Darsono., Legowo, B., & Darmanto. (2017). Identifikasi Potensi Akuifer Tertekan berdasarkan Data Resistivitas Batuan (Kasus: Kecamatan Sambirejo Kabupaten Sragen). *Jurnal Fisika dan Aplikasinya*, 13(1), 34–38. http://dx.doi.org/10.12962/j24604682.v13i1.2151

Google Earth. (2022). *Research Location*. https://earth.google.com/web/search/GunungSirung

Gunawan, I., Windarta, J., & Harmoko, U. (2021). Overview Potensi Panas Bumi di Provinsi Jawa Barat. *Jurnal Energi Baru dan Terbarukan*, 2(2), 60–73. https://doi.org/10.14710/jebt.2021.11072

Hadi, M. N., & Kusnadi, D. (2015). Survei Geologi dan Geokimia Daerah Panas Bumi Pulau Pantar Kabupaten Alor, Provinsi Nusa Tenggara Timur. *Prosiding Hasil Kegiatan Lapangan Pusat Sumber Daya Geologi Tahun Anggaran*.

Hartini. (2020). Pemodelan Inversi Linier Least-Square (LS) pada Anomali Geomagnet Model Dyke. *Jurnal Hadron*, 2(2), 49–53. https://doi.org/10.33059/jh.v2i2.2689

Ibrahim, M. M., Utami, P., & Raharjo, I. B. (2022). Analisa Struktur Geologi berdasarkan Data Gravitasi Menggunakan Metode Second Vertical Derivative (SVD) Pada Lapangan Panas Bumi "X". *Jurnal Geosains dan Remote Sensing (JGRS)*, 3(2), 52–59. https://doi.org/10.23960/jgrs.2022.v3i2.76

Imran, P. B., Fernanda, E., & Sudrazat, S. D. (2021). Pengolahan Data Landsat dan Gravitasi Sebagai Indikasi Panasbumi Daerah Rana Kulan, NTT. *Jurnal Geofisika Eksplorasi*, 7(1), 41–51. https://doi.org/10.23960/jge.v7i1.10

Koesoemadinata, S., & Noya, N. (1969). *Geological Map of Lomblen Quadrangle, East Nusa Tenggara Scale 1:250.000*. Pusat Penelitian dan Pengembangan Geologi.

Luthfi, M., Haryanto, A. D., Hutabarat, J., & Siagian, H. (2020). Pemodelan Sistem Panasbumi pada Sumur ML-1, ML-2 dan ML-3 berdasarkan Analisis Petrografi dan Magnetotellurik di Lapangan Panasbumi Sorik Marapi, Kabupaten Mandailing Natal, Sumatera Utara. *Geoscience Journal*, 4(2), 154–162. http://jurnal.unpad.ac.id/geoscience/article/view/29089

Ministry of Energy and Mineral Resources. (2017). *Potensi Panas Bumi Indonesia Jilid 2*. Badan Geologi.

Ministry of Energy and Mineral Resources. (2021). *Triwulan III 2021: Rasio Elektrifikasi 99,40%, Kapasitas Pembangkit EBT 386 MW*. Siaran Pers Indonesia. https://ebtke.esdm.go.id/post/2021/11/22/3013/triwulan.iii.2021.rasio.elektrifikasi.9940.kapasitas.pembangkit.ebt.386.mw

Permana, N. R., Gunawan, B., Primastika, A. A., & Novitasari, D. (2022). Characteristics of Palu-Koro Fault based on Derivative Analysis and Euler Deconvolution Model of Gravity Data. *Journal of Physics: Conference Series*, 2377, 012041. https://doi.org/10.1088/1742-6596/2377/1/012041

Permana, N. R., Gunawan, B., Primastika, A. A., Shafa, D., Fadrian, D. F., & Zani, F. R. (2022b). Identification of Alteration Zone and Gold Mineralization based on Magnetic Anomaly and 3D Model of Geomagnetic Satellite Data Inversion of Mount Pongkor Area, West Java. *Journal of Natural Sciences and Mathematics Research*, 8(2), 94–102. https://doi.org/10.21580/jnsmr.2022.8.2.13177

Rahadinata, T., Takodama, I., & Zarkasyi, A. (2019). Penerapan Koreksi Topografi pada Data Magnetotellurik dan Analisis Data Gaya Berat dalam

Interpretasi Daerah Panas Bumi Pantar, Kabupaten Alor, Provinsi Nusa Tenggara Timur. *Buletin Sumber Daya Geologi*, 14(3), 156–168. https://doi.org/10.47599/bsdg.v14i3.290

Rey, R. B. & Poluakan, C. (2020). Identifikasi mineral batuan pada daerah manifestasi mata air panas di Koya Kecamatan Tondano Selatan Kabupaten Minahasa menggunakan sem-edx dan ftir. *Jurnal Fisika dan Terapannya*, 1(1), 12–16. https://eurekaunima.com/index.php/fista/article/view/57/29

Reynolds, J. M. (1997). *An Introduction to Applied and Environmental Geophysics.* John Wiley and Sons.

Salam, R. A., Harmoko, U., & Yulianto, T. (2017). Pemodelan 2D sistem panas bumi daerah Garut bagian timur menggunakan metode magnetotellurik. *Youngster Physics Journal*, 6(2), 143–150. https://ejournal3.undip.ac.id/index.php/bfd/article/view/17118

Saptadji, N. (2001). *Teknik Panas Bumi.* Bandung Institute of Technology Press.

Sari, H. P., Suprianto, A., & Priyantari, N. (2022). Groundwater Distribution and Potency in Faculty of Mathematics and Natural Science, Universitas Jember based on 3-Dimensional Resistivity Data Modeling. *Jurnal Berkala Saintek*, 10(1), 32–36. https://doi.org/10.19184/bst.v10i1.23025

Sarkowi, M., Sawitri, R. F., Mulyanto, B. S., & Wibowo, R. C. (2021). Wai Selabung geothermal reservoir analysis based on gravity method. *Jurnal Ilmiah Pendidikan Fisika Al-BiRuNi*, 10(2), 211–229. https://doi.org/10.24042/jipfalbiruni.v10i2.9705

Sehah., Prabowo, U. N., & Raharjo, S. A. (2021). Pemanfaatan Data Anomali Gravitasi Citra Satelit untuk Interpretasi Kualitatif Batas Cekungan Air Tanah Purwokerto-Purbalingga. Prosiding Seminar Nasional dan Call for Papers. http://jurnal.lppm.unsoed.ac.id/ojs/index.php/Prosiding/article/viewFile/1841/1600

Sidik, I. F., Susilo, A., & Sulastomo, G. (2014). Identifikasi Sesar Di Daerah Pongkor Bogor Jawa Barat Dengan Menggunakan Metode Gayaberat. *Brawijaya Physics Student Journal*, 2(1), 21–25. http://physics.studentjournal.ub.ac.id/index.php/psj/article/view/125

Sugianto, A., Takodama, I., & Rahadinata, T. (2017). Identification of Pantar Geothermal Structures Derived from Gradient Horizontal Analysis and 3D Modeling of Gravity Data. *Buletin Sumber Daya Geologi*, 12(2), 135–143.

Sugita, M. I., Janah, A. F., Rahmawati, D., Supriyadi., & Khumaedi. (2020). Analisis Data Gaya Berat di Daerah Bendan Duwur Semarang. *Journal of Research and Technology*. 6(1), 81–90. https://journal.unusida.ac.id/index.php/jrt/article/view/143/152

Sugito., Hartono., Irayani, Z., & Abdullatif, R. F. (2019). Eksplorasi potensi akuifer menggunakan metode geolistrik resistivitas di desa plana Kec. Somagede Kab. Banyumas. *Prosiding Seminar Nasional LPPM Unsoed*, 9(1), 12–22. http://jurnal.lppm.unsoed.ac.id/ojs/index.php/Prosiding/article/viewFile/1102/956

Wachidah, N. & Minarto, E. (2018). Identifikasi Struktur Lapisan Bawah Permukaan Daerah Potensial Mineral dengan Menggunakan Metode Gravitasi di Lapangan "A", Pongkor, Jawa Barat. *Jurnal Sains dan Seni ITS*, 7(1), B32–B37. http://dx.doi.org/10.12962/j23373520.v7i1.28673

Yudha, S. W., Tjahjono, B., & Longhurst, P. (2022). Unearthing the Dynamics of

Indonesia's Geothermal Energy Development. *Energies*, 15(14), 5009. https://doi.org/10.3390/en15145009

Yulistina, S. (2018). Studi Identifikasi Struktur Geologi Bawah Permukaan untuk Mengetahui Sistem Sesar berdasarkan Analisis First Horizontal Derivative (FHD), Second Vertical Derivative (SVD), dan 2,5D Forward Modeling di Daerah Manokwari Papua Barat. *Jurnal Geofisika Eksplorasi*, 4(2), 173–186. http://dx.doi.org/10.23960/jge.v4i2.15

ISSN: 2579-5821 (Print)
ISSN: 2579-5546 (Online)
URL address: http://journal.unhas.ac.id/index.php/geocelebes
DOI: 10.20956/geocelebes.v7i2.25476

Jurnal Geocelebes Vol. 7 No. 2, October 2023, 130 – 137

Assessment of Landslide Susceptibility Microzonation using Microtremor Measurements Along Mountain Road in North Bengkulu–Lebong, Bengkulu Province

Ulfa Nuramadani[1], Halauddin[2]*, Suhendra[2]*, Darmawan Ikhlas Fadli[2], Ardika Pratama Panjaitan[2], Jesika Erni Elfrita Sinaga[2]

[1]Study Program of Physiscs, Faculty of Mathematics and Natural Sciences, University of Bengkulu, 38371, Indonesia.
[2]Study Program of Geophysics, Faculty of Mathematics and Natural Sciences, University of Bengkulu, 38371, Indonesia.

*Corresponding author. Email: halaukualasatu@gmail.com; suhendra@unib.ac.id

Manuscript received: 16 February 2023 ; Received in revised form: 2 March 2023; Accepted: 28 March 2023

Abstract

Based on the geological condition, the research location on the North Bengkulu - Lebong crossing is on the Sumatra fault zone that extends from south to north, which causes this area to have a morphological shape and topography of hills and hills extreme slopes. This research results in landslide-prone micro zonation based on GSS and PGA values obtained from Horizontal-to-Vertical Spectral Ratio (HVSR) method measurements. The research was conducted by measuring 25 research sites. The results of Peak Ground Acceleration (PGA) values processing at the research site, between 0.14 gal - 0.53 gal. Locations with the potential for landslides, shown in blue (0.14-0.29 gal), are located in several spots of the research site. The distribution of Ground Shear Strain (GSS) at the study site is evenly distributed at a value of 10^{-4}, which indicates that the study site is prone to cracking and ground movement. In the distribution of GSS values, it is suspected that the location in the dark red color (10^{-3}) has the highest potential to experience repeated landslides. Based on the results of the calculation of PGA and GSS values on the North Bengkulu - Lebong crossing, the points of landslide-prone locations can be known so that disaster mitigation can be carried out at these locations to reduce the risk that will occur.

Keywords: landslide; microtremor; microzonation; mountain road.

Citation: Nuramadani, U., Halauddin., Suhendra., Fadli, D. I., Panjaitan, A. P., and Sinaga, J. E. E. (2023). Assessment of Landslide Susceptibility Microzonation using Microtremor Measurements Along Mountain Road in North Bengkulu–Lebong, Bengkulu Province. *Jurnal Geocelebes*, 7(2):130–137, doi: 10.20956/geocelebes.v7i2.25476

Introduction

Bengkulu is one of the provinces located on the island of Sumatra, with most of its mountainous territory having a high potential for landslides (BPBD, 2019). One of the areas with a high potential for landslides is the North Bengkulu - Lebong crossing (Ariyanto & Joni, 2019). Based on geological conditions, the North Bengkulu - Lebong crossing is located in the Sumatran fault zone that extends from the south to the north, which causes this area to have a hilly morphological and topographic shape and slopes with high steepness so that it can endanger road users because of the high potential for landslides.

Landslides can occur due to the movement of land masses or can be defined as the displacement of slope-forming materials that move down and out of the slope (Trianda et al., 2018). Apart from that, several human activities can be a triggering factor for landslides, such as logging trees on slopes without reforestation (Nurjanah & Mursalin,

2021), mining of rocks, soil, or other mining goods that cause slope instability (Susanti & Miardini, 2019), the level of soil and rock wetness (Iswahyudi et al., 2021), changes in the slope of the area due to development, and excessive loading from buildings in mountainous areas (Hadi et al., 2021).

Other factors influencing landslides are slip surface or shear surface and high rainfall (Nishimura et al., 2022). The North Bengkulu - Lebong crossing is an important crossing that connects Bengkulu Province with other provinces using land transport. The North Bengkulu - Lebong crossing is one of the most heavily traveled routes, so the resulting vibrations can trigger landslides due to ground movements that change the physical properties of the land surface (Kristie & Budiman, 2021). Landslides that occur on the North Bengkulu - Lebong crossing will have a significant impact on the community because they hamper traffic and have a severe impact on economic problem, for example, landslides that occurred in 2022, causing impacts felt by the community due to disruption of the land transportation system which is covered by landslide material. The preliminary survey results found several locations of the North Bengkulu - Lebong Regency crossing road that experienced landslides, shown in Figure 1.

The impact of landslides can be minimized by conducting disaster mitigation and management efforts (Zulfa et al., 2022). One of the disaster mitigation efforts can be made using the Horizontal-to-Vertical Spectral Ratio (HVSR) method (Hartantyo et al., 2020). The HVSR method can be used to determine complex geological structures and determine the thickness of sedimentary layers obtained from data in the form of natural vibrations originating from natural sources and human activities (Silitonga, 2022). The HVSR method has two important methods obtained from the processing results: dominant frequency (f_0) and amplification (A_0). In addition, microtremor data can be used to find seismic susceptibility index, sediment layer thickness, Peak Ground Acceleration (PGA), and Ground Shear Strain (GSS), which are used as parameters for analysis in identifying potential landslide areas (Refrizon et al., 2013). The landslide-prone zonation areas can be mapped based on the PGA and GSS values obtained from the HVSR method.

Figure 1. Documentation of the location of the North Bengkulu - Lebong crossing road that experienced a landslide on 26 March 2022.

A landslide investigation using the HVSR method has been conducted (Natasya et al., 2022) on the Bengkulu - Kepahiang causeway. The interpretation results showed that in the Bengkulu - Kepahiang causeway area, the average value obtained is relatively medium-high, so it is less likely if a landslide occurs at a depth of 0 to 30 meters. However, at a depth of 0 to 5 meters, the average value is relatively low-medium, so the area is prone to landslides. Therefore, the HVSR method is often used in case studies of landslides and earthquakes (Hadi et al., 2018).

Local Geology Setting

The Barisan Mountains dominate the geology of the Bengkulu sheet, the corner is part of the South Sumatra Basin, and the west is part of the Bengkulu Basin. The study area is a plateau located around the

Sumatra fault zone, associated with the Musi-Keruh and Ketaun faults and covered by a mixture of Quaternary alluvium and volcanic materials. Plio-Plistocene volcanic rocks cover the plateau. Elevation on this plateau is up to 500 meters above the MSL. The oldest unit exposed is the Seblat Formation which includes marine sediments derived from clastic volcanic rocks of the Barisan Mountains and locally inserted limestone. The Simpangaur Formation consists of shallow marine to muddy freshwater sediments and lignite coal. The Plio-Plistocene-aged Bintunan Formation taxonomically overlies the Simpangaur Formation. Based on the geological map of the Bengkulu sheet on the North Bengkulu - Lebong cross-section, there are also Bintunan Formation and Andesite-Basalt volcanic rocks, which can be seen in Figure (2). This lane forms the Barisan volcanic chain that stretches along the western part and is parallel to the long axis of the island of Sumatra. It is an area of magmatic activity during the Tertiary and Quaternary, which may indicate the maturity of the volcanic arc (Gafoer et al., 2007).

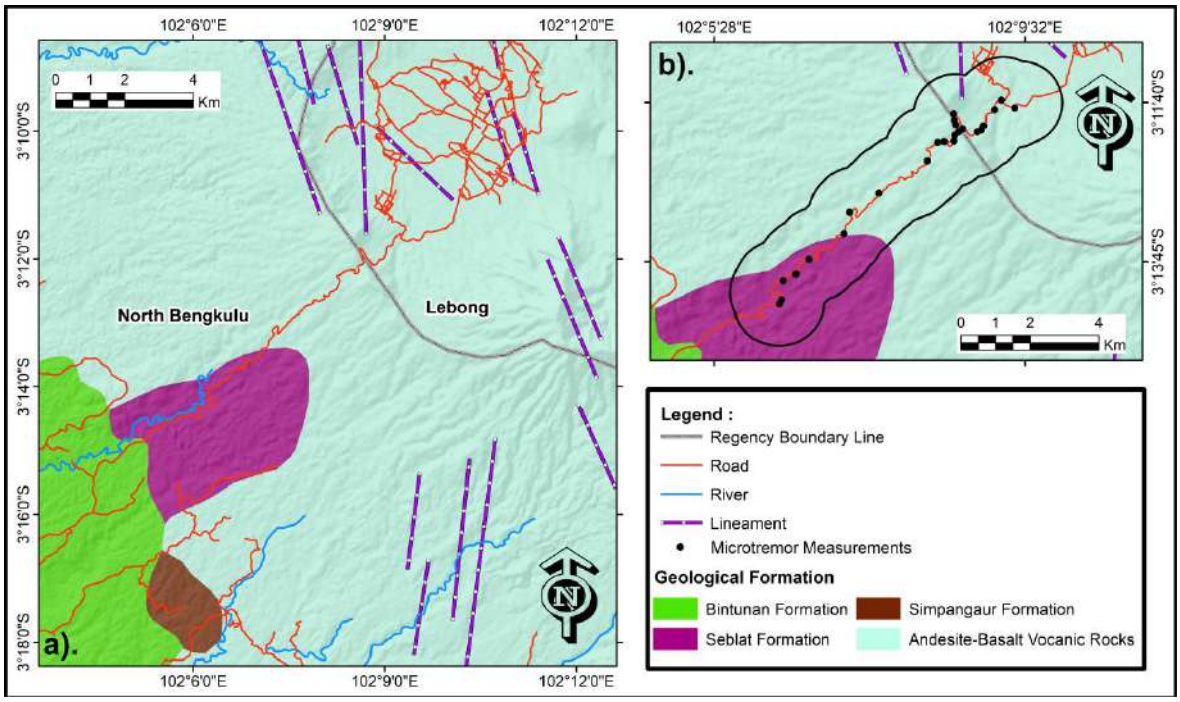

Figure 2. a). Research geological map (modified from Gafoer et al. (2007); b). HVSR site measurements.

Materials and Methods

The research was conducted in the mountainous area of the North Bengkulu - Lebong Regency of Bengkulu Province measurements using microtremor as many as 25 measurement points along the research location road. Data were collected for 30 minutes at each measurement point with a sampling frequency of 100 Hz. The structure of subsurface rock layers can be described by variations in shear wave velocity obtained from forward computation and HVSR inversion of microtremor data. Rocks with complex properties, like igneous rocks, will have low landslide-prone factor values. On the other hand, soft rocks like clay and silt have high landslide-prone factor values (Sugianto & Refrizon, 2021).

The dominant frequency (f_0) and amplification (A_0) values obtained from HVSR analysis are used as input data to calculate the seismic susceptibility index (K_g). The seismic susceptibility index is an index that describes the level of

susceptibility of the surface soil layer to deformation during an earthquake (Tanjung et al., 2019). The seismic susceptibility index can be calculated using the following Equation (1) (Asnawi et al., 2020):

$$Kg = \frac{Ag^2}{fg}\frac{1}{\pi^2 vb} \quad (1)$$

Based on the seismic vulnerability index obtained, the soil structure or subsurface rock condition at the research location can be known.

Peak Ground Acceleration (PGA) value is calculated using earthquake parameters with the most significant magnitude at the epicenter distance closest to the research location (Prakoso, 2018). The PGA formula is as follows Equation (2) (Douglas, 2021):

$$\alpha_g = \frac{5}{\sqrt{T_g}} 10^{(0{,}6\,M)-\left(1{,}6+\frac{3{,}6}{R}\right)\log R+0{,}167-\frac{1{,}8}{R}} \quad (2)$$

The Ground Shear Strain (GSS) value describes the geological conditions at a location (Sugianto et al., 2021). GSS is one of the physical parameters that shows the level of rock susceptibility to stretching or shifting from its equilibrium point due to earthquakes. GSS is often used to describe the characteristics of soil layers or the potential for liquefaction and landslides at a location. The GSS value is obtained by multiplying the seismic susceptibility index with the PGA because the relationship is directly proportional. The greater the value of the seismic vulnerability index and PGA, the greater the GSS value and will cause the soil layer to deform (Gemintang et al., 2022). The GSS formula is as follows Equation (3) (Nakamura, 2008):

$$\boldsymbol{\gamma} = Kg \times (10^{-6}) \times \alpha \quad (3)$$

Results and Discussion

The measurement results at this research location are data from vibration signals analyzed using Sesaray Geopsy for signal filtering without noise. The results of signal filtering were analyzed using the HVSR method, resulting in H/V curves, predominant frequency values (f_0), and amplification factors (A_0). The value of the predominant period is used as a parameter to determine the Peak Ground Acceleration (PGA) value, which is calculated using Equation (2). The PGA values at the 25 research points were inputted in the PGA map shown in Figure 3. The results of processing the PGA values in the surface layer show PGA values between 0.14 g - 0.53 g.

Low PGA values are shown in dark blue with values of 0.14 g - 0.19 g, medium PGA values in green with values of 0.34 g - 0.39 g, and high PGA values in dark brown with values of 0.48 g - 0.53 g. The PGA value is directly proportional to the dominant frequency value. This parameter shows that areas with low PGA values have low dominant frequency values. Areas with low PGA values have thick sedimentary layers and a small density of constituent rocks. Areas with small PGA values have seismic wave velocities that propagate through the rock layers resulting in significant amplification and seismic wave vibrations that travel below the ground surface for a long time, which can cause more significant damage.

The PGA value in this study was used to find the Ground Shear Strain (GSS) value. GSS value is a parameter related to the dynamic nature of the soil. If an area has a high GSS value, then the area is prone to stretching or shifting movements. The stretching and shifting will cause the rock structure to deform and experience landslides. However, if the GSS value is smaller, the soil layer will be difficult to deform.

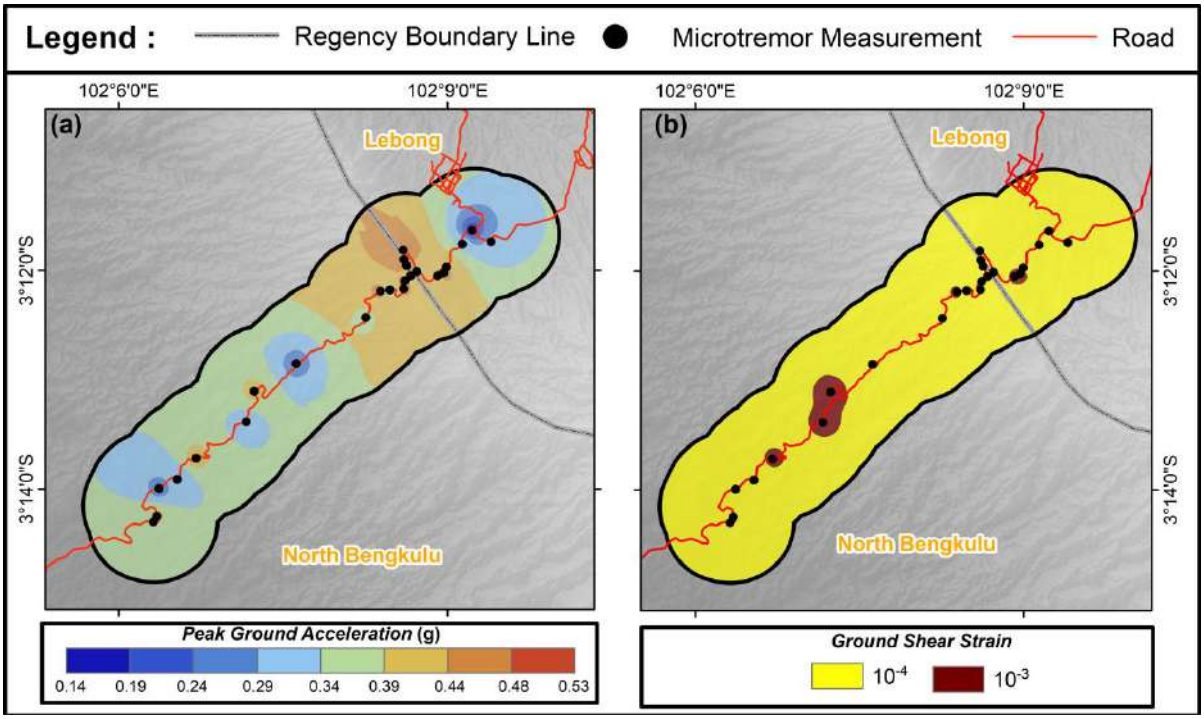

Figure 3. a). Peak Ground Acceleration (PGA) distribution map; b). Ground Shear Strain (GSS) distribution map.

Based on the distribution map of GSS values, the research site has elastic-plastic soil dynamics when looking at the relationship between GSS values and the nature of soil dynamics. Therefore, cracks and subsidence can occur if the nature of soil dynamics is elastic-plastic. Judging from the results of the GSS distribution map overlay, areas with high GSS values are shown in dark red. The even distribution of GSS values at 10^{-4} indicates that the study site is prone to cracking and ground movement. The rock structure is susceptible to seismic vibrations and mechanical vibrations caused by transport vehicles, changing the physical properties of the rock. The triggering factor for ground movement at the study site can be cracking and landslide collapse. The GSS 10^{-4} values evenly distributed along the North Bengkulu-Lebong mountain road are not all susceptible to landslides. The research location with a high susceptibility to landslides is in the area with a GSS value of 10^{-3}. This condition causes some areas along the mountain road to experience landslides with a small volume of material. The factor that causes the size of the landslide can be caused by the angle of the slope on the side of the road. The North Bengkulu-Lebong crossroad is located between regencies that are mountainous areas with steep slopes and a high potential for landslides.

Conclusion

The distribution of PGA values in the research location is dominated by green color, which has a landslide risk if no disaster management is done. In addition, some dark blue colored points show a high risk of landslides. Meanwhile, based on the distribution map of GSS in the study area, several dark red colored points show the potential severe danger of landslides. Therefore, based on the distribution map of PGA and GSS on the North Bengkulu - Lebong crossing, it is possible to identify locations prone to landslides so that disaster mitigation can be carried out at those locations to reduce the risk.

Acknowledgements

The authors thank the Research Institutions and Community Service

(LPPM), University of Bengkulu, for the grant for Research Fundamentals 2007/UN30.15/PP/2022 to support this work financially. The author also thanks the Physics Laboratory of the University of Bengkulu for providing equipment for this work. Finally, we thank the anonymous reviewers and academic editors who took the time and effort to review the manuscript. We appreciate all valuable comments and suggestions that improve the manuscript's quality.

Author Contribution

Conceptualization, U.N., H., S., and D.I.F.; Methodology, D.I.F, S., and H.; Software, D.I.F; Investigation, and Data Acquisition, A.P.P., and S.; Writing – Original Draft Preparation, U.N., D.I.F, and J.E.E.S.; Writing – Review & Editing, H., and S.; Visualization, D.I.F.; Supervision, H., and S.; Project Administration, H., and S.; and Funding Acquisition, H., and S.

Conflict of Interest

The authors declare no conflict of interest.

References

Ariyanto, S. V., & Joni, I. (2019). Zone Landslide Analysis Using Geophysical Method and Analysis of Soil Type for Disaster Mitigation In Waru Pamekasan. *Indonesian Journal of Applied Physics*, 9(02), 68–75. https://doi.org/10.13057/ijap.v9i2.34520

Asnawi, Y., Simanjuntak, A. V. H., Umar, M., Rizal, S., & Syukri, M. (2020). A Microtremor Survey to Identify Seismic Vulnerability Around Banda Aceh Using HVSR Analysis. *Elkawnie: Journal of Islamic Science and Technology*, 6(2), 342–358. https://doi.org/10.22373/ekw.v6i2.7886

BPBD. (2019). *Badan Penanggulangan Bencana Daerah Provinsi Bengkulu*.

Douglas, J. (2021). *Ground Motion Prediction Equations 1964–2021*. Department of Civil & Environmental Engineering Imperial College London.

Gafoer, S., Amin, T. C., & Pardede. (2007). *Peta Geologi Lembar Bengkulu, Sumatera*. Pusat Penelitian dan Pengembangan Geologi. Pusat Penelitian dan Pengembangan Geologi.

Gemintang, K. N., Hanatha, F. D., Indriatmoko, T. W., Qurrotu'aeni, W. S., Azis, B. N. L., & Hamdalah, H. (2022). Identifikasi Zona Rawan Amblesan Berdasarkan Parameter Hvsr Dan Ground Shear Strain Di Daerah Gua Pindul. *Jurnal Geosaintek*, 8(3), 232–241. https://doi.org/10.12962/j25023659.v8i3.14395

Hadi, A. I., Brotopuspito, K. S., Pramumijoyo, S., & Hardiyatmo, H. C. (2018). Regional landslide potential mapping in earthquake-prone areas of kepahiang regency, Bengkulu Province, Indonesia. *Geosciences (Switzerland)*, 8(6), 219. https://doi.org/10.3390/geosciences8060219

Hadi, A. I., Brotopuspito, K. S., Pramumijoyo, S., & Hardiyatmo, H. C. (2021). Determination of Weathered Layer Thickness around the Landslide Zone using the Seismic Refraction Method. *IOP Conference Series: Earth and Environmental Science*, 830(1), 012022. https://doi.org/10.1088/1755-1315/830/1/012022

Hartantyo, E., Khayati, N. N., Nur, R., & Novita, S. (2020). Kajian Nilai Percepatan Puncak di Daerah Kulon Progo Utara, Yogyakarta, Indonesia, Berbasis Peta Gempa Nasional 2017 dan Pengukuran Mikrotremor. *Positron*, 10(2), 148–154. https://doi.org/10.26418/positron.v10i2.43310

Iswahyudi, S., Widagdo, A., & Laksono,

F. A. T. (2021). Sosialisasi Analisis Penyebab Bencana Longsor Desa Sirau, Karangmoncol, Purbalingga. *Jurnal Dharma Bakti-LPPM IST AKPRIND*, 4(1), 7–17.

Kristie, H. J., & Budiman, A. (2021). Karakteristik Sifat Fisis Tanah Daerah Potensi Longsor di Jalan Raya Sumbar Riau Nagari Koto Alam, Sumatera Barat. *Jurnal Fisika Unand*, 10(1), 123–129. https://doi.org/https://doi.org/10.25077/jfu.10.1.123-129.2021

Nakamura, Y. (2008). On the H/V spectrum. *The 14th World Conference on Earthquake Engineering*, 1–10.

Natasya, I. D., Puspa, M., Elona, L., Gatra, G., & Refrizon, P. (2022). Upaya Mitigasi Bencana Longsor Jalan Lintas Bengkulu-Kepahiang Berdasarkan Kecepatan Gelombang Geser (Vs). *Newton-Maxwell Journal of Physics*, 3(1), 33–37. https://doi.org/https://doi.org/10.33369/nmj.v3i1.21243

Nishimura, I., Noguchi, T., Ono, Y., & Kohno, M. (2022). Subsurface Structures Based on Microtremor Observations in Landslide Area of Tandikat , West Sumatra, Indonesia. *GEOMATE Journal*, 22(90), 57–62.

Nurjanah, S., & Mursalin, E. (2021). Pentingya Mitigasi Bencana Alam Longsor Lahan: Studi Persepsi Mahasiswa. *Jurnal Basicedu*, 6(1), 515–523. https://doi.org/10.31004/basicedu.v6i1.1937

Prakoso, B. A. (2018). *Analisis Tingkat Risiko Tanah Longsor Berdasarkan Nilai* Peak Ground Acceleration *(PGA) di Desa Purwosari Kecamatan Girimulyo Kabupaten Kulon Progo*. Universitas Negeri Yogyakarta.

Refrizon, Arif, I. H., Kurnia, L., & Tria, O. (2013). Analisis Percepatan Getaran Tanah Maksimum dan Tingkat Kerentanan Seismik Daerah Ratu Agung Kota Bengkulu. *Prosiding Semirata FMIPA Universitas Lampung*, 323–328.

Silitonga, B. (2022). Pengukuran Seismik Dengan Metode HVSR Untuk Pendugaan Bencana Gempa Bumi. *Jurnal Rekayasa Konstruksi Mekanika Sipil (JRKMS)*, *5*(2), 103–111. https://doi.org/10.54367/jrkms.v5i2.2184

Sugianto, N., & Refrizon. (2021). Struktur Kecepatan Gelombang Geser (Vs) di Daerah Rawan Gerakan Tanah (Longsor) Jalan Lintas Kabupaten Bengkulu Tengah-Kepahiang. *Indonesian Journal of Applied Physics*, 11(2), 134–142. https://doi.org/https://doi.org/10.13057/ijap.v11i2.41699

Sugianto, N., Refrizon, Mase, L. Z., & Anggeraini, S. (2021). The updated zonation of seismic vulnerability index and ground shear strain at Bengkulu City, Indonesia. *AIP Conference Proceedings*, 2320, 040022. https://doi.org/10.1063/5.0037597

Susanti, P. D., & Miardini, A. (2019). Identifikasi Karakteristik dan Faktor Pengaruh pada Berbagai Tipe Longsor. *AgriTECH*, 39(2), 97–107. https://doi.org/10.22146/agritech.40562

Tanjung, N. A. F., Yuniarto, H. P., & Widyawarman, D. (2019). Analisis Amplifikasi Dan Indeks Kerentanan Seismik Di Kawasan Fmipa Ugm Menggunakan Metode HVSR. *Jurnal Geosaintek*, 5(2), 60–67. https://doi.org/10.12962/j25023659.v5i2.5726

Trianda, O., Prastowo, R., & Novitasari, S. (2018). Identifikasi Ketebalan Lapisan Lapuk di Daerah Kalirejo, Kulonprogo Berdasarkan Pengukuran Mikrotremor dalam Upaya Mitigasi Tanah Longsor. *Prosiding Seminar Nasional ReTII ke-13 2018*, 246–253. https://journal.itny.ac.id/index.php/ReTII/article/view/892

Zulfa, V. A., Widyasamratri, H., &

Kautsary, J. (2022). Mitigasi Bencana Berdasarkan Tingkat Risiko Bencana Tanah Longsor. *Jurnal Kajian Ruang*, 2(2), 154–169. https://doi.org/http://dx.doi.org/10.30659/jkr.v2i2.26532

ISSN: 2579-5821 (Print)
ISSN: 2579-5546 (Online)
URL address: http://journal.unhas.ac.id/index.php/geocelebes
DOI: 10.20956/geocelebes.v7i2.25371

Jurnal Geocelebes Vol. 7 No. 2, October 2023, 138 – 153

Middle Eocene Nannofossil Assemblages Responding to Depositional Dynamics of the Elat Formation, Maluku

Ratih C.F. Ratumanan[1*], Vijaya Isnaniawardhani[2]*, Budi Muljana[3]

[1]Master Program in Geological Engineering, Padjadjaran University, 45363, Indonesia
[2,3]Department of Geosciences, Padjadjaran University, 45363, Indonesia

*Corresponding author. Email: ratihcfr@gmail.com, vijaya.isnania@unpad.ac.id

Manuscript received: 8 February 2023; Received in revised form: 6 June 2023; Accepted: 10 July 2023

Abstract

The Kei Besar Island is mainly composed of the Elat Formation carbonate rocks. This research was conducted to determine the nannofossils assemblages in the Elat Formation to interpret the depositional dynamics during its formation. Lithological observations and sampling for nannofossil analysis were carried out on three measured stratigraphic sections: Section 1 - Hollat, Section 2 - Ngurdu, and Section 3 - Mata Hollat. A total of 47 species assigned to 25 genera of nannofossils were identified in 45 selected samples. The succession of the Elat Formation in the study area formed at NP16 to N17 or Middle Eocene. Stratigraphic reconstruction supported by biostratigraphy analysis shows that Section 3 at the lower (NP16 to NP 17), Section 2 in the middle part (NP 17), and Section 1 at the upper (NP 17). R-mode cluster analysis of nannofossils defined four species clusters (assemblies A, B, C and D) that tend to occur together. Q-mode cluster analysis defined five depth-distribution clusters (1, 2, 3, 4, and 5), each deposited under similar conditions. Based on large foraminifera, the succession was formed in fore reef setting in neritic bathymetric zone. Coarsening and thickening upward supported by the nannofossil assemblages indicate depositional dynamics which tend to be shallower. Reworked fossils, commonly found at the lower of the Elat Formation, show the mechanism of turbid currents in early deposition.

Keywords: depositional environment; Kei Besar; Middle Eocene; nannofossil.

Citation: Ratumanan, R. C. F, Isnaniawardhani, V. and Muljana, B. (2023). Middle Eocene Nannofossil Assemblages as A Depositional Environment Indicator of Elat Formation, Maluku. *Jurnal Geocelebes*, 7(2):138–153, doi: 10.20956/geocelebes.v7i2.25371

Introduction

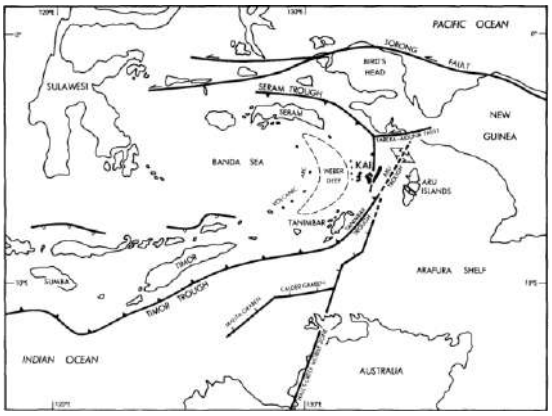

Figure 1. Kei Islands in the Banda Arc Tectonic Framework (modified from Charlton et al., 1991).

Geographically, the Kei Islands, Southeast Maluku, are in the arc zone of the Banda Arc System. The Banda Arc is located at the subduction zone between three plates in the earth's crust: the Indo-Australian Plate, the Eurasian Plate, and the Pacific Plate. The Banda Arc is divided into two regions, which are the Inner Banda Arc (volcanic) and the Outer Banda Arc (non-volcanic) (Charlton, 2016) (Figure 1).

The Kei Islands consist of Kei Besar Island and Kei Kecil Island. The Elat Formation occupies the most extensive area on Kei Besar Island. The Elat Formation is mainly composed of calcilutite and calcarenite, with marl intercalations. The thickness of this formation is estimated at 600 – 800 m. A thinning upward of marl indicates the depositional environment changes

(Achdan & Turkandi 1994). The Elat Formation refer as pelagic or hemipelagic carbonate rocks deposited on the distal continental slope setting, which is slowly shallowing. Based on the content of planktonic foraminifera, it is known that this formation was formed in the Middle to Late Eocene. Middle Eocene reworked benthic foraminifera fossils are found in calcilutite (Achdan and Turkandi, 1994; Charlton et al., 1991; Kurniasih et al., 2019).

Pelagic carbonate rocks as the Elat Formation usually contain many nannofossils (Agnini et al., 2017). These taxa are very small marine microfossils, oval, rod, star-shaped, nannofossil belongs to the protist kingdom, phylum hatophyta comporised of calcite plates generally produced by unicellular marine algal *coccolithophore* as a parent cell, limestone composisition, with a size of ±1-25 μm (Isnaniawardhani, 2017; Widhiyatmoko et al., 2023)

Nannofossil analysis provides good accuracy in determining relative ages of marine sediment because of the abundance, rapid evolution and wide distribution (Isnaniawardhani, 2015; Raffi et al., 2022). Quantitative analysis of nannofossils can be used to support the paleo-depositional environments, Paleotemperature and oceanographic reconstructions in addition to foraminifera (Isnaniawardhani et al., 2020; Karatsolis & Henderiks, 2023; Lowery et al., 2014; Choiriah & Maha, 2020; Villa et al., 2021; Imai et al., 2013; Rosmadi et al., 2022; Alves et al., 2016; Mandur et al., 2022).

The sampel of this research is the marine pelagic sediment of Elat Formation. This study focused on quantitatively analysing nannofossil assemblages, supported by lithostratigraphic data, to interpret changes in the depositional environment. The results of this study can then be used as a reference in reconstructing depositional environments based on nannofossil assemblages.

Materials and Methods

Field observations and sampling were carried out on 3 sections where the Elat Formation was continuously exposed. Five samples were collected from the northern part of Kei Besar Island (Section 1 or Hollat), 10 samples from the central part (Section 2 or Ngurdu), and 30 samples from the southern part (Section 3 or Mata Hola) (Figure 2). These samples were selected that contain assemblages of high-diversity nanofossils, and represent the upper, middle and lower stratigraphic positions of the formation.

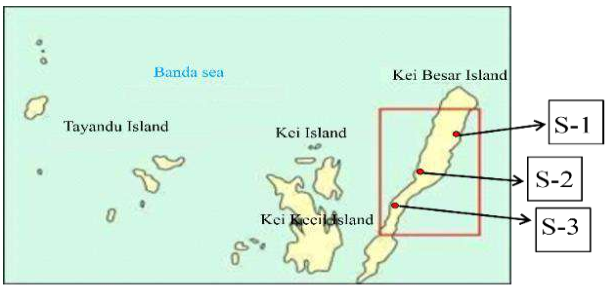

Figure 2. Three sections of observation and sampling on Kei Besar Island, which are: Hollat (S-1), Ngurdu (S-2), and Mata Hollat (S-3)

The samples were prepared using the *quick smear slide method* (Suchéras-Marx et al., 2016; Young, 1998; Ikhwana et al., 2022; Farida et al., 2019). Observation of nannofossils was carried out using a polarizing microscope at 1000x magnification (Sheward., et al 2017; Gibbs et al., 2013). The determination of nannofossils refer to previous researchers such as Perch-Nielsen (1985), Young (1998), Nannotax3 (2014), Faris et al. (2021). Age determination is based on established biostratigraphy zones (Martini, 1971; Perch-Nielsen, 1985; Okada & Bukry, 1980; Agnini et al., 2014, Raffi et al., 2016).

Cascading counting method was applied in calculating the number of individuals of each species. The total abundance of

individuals in the sample is classified into four classes (Ladner, 2007) (Table 1).

Table 1. Classification of individual abundance (Ladner, 2007).

Category	Number specimens per view
Abundant (A)	>10 per view
Common (C)	1-10 per view
Few (F)	1 specimen per 1-10 views
Rare (R)	< 1 specimen per 10 views

Diversity is calculated using the Shannon-Weaver index, as follows:

$$H' = -\Sigma\, p_i \ln(p_i) \qquad (1)$$

where:
H' : Shannon-Weaver index
Σ : means "amount."
ln : natural logs
p_i : the proportion of the entire community consisting of species *i*

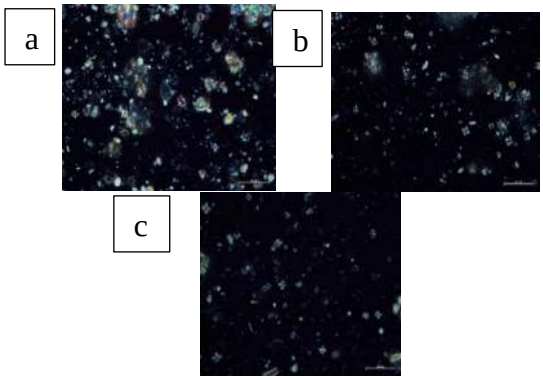

Figure 3. Photomicrograph of nannofossil preservation (a) Poor preservation (*Poor*) as shown in sample N4, (b) Medium preservation (*Fair*) on the sample MH16, (c) *Good* preservation on the sample MHL10

The data were processed using the *cluster analysis method* to compare the composition of taxa (*R-mode*) and the presence of distribution nannofossil assemblages in the sample (*Q-mode*) (Clark, 2018). The depositional environment is interpreted by integrating the results of the quantitative analysis to obtain accurate results (Kontakiotis et al., 2013). Preservation (Figure 3) of nannofossil was observed to provide an accurate interpretation (Roth, 1984) Preservation of nannofosil related to carbonate content in water-mass (Toffanin et al., 2013.), which were classification of preservation into three categories (Ladner, 2007) (Table 2).

Table 2. Classification of nannofossil preservation (Ladner, 2007).

Category	Description
Good (G)	little/no dissolution or *overgrowth*
Fair (F)	specimen shows some streaking and *overgrowth*
Poor (P)	specimen shows excessive streaking or *overgrowth*

Nannofossils cannot yet indicate depth in detail due to the nature of planktonic life. Therefore, large foraminifera analysis is also used for environmental (Hairul, 2022). Large foraminifera analysis was also carried out to strengthen the interpretation results. These fossils are founded in limestone intercalations. The determination of fossils refers to the systematic and occurrences of larger foraminifera.

Results and Discussion

Lithostratigraphy

The Elat Formation is composed of alternating calcarenite and calcareous clays, with limestone intercalations. Calcarenite is white-grey, fine to coarse sand, generally fine to medium in size, with parallel laminations, contains trace fossils, and thickness generally ranges from 5-70 cm. Towards the upper part, the grain size gets coarser, and the layer gets thicker, up to 1 meter. Fresh grey carbonate clay, weathered brownish, rich in fossils, poorly layered, generally <20 cm in thickness and decreases (<1 cm) upward. In several locations exposed white-brown limestone, containing large foraminifera and mollusk cells, generally < 10 cm thick (Figure 4–5, 8).

Stratigraphic reconstruction of the observation section based on the direction of the slope of the rock layers with a north-northeast trending trend and a gentle slope (< 50°). On section 3, the fold axis is found. The field observation indicates a

depositional dynamic which tends to be shallower (Figure 6–7, 9).

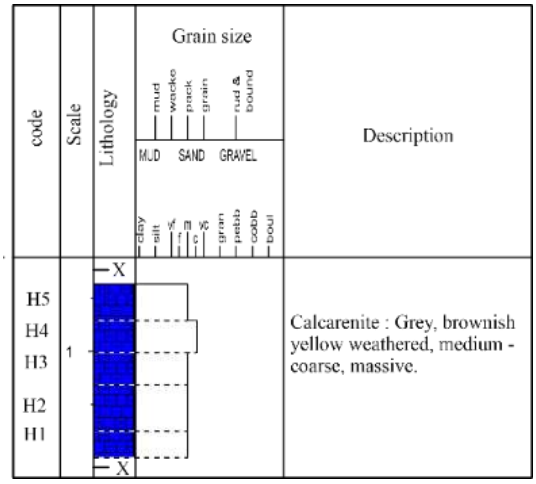

Figure 4. Lithostratigraphy S-1 Hollat.

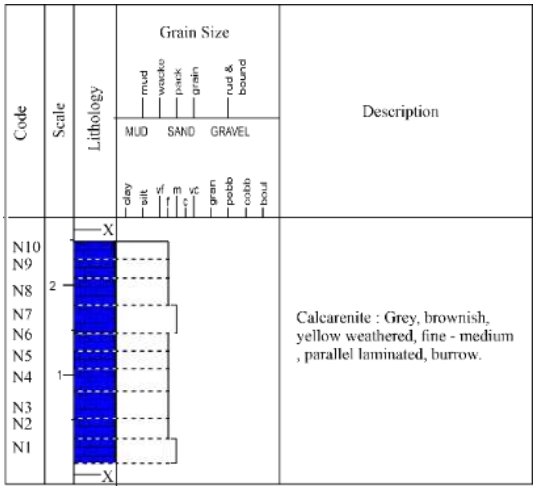

Figure 5. Lithostratigraphy S-2 Ngurdu.

Figure 6. Massive calcarenite on S-1 Hollat.

Figure 7. Calcarenite beds at S-2 Ngurdu.

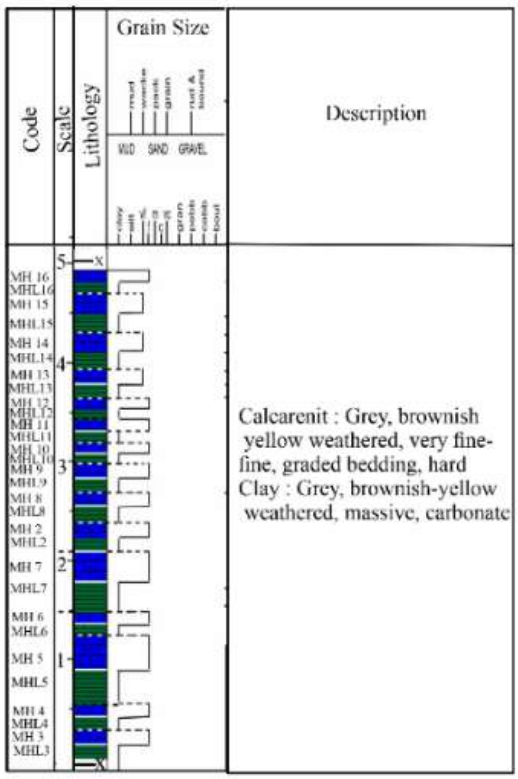

Figure 8. Lithostratigraphy S-3 Mata Hollat.

Figure 9. Intercalations of calcarenite and clay at S-3 Mata Hollat.

Table 3. Preservation, abundance, and individuals' number of nannofossil on S-1, -2, and -3.

Code	Preservation	Abundance	*Reticulofenestra umbilica*	*Reticulofenestra dictyoda*	*Reticulofenestrabisecta*	*Reticulofenestra stavensis*	*Reticulofenestra minuta*	*Reticulofenestru hampdanensis*	*Reticulofenestra lockeri*	*Cyliycargolithus floridanus*	*Cydicargolithus luminis*	*Coccilithus pelagicus*	*Coccilithus aspida*	*Sphenolithus spiniger*	*Sphenolithus obtusus*	*Sphenolithus morfiormis*	*Sphenolithus radians*	*Sphenolithus furcatholoides*	*Sphenolithus orphaknolensis*	*Helicosphaera compacta*	*Helicosphaera lopotha*	*Chiasmolithus grandis*	*Chiasmolithus titus*	*Chiasmolithus solitus*	*Umbilicosphaera protoannulus*	*Coronocyclus nitiscens*	*Clausicoccus subdistichus*	*Calcidiscus bicircus*	*Pontosphaera plana*	*Pontosphaera multipora*	*Pontosphaera pectinata*	*Pontosphaera wechesensis*	*Discoaster kuepperi*	*Discoaster tani nodifer*	*Discoaster tanii*	*Braarudosphaera bigelowii*	*Scyphosphaera apsteini*	*Nanotetrina sp*	*Isthmolithus unipons*	*Ericsonia formosa*	*Zygrhablithus bijugatus*	*Lanternithus minutus*	*Isthmolithus sp*	*Blackites inflata*	*Tribrachiatus orthotylus*	*Rhabdosphaera gladius*	*Micrantholitus astrum*	*Fasciculithus tympaformis*	*Dictyococites scrippae*
H5	F	C	2	9	5	0	1	1	0	7	2	4	0	6	4	2	7	5	1	4	4	0	0	0	0	0	1	0	0	0	0	0	0	0	4	0	0	0	5	5	2	0	0	0	0	0	0	0
H4	F	C	1	9	4	0	1	0	0	2	1	4	4	5	0	3	2	2	0	4	2	0	0	0	2	0	1	0	2	0	0	0	0	0	0	0	20	1	0	0	5	5	0	0	0	0	0	0	0	1
H3	F	C	2	11	4	0	1	1	0	7	2	3	1	5	1	3	4	1	1	3	4	1	0	0	0	0	2	0	0	0	0	0	0	2	0	9	0	0	0	0	4	3	0	0	0	0	0	1	0	1
H2	F	C	2	8	5	0	0	0	0	8	1	2	2	6	0	3	2	1	1	2	2	0	0	0	0	0	1	1	2	0	0	0	2	3	1	13	0	0	0	0	2	2	1	0	0	0	0	2	0	1
H1	G	C	0	9	4	0	2	0	0	7	1	5	0	5	0	2	3	3	0	4	0	1	0	0	0	0	0	0	0	0	0	0	0	0	0	20	0	0	0	0	4	3	0	0	0	0	0	0	0	0
N10	F	C	2	15	5	1	0	0	0	10	1	4	0	3	2	0	0	1	1	0	1	3	0	1	0	1	2	0	1	0	0	0	0	0	0	3	1	0	1	6	1	1	0	1	0	0	1	0	0	1
N9	G	C	4	22	10	0	8	3	1	19	1	2	0	4	1	1	0	1	1	2	0	3	0	1	1	0	0	0	1	0	0	0	0	3	0	2	0	0	0	4	1	1	0	0	0	0	0	0	0	1
N8	P	A	5	20	5	1	2	3	0	10	8	5	0	9	1	3	0	0	3	3	3	1	0	0	3	2	2	1	1	0	0	0	0	0	0	3	0	0	1	4	3	1	0	0	0	0	0	0	0	0
N7	P	C	2	13	7	2	5	1	0	10	1	8	0	3	2	3	1	0	1	4	0	0	1	0	1	2	1	0	2	0	0	0	0	0	0	3	1	2	0	5	2	0	0	0	0	0	2	0	2	0
N6	G	A	4	20	12	1	2	4	0	23	6	3	1	5	1	2	0	2	0	3	0	2	0	0	0	1	2	0	0	0	0	0	0	0	1	1	0	0	0	6	1	0	0	0	0	0	0	0	0	0
N5	F	A	7	15	5	0	1	0	0	26	3	7	0	9	0	7	0	0	3	0	1	1	1	1	2	1	3	0	0	0	0	0	0	0	0	3	0	0	0	10	2	0	0	0	0	0	0	0	0	0
N4	P	A	4	22	7	3	4	3	1	14	2	8	0	3	0	3	0	1	0	3	2	2	0	0	0	1	2	0	3	0	0	0	0	2	0	4	0	0	0	7	2	2	0	0	0	0	0	1	1
N3	G	C	7	21	10	1	4	3	0	15	1	10	0	4	0	4	0	0	0	2	2	0	0	0	0	0	2	0	0	0	0	0	1	0	0	0	3	0	0	0	6	3	1	0	0	0	0	0	0	2
N2	G	C	4	15	20	3	2	0	0	10	2	6	2	3	0	2	0	1	0	1	0	0	0	0	0	0	2	1	0	0	0	0	0	0	0	2	0	0	0	5	0	0	0	0	0	0	0	0	0	0
N1	F	C	4	16	10	5	1	4	0	11	4	6	1	5	0	4	0	0	1	2	0	0	0	0	0	2	3	1	2	0	0	0	0	0	1	5	0	0	0	7	2	1	0	0	0	1	0	0	1	0
MH16	F	A	12	26	10	4	0	1	0	35	2	8	1	8	0	4	0	0	2	1	1	0	0	1	3	4	2	0	2	0	1	1	0	1	2	2	0	0	0	9	0	8	0	0	1	0	0	0	0	0
MHL16	G	A	7	30	18	4	0	1	0	40	2	10	3	3	0	4	0	0	7	0	1	0	1	0	1	0	3	0	0	2	0	0	0	0	0	2	0	0	0	7	0	4	0	0	0	0	1	2	0	0
MH15	P	A	3	41	9	1	0	3	0	30	9	2	1	6	3	6	0	2	0	0	2	0	0	1	2	1	0	0	0	0	0	0	0	0	0	0	0	1	4	8	3	1	0	3	0	4	0	4	0	0
MHL15	G	A	5	35	4	8	0	0	0	24	4	10	0	7	1	0	0	2	2	1	2	0	0	2	1	3	4	1	4	1	0	0	0	2	3	2	1	0	7	10	1	9	0	1	2	1	1	0	0	0
MH14	F	C	1	30	11	3	0	0	0	20	2	5	0	4	1	1	2	2	2	1	0	0	0	0	0	7	5	0	4	3	0	0	0	0	2	0	0	1	0	2	3	3	5	0	2	0	0	0	6	0
MHL14	G	A	2	38	10	1	0	0	0	28	4	8	0	2	0	2	0	0	0	0	2	0	0	0	3	7	2	1	0	0	0	0	0	1	0	0	0	0	4	10	0	4	0	0	0	0	0	1	0	0
MH13	F	C	5	40	10	0	0	0	0	34	10	6	1	6	0	3	2	2	2	1	1	1	0	0	2	2	2	0	1	0	0	0	0	0	0	2	2	0	0	2	2	2	0	0	1	0	1	0	0	0
MHL13	G	A	4	50	18	3	0	0	0	42	1	12	0	4	0	1	1	0	2	0	3	0	0	0	0	2	4	2	0	0	0	0	0	2	0	1	0	0	0	10	0	4	0	0	0	0	1	0	0	0
MH12	F	C	3	23	6	3	0	2	3	19	4	6	1	2	0	2	0	0	1	0	2	1	0	0	1	0	1	0	0	0	0	0	0	1	0	2	0	0	0	3	1	1	0	0	0	0	0	0	0	0
MHL12	G	C	2	16	9	3	0	2	0	11	4	4	1	6	0	2	0	1	1	2	0	1	1	0	4	3	2	0	3	1	0	0	0	0	0	2	2	0	1	4	0	1	0	0	0	0	0	0	0	0
MH11	F	C	1	30	11	9	0	0	0	25	5	8	0	4	0	3	1	0	2	0	1	1	2	1	2	1	4	0	0	0	0	0	0	1	0	3	0	1	3	8	0	0	0	0	2	0	0	0	0	0
MHL11	F	A	10	32	15	2	0	0	0	21	6	17	0	8	0	2	0	2	1	2	2	0	0	1	1	16	2	0	1	0	0	0	0	2	0	0	0	2	1	8	0	4	0	0	0	0	1	1	0	0
MH10	G	C	2	22	9	1	0	0	0	14	4	6	0	6	0	2	1	0	1	0	0	1	0	0	0	1	0	0	2	0	0	0	0	1	0	0	0	0	0	9	11	0	0	1	0	0	0	0	0	0
MHL10	G	A	7	35	19	3	0	2	0	16	3	20	0	8	0	5	1	3	4	0	1	0	1	0	3	9	0	5	1	0	0	0	0	0	0	2	0	0	1	8	0	0	0	0	2	0	0	0	0	0
MH9	F	A	1	35	11	2	0	1	0	25	3	9	0	1	0	0	0	1	4	1	0	1	0	0	1	2	0	0	0	0	0	0	0	1	0	1	1	0	4	12	1	0	0	1	0	0	1	1	0	0
MHL9	G	A	10	33	15	3	2	2	0	28	6	15	0	9	0	4	0	3	2	1	1	1	1	0	0	5	9	2	3	0	0	0	0	0	0	1	0	0	0	8	6	0	0	0	0	0	0	0	0	0
MH8	F	C	9	24	10	3	0	0	0	9	4	18	0	2	0	1	0	0	5	1	1	0	1	0	3	3	3	1	1	1	0	0	0	0	0	0	0	0	2	12	0	5	0	0	0	1	0	0	0	0
MHL8	F	A	9	32	20	4	0	0	0	27	4	16	0	8	0	2	0	0	1	0	0	0	2	0	3	1	3	2	1	1	0	0	0	2	0	3	0	0	0	29	0	1	0	0	0	0	0	0	0	0
MH2	G	C	2	30	5	1	1	0	0	12	4	2	0	4	1	1	1	2	2	0	3	0	0	0	0	1	0	1	0	0	0	0	0	0	0	0	0	0	1	2	3	1	0	0	0	0	0	0	0	0
MHL2	G	C	7	70	10	3	2	3	0	21	0	17	0	0	1	0	0	1	0	0	0	0	0	0	3	1	3	0	0	0	0	0	0	0	0	1	1	0	0	11	0	0	0	0	0	0	0	0	0	0
MH7	G	C	2	35	12	2	2	0	0	21	4	5	1	9	0	1	0	0	0	0	1	0	0	2	0	0	0	2	3	0	0	0	0	0	0	1	0	0	3	5	1	2	0	0	0	0	0	0	0	0
MHL7	F	A	4	77	10	2	0	2	0	20	3	5	3	3	0	3	0	3	0	0	1	0	0	0	0	0	3	2	0	0	0	0	0	0	0	1	0	0	0	21	1	4	0	0	0	0	0	0	0	0
MH6	F	C	0	20	7	0	0	1	0	16	2	8	7	7	1	4	0	2	8	0	1	0	0	0	0	0	1	1	0	0	0	0	0	0	0	1	1	0	1	8	2	0	0	0	0	0	0	0	0	0
MHL6	F	A	0	40	12	0	0	0	0	15	9	23	0	18	0	0	0	0	3	0	2	0	0	0	7	1	0	0	3	0	0	0	0	0	0	0	0	0	5	14	2	4	2	0	0	0	0	0	0	0
MH5	P	C	0	49	13	0	0	0	0	26	4	3	0	8	2	4	0	0	0	0	3	0	0	0	0	0	0	0	1	0	0	0	0	0	0	0	0	0	0	3	2	0	1	0	0	1	0	0	0	0
MHL5	F	C	0	70	9	0	0	0	0	40	0	10	0	1	1	2	0	0	2	0	0	0	0	0	0	0	1	0	1	1	0	0	0	0	0	0	0	0	0	9	0	2	0	0	0	0	1	0	0	0
MH4	F	C	4	36	6	0	1	0	0	16	6	17	0	10	0	2	0	0	4	0	2	0	1	4	2	3	0	0	4	1	0	0	1	0	0	0	0	0	0	4	1	7	0	1	1	0	0	0	0	0
MHL4	G	C	1	32	11	2	0	1	0	25	5	10	0	4	0	4	0	0	3	0	4	0	0	1	0	0	0	0	0	2	0	0	0	0	0	1	0	0	0	8	0	2	0	1	0	0	0	0	0	0
MH3	F	A	7	30	12	8	0	0	0	15	5	4	0	8	0	2	0	3	7	0	1	0	7	6	1	0	1	0	2	0	0	0	0	0	0	0	6	3	3	15	1	3	0	0	0	0	0	0	0	0
MHL3	F	A	3	50	10	4	1	0	0	20	6	14	0	6	0	4	0	0	7	0	2	0	0	5	3	2	3	0	4	0	2	0	0	0	0	0	0	2	0	0	4	2	1	0	0	0	0	0	0	0

Nannofossil assemblages

In this study, nannofossil identified from the 45 selected samples were classified into 25 genera and 47 species (Table 3) in alphabetical order as follows:

- Genus *Blackites* (*B. inflata*)
- Genus *Braarudosphaera* (*B. bigelowii*)
- Genus *Calcidiscus* (*C. bicircus*),
- Genus *Chiasmolithus* (*C. grandis, C. solitus,* and *C. titus*)
- Genus *Clausicoccus* (*C. subdistichus*)
- Genus *Coccolithus* (*C. aspida,* and *C. pelagicus*)
- Genus *Coronocyclus* (C. *nitiscens*)
- Genus *Cyclicargolithus* (*C. floridanus,* and *C. luminis*)
- Genus *Dictyococcites* (*D. scrippsae)*
- Genus *Discoaster* (*D. kuepperi*, *D. tanii* and *D. tanii nodifier*)
- Genus *Ericsonia* (*E. formosa*)
- Genus *Fasciculithus* (*F. tympaniformis*)
- Genus *Helicosphaera* (*H. compacta*, and *H. lophota*)
- Genus *Isthmolithus* (*I. sp* and *I. unipons*)
- Genus *Lanternithus* (*L. minutus*)
- Genus *Micrantholithus* (*M. astrum*)
- Genus *Nanotetrina*
- Genus *Pontosphaera* (*P. multipora, P. pectinata*, *P. plana,* and *P. wechesensis*)
- Genus *Reticulofenestra* (*R. bisecta, R. dictyoda, R. hampdenensis*, *R. lockerii, R. minuta, R. stavensis,* and *R. umbilica*)
- Genus *Rhabdosphaera* (*R. gladius*)
- Genus *Scyphosphaera* (*S. apsteini*)
- Genus *Sphenolithus* (*S. furcatolithoides, S. moriformis*, *S. obtusus*, *S. orphaknolensis, S. radians*, and *S. spiniger*)
- Genus *Tribrachiatus* (*T. orthostylus*)
- Genus *Umbilicosphaera* (*U. protoannulus*)

- Genus *Zygrhablithus* (*Z. bijugatus*)

Biostratigraphy/ age identification

The marker species selected from the nannofossils assemblages were: *Reticulofenestra umbilica* and *Helicosphaera compacta.* Based on the presence of these species, the succession of the Middle Eocene Elat Formation can be grouped into two zones (Ratumanan, et al., 2022) (Table 4), which are:

a. *Reticulofenestra umbilica* Zone (NP16, or 43.06 to 38.7 million years ago)
b. *Helicosphaera compacta* Zone (NP17, 38.7 to 37.9 million years ago).

Rock succession on S-3 (southern part of Kei Besar Island) can be distinguished into the *Reticulofenstra umbilica Zone* (NP16) at the lower part, and the *Helicosphaera compacta* Zone (NP17) at the upper part. The all succession of Sections-1 and 2 includes the *Helicosphaera compacta* Zone (NP17).

This biostratigraphy analysis corelate to the stratigraphic reconstruction based on field data which shows the rocks are getting younger towards the north.

Table 4. Biostratigraphic zone on the three observation sections of the Elat Formation.

Sections	Epoch	Zone	Biozone
S-1 Hollat S-2 Ngurdu	Middle Eocene	NP17	Presence *Chiasmolithus grandis* (38.7 mya)
S-3 Mata Hollat			First appearance *Helicosphaera compacta* (37.9 mya)
		NP16	Appearance *Reticulofenestra umbilica* (43.06 mya)

Cluster Analysis

a. R-mode

For this cluster analysis, a similarity matrix was conducted based on relative abundance of species. This classification allows the characterization of four clusters (A, B, C, and D) which appear to coexist (Figure 10) of species that preferentially occur together.

Cluster A is characterized by an association of many placolith-bearing species (*Reticulofenestra umbilica, R. stavensis, R. minuta, R. hampdanensis, R. lockeri, Cyclicargolithus luminis, Cocolithus aspida, Helicosphaera compacta, H. lopotha, Chiasmolithus grandis, C. titus, C. solitus, Umbilicosphaera protoannulus, Coronocyclus nitiscens, Clausicoccus subdistichus, Calcidiscus bicircus, Pontosphaera plana, P. multipora, P. pectinate, P. wechesensis, Isthmolithus unipons, Ericsonia formosa, Isthmolithus* sp. *, Blackites inflata,* and *Dictyoccocites scripsae*), and *Sphenolithus obtusus, S. moriformis, S. radians, S. furcatholoides S. orphaknolensis, Discoater kuepperi, D. tani nodifer, D. tanii, Braarudosphaera bigelowii, Scyphosphaera apsteini, Nanotetrina* sp.*, Zygrhablithus bijugatus, Lanterminuthus minutus, Tribrachiatus orthotylus Rhabdosphaera gladius, Micrantholitus astrum,* and *Faschitulithus tympaformis.*

Small placoliths are a good indicator of environmental conditions rich in nutrients in carbonate complexes (Okada, 2000; Aizawa et al., 2004) *Helicosphaera, Umbilicosphaera* and *Discoaster* are usually used to mark the neritic zone (Aizawa et al., 2004) The dominant *Discoaster* characterizes warm conditions (Pratiwi & Sato, 2016; Shepherd et al., 2021; D'Onofrio et al., 2021; Schneider et al., 2013). *Zygrhablithus bijugatus* indicated in low nutrient with open ocean envirotment (Gibbs et al., 2016; Fioroni et al., 2015), Reticulofenestra umbilica is temperate taxa (Bordiga et al., 2015; Senemari & Mejía-Molina, 2022). *Umbilicosphaera* is known as a tropical

oligo taxon. *Braarudosphaera bigelowii* and *Reticulofenestra minuta* represent the photic zone species rich in nutrients (Kanungo & Young, 2017; Auer et al., 2014; Senemari & Jalili, 2021), The *Reticulofestra* group characterizes cold water (Umoh, 2023), *Chiasmolithus* is a characteristic of cold water (Khorassani et al., 2014; Kasem et al., 2022).

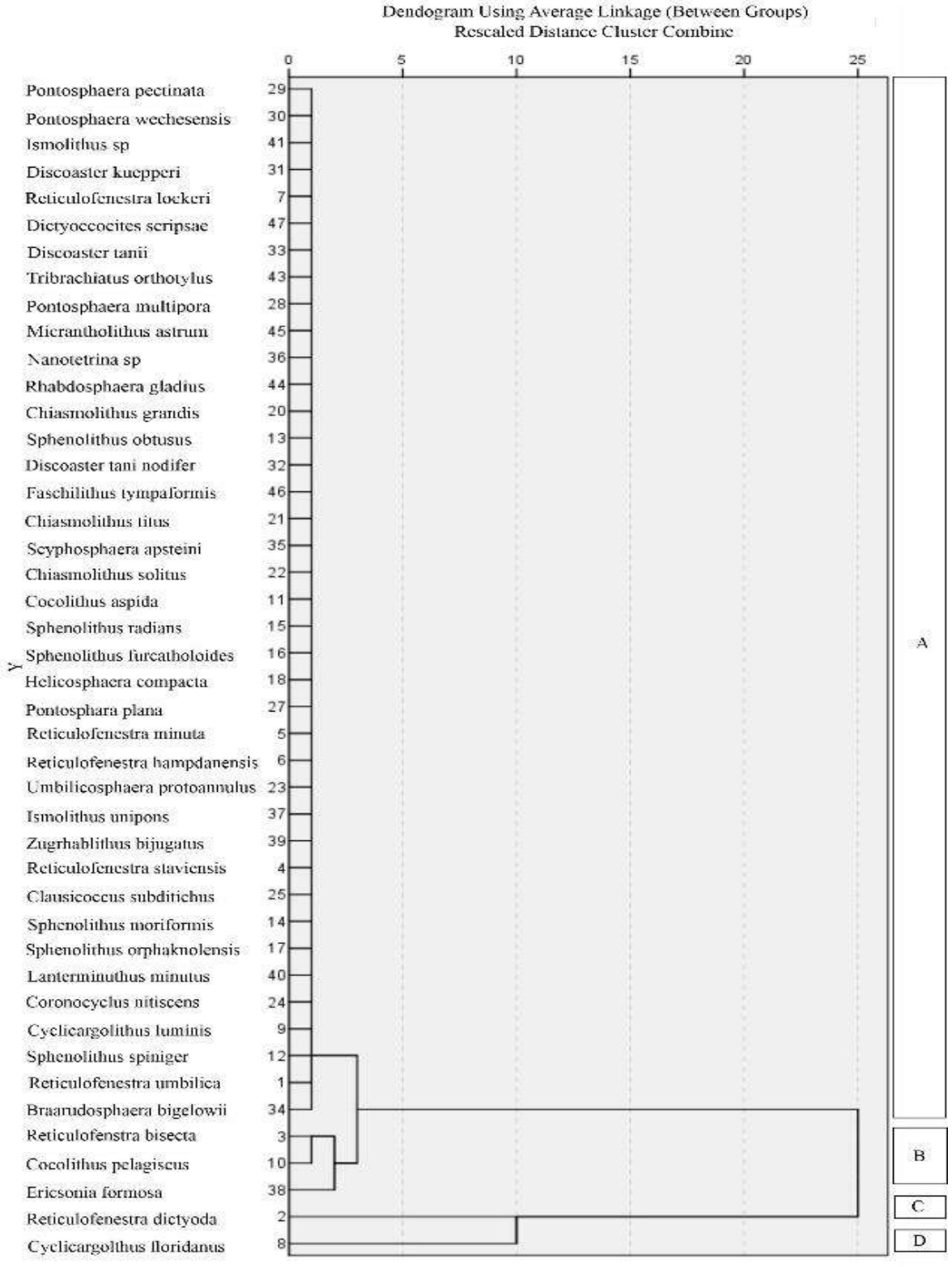

Figure 10. R-mode cluster analysis on three sections of the Elat Formation grouping into four clusters based on nannofossil associations (A, B, C, and D).

Cluster B represents the association *Ericsonia formosa, Reticulofenestra bisecta* and *Cocolithus pelagicus*. The dominant species, *Cocolithus pelagicus*, indicates cold water temperatures and represent in the upwelling zone (Kameo et al., 2020; Tangunan et al., 2018) .

Cluster C consists of a single species, which is *Reticulofenestra dictyoda.* Cluster D consists of the species *Cyclicargolithus floridanus* which characterize a high level of productivity (Monechi et al., 2000).

b. Q-mode

In this cluster analysis a similarity matrix is obtained based on the relative abundance of species from each sample. It has produced five clusters (1, 2, 3, 4, and 5) each of which represents the same environmental conditions (Figure 11).

Cluster 1 consists of all calcarenite samples from S-1 (sample codes H1 – H5) and S-2 (sample codes: N1 – N10), also five dominated calcarenite samples (MH6, MH8, MH10, MH12 and MHL12) from S-3. This cluster is characterized by the lowest abundance and diversity (abundance N= 70 to 120, average abundance Ń =91.9, and diversity index H' =2.88). This cluster has Poor (15%)-Good(40%) preservation with fair(45%) dominant.

Cluster 2 includes 11 calcarenite samples (MH2, MH3, MH4, MH5, MH7, MH9, MH11, MH13, MH14, MH15, and MH16), and 9 clay samples of clay (MHL3, MHL4, MHL6, MHL9, MHL10, MHL11, MHL14, MHL15, and MHL16) from Section-3 (N = 130-160, Ń = 144.4, and H' = 3.36). The clusters were poor (10,52%) - good (36,8%) preservation with a dominant fair preservation (52,6%) sample.

Cluster 3 is represented in one clay sample (MHL8) from Section-3 characterized by the highest abundance and diversity (N = 171, and H'=3.3). The cluster has a fair preservation and represented by this single sample are difficult to interpret.

Cluster 4 is represented by two clay samples, MHL2 and MHL7, from Section-3 which contain high abundance of nannofossil (N = 155-168, Ń = 161.5, and H ' = 2.5). The Clusters were good (50%) and fair (50%) preservation.

Cluster 5 includes two clay samples, MHL5 and MHL13, from Section-3 which contain high relative abundance (N=150-167, Ń= 158.5 and H ' =2.27). Cluster 5 were good (50%) and fair (50%) preservation

Large foraminifera assemblages

Large foraminifera identified from the limestone samples are genera *Amphistegina, Baculogypsina, Cycloclypeus, Heterostegina, Lacazinella Nummulites, Operculina, Pellatispira, Planobulinella* and *Textularia*. The observation showed the similarity of the large foraminifera assemblages at Sections-1, 2 and 3. Based on the assemblages, these lithological successions are formed at fore reef setting in neritic bathymetric zone (less than 200 meters depth).

Depositional Environment Dynamics

Stratigraphic reconstruction and biostratigraphy analysis show that the oldest rock succession from the Elat Formation is occupied by S-3 (aged NP16 to NP17), S-2 (aged NP17) in the middle, and the youngest is S-1 (aged NP17) (Table 5).

Nannofossil associated are dominated by placolith-bearing species, genus Discoaster, and *Braarudosphaera* that characterizes tropical warm-neritic (Newsam et al., 2017) taxa (Cluster A). Few cooler typical taxa were found in some samples (Cluster B).

Field observations recorded the coarsening and thickening upward of the lithological

succession in the study area. Clay and alternating clay – calcarenite at the lower part (S-3) gradually changes to massive calcarenite at the upper part (S-1).

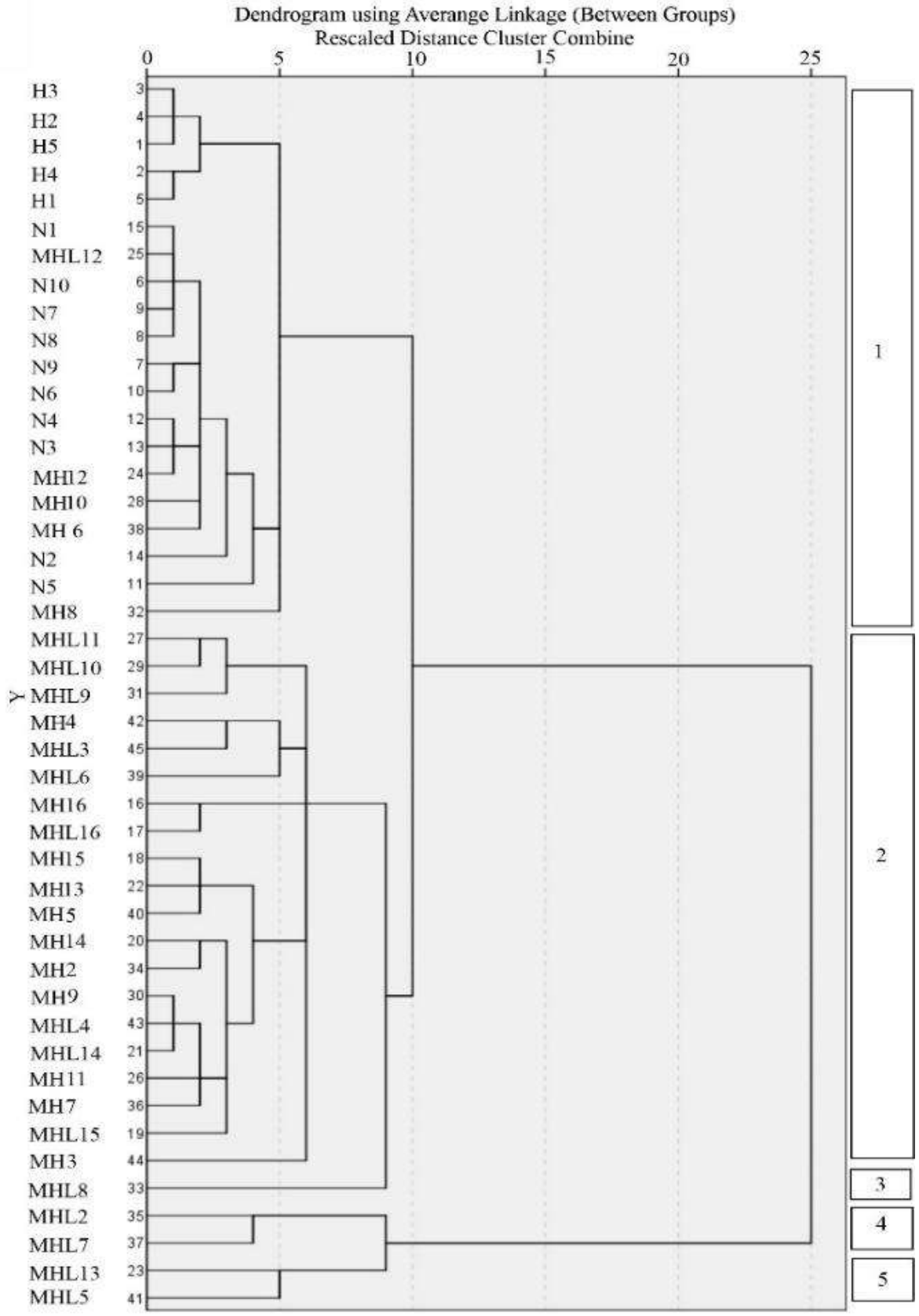

Figure 11. *Q-mode clusters* analysis on the three sections of the Elat Formation grouping into five clusters (1, 2, 3, 4, and 5) based on abundance.

Table 5. Depositional dynamics interpretation based on the assemblages of nannofossil recorded in the succession of the Elat Formation.

Section	Epoch	Age Zone	Code	Lithology	N	H'	C1	C2	C3	C4	C5
			H5	Calcarenite	81	2.87					
			H4	Calcarenite	81	2.69					
S-1			H3	Calcarenite	77	2.84					
Hollat			H2	Calcarenite	76	2.80					
			H1	Calcarenite	73	2.25					
			N10	Calcarenite	70	2.54					
		NP17	N9	Calcarenite	98	2.92					
			N8	Calcarenite	103	3.32					
			N7	Calcarenite	87	3.11					
S-2			N6	Calcarenite	103	2.92					
Ngurdu			N5	Calcarenite	108	2.98					
			N4	Calcarenite	107	3.40					
			N3	Calcarenite	102	2.98					
			N2	Calcarenite	81	2.38					
			N1	Calcarenite	100	3.29					
			MH16	Calcarenite	152	3.80					
			MHL16	Clay	153	3.39					
			MH15	Calcarenite	150	3.56					
	Middle		MHL15	Clay	161	4.33					
	Eocene		MH14	Calcarenite	128	3.60					
			MHL14	Clay	130	2.69					
			MH13	Calcarenite	143	3.29					
			MHL13	Clay	167	2.99					
			MH12	Calcarenite	88	2.61					
			MHL12	Clay	89	3.06					
			MH11	Calcarenite	129	3.34					
			MHL11	Clay	160	3.84					
			MH10	Calcarenite	94	2.60					
			MHL10	Clay	159	3.81					
S-3			MH9	Calcarenite	121	2.89					
Mata			MHL9	Clay	4.04	170					
Hollat			MH8	Calcarenite	3.32	120					
			MHL8	Clay	3.54	171					
			MH2	Calcarenite	2.31	80					
			MHL2	Clay	2.40	155					
			MH7	Calcarenite	2.80	114					
			MHL7	Clay	2.64	168					
			MH6	Calcarenite	99	2.84					
		NP16	MHL6	Clay	160	3.20					
			MH5	Calcarenite	120	2.15					
			MHL5	Clay	150	1.56					
			MH4	Calcarenite	134	3.39					
			MHL4	Clay	117	2.77					
			MH3	Calcarenite	150	3.40					
			MHL3	Clay	155	3.50					

The high abundance and diversity of nannofossil assemblages (Cluster 4 and 5) were shown at the lower part (S-3), while the lowest abundance and diversity (Cluster 1) at the upper part of the succession (S-1).

The abundance and diversity of nannofossils increases with increasing depth Changes in the composition of the nannofossil assemblages are consistent with changes in sediment grain size and lamination thickness indicating the dynamics of the depositional.

The presence of *Braarudosphaera* and *Reticulofenestra minuta* which are abundant in the middle to the upper part of the succession (on S-1 and -2) supports the

interpretation that these rocks were formed in the neritic bathymetry zone. At the lower part (S-3) these taxa less indicate a deeper environment.

Observable depositional environment dynamics shallowing upward as recorded in field observations, supported by laboratory nannofossil assemblages, relevant to previous researchers (Achdan & Turkandi, 1994; Kurniasih et al., 2019) .

The similarity of the large foraminifera assemblages in all samples indicates that there was no significant bathymetric zone change during the Middle Eocene where lithological succession was formed. The dynamics of deposition occur in an inner neritic zone which tends to be shallower.

The presence of *reworked fossils* (*Blackites inflata, Cyclicargolithus luminis, Isthmolithus unipons, Nanotrina* sp., *Sphenolithus orphaknolensis, S. spiniger*, and *Tribrachiatus orthostylus*) which is dominant in S-3 can be interpreted due to turbid currents in the slope area that occurred at the beginning of the deposition of the Elat Formation. Field observations found local slump structures that support this interpretation.

Conclusion

The Elat Formation comprises fine-grained carbonate rocks containing abundant to very-very abundant nannofossils. A total of 47 species could be identified in the 45 selected samples from three sections (S-1 – Hollat, S-2 – Ngurdu and S-3 – Mata Hollat).

The succession of Elat Formation in study area was formed in NP16 to N17 or Middle Eocene. Reconstruction of lithostratigraphy and biostratigraphic analysis shows that the oldest rock succession from the Elat Formation is occupied by S-3 (aged NP16 to NP17), in the middle is occupied by S-2 (NP17), and the youngest is S-1 (NP17).

R-mode cluster analysis of samples grouped the nanofossil assemblages that appeared coexist into four clusters (A, B, C and D). *Q-mode* cluster analysis grouping into 5 clusters (1, 2, 3, 4, and 5) based on abundance and diversity which characterizes formation under the same environmental conditions.

Sediment grain size coarsening and lamination thickening are recorded in 3 sections. Changes in the composition of the nannofossil assemblages are consistent with lithological succession indicating depositional dynamics.

Reworked fossils at the lowermost of the Elat Formation (S-3) suggest a mechanism of deposition by turbidite currents.

Acknowledgements

Authors thank to Padjadjaran University for facilities support, and the Community of Kei Island for helping during field observation.

Author Contribution

Field observations were carried out by Ratumanan. Laboratory analysis was performed by Ratumanan and Isnaniawardhani. All authors discussed, interpreted, and wrote the manuscript.

Conflict of Interest

All authors have no any financial and personal relationships with other Community or organizations that could inappropriately influence (bias) our work.

References

Achdan, A., & Turkandi, T. (1994). *Peta Geologi Lembar Kai dan Tayandu, Maluku, Skala 1:250.000*. Pusat Penelitian dan Pengembangan

Geologi, Bandung.

Agnini C., Fornaciari E., Raffi, I., Catanzariti, R., Pälike, H., Backman, J., & Rio, D. (2014). Biozonation and biochronology of Paleogene calcareous nannofossils from low and middle latitudes. *Newsletter on Stratigrafi*, 47(2), 131–181. https://doi.org/10.1127/0078-0421/2014/0042

Agnini, C., Monechi, S., & Raffi, I. (2017). Calcareous nannofossil biostratigraphy: historical background and application in Cenozoic chronostratigraphy. *Lethaia*, 50(3), 447–463. https://doi.org/10.1111/let.12218

Aizawa, C., Oba, T., & Okada, H. (2004). Late Quaternary paleoceanography deduced from coccolith assemblages in a piston core recovered off the central Japan coast. *Marine Micropaleontology*, 52(1–4), 277–297. https://doi.org/10.1016/j.marmicro.2004.05.005

Alves, T. D., Cooper, M. K. E., & Rios-Netto, A. de M. (2016). Paleogene-Neogene calcareous nannofossil biostratigraphy and paleoecological inferences from northern Campos Basin, Brazil (well Campos-01). *Journal of South American Earth Sciences*, 71, 143–160. https://doi.org/10.1016/j.jsames.2016.06.010

Auer, G., Piller, W. E., & Harzhauser, M. (2014). High-resolution calcareous nannoplankton palaeoecology as a proxy for small-scale environmental changes in the Early Miocene. *Marine Micropaleontology*, 111, 53–65. https://doi.org/10.1016/j.marmicro.2014.06.005

Bordiga, M., Henderiks, J., Tori, F., Monechi, S., Fenero, R., Legarda-Lisarri, A., & Thomas, E. (2015). Microfossil evidence for trophic changes during the Eocene-Oligocene transition in the South Atlantic (ODP Site 1263, Walvis Ridge). *Climate of the Past*, 11(9), 1249–1270. https://doi.org/10.5194/cp-11-1249-2015

Charlton, T. R., Kaye, S. J., Samodra, H., & Sardjono. (1991). Geology of the Kai Islands: implications for the evolution of the Aru Trough and Weber Basin, Banda Arc, Indonesia. *Marine and Petroleum Geology*, 8(1), 62–69. https://doi.org/10.1016/0264-8172(91)90045-3

Charlton, T. R. (2016). *Neogene Plate Tectonic Evolution of The Banda Arc*. *Proceedings Indonesian Petroleum Association*. https://doi.org/10.29118/ipa.0.16.21.g

Choiriah, S. U., & Maha, M. (2020). *Aplikasi Nannoplankton untuk Interpretasi Paleotemperatur di Zona Kendeng*. Deepublish.

Clark, W. B. (2018). a Quantitative Analysis of Calcareous Nannofossils Across a Late Oligocene Paleolatiude Transect of the North Atlantic Ocean. *GSA Annual Meeting in Indianapolis, Indiana, USA*. https://doi.org/10.1130/abs/2018am-318571

Farida, M., Jaya, A., & Sato, T. (2019). Calcareous Nannofossil Assemblages of Tonasa Formation Palakka Area, South Sulawesi: Implication of Paleoenvironmental application. *IOP Conference Series: Materials Science and Engineering*, 619(1), 012016. https://doi.org/10.1088/1757-899X/619/1/012016

Fioroni, C., Villa, G., Persico, D., & Jovane, L. (2015). Middle Eocene-Lower Oligocene calcareous nannofossil biostratigraphy and paleoceanographic implications from Site 711 (equatorial Indian Ocean). *Marine Micropaleontology*, 118, 50–62. https://doi.org/10.1016/j.marmicro.2015.06.001

Gibbs, S. J., Bown, P. R., Ridgwell, A., Young, J. R., Poulton, A. J. & O'Dea,

S. A. (2016). Ocean warming not acidification controls coccolithophore response during past greenhouse climate change. *Geology*, 44(1), 59–62. https://doi.org/10.1130/G37273.1

Gibbs, S. J., Poulton, A. J., Bown, P. R., Daniels, C. J., Hopkins, J., Young, J. R., Jones, H. L., Thiemann, G. J., O'Dea, S. A., & Newsam, C. (2013). Species-specific growth response of coccolithophores to Palaeocene–Eocene environmental change. *Nature Geoscience*, 6, 218–222. https://doi.org/10.1038/ngeo1719

Hairul, N. S. (2022). *Biostratigrafi Formasi Tonasa Berdasarkan Nannofosil Daerah Mallasoro Kecamatan Bangkala Kabupaten Jenepont Provinsi Sulawesi Selatan*. Universitas Hasanuddin.

Ikhwana, N., Farida M., & Umar H. (2022). Paleoenvironment Analysis of the Tonasa Formation based on Nannofossils in the Barru River , South Sulawesi Province. *Proceedings PIT IAGI 51st*.

Imai, R., Sato, T., & Iryu, Y. (2013). Chronological and paleoceanographic constraints Miocene to Pliocene 'mud sea' in the Ryukyu Islands (southwestern Japan) based on calcareous nannofossil assemblages. *Island Arc*, 22(4), 522–537. https://doi.org/10.1111/iar.12046.

Isnaniawardhani V. (2015). *Biostratigraphy: Basics and Biostratigraphic Zones*. Universitas Padjadjaran, Penerbit Pustaka Reka Cipta.

Isnaniawardhani, V. (2017). *Prinsip dan Aplikasi Biostratigrafi*. UNPAD PRESS.

Isnaniawardhani, V., Rivaldy, M., Ismawan., Sophian, R. I., & Andyastiya, A. S. (2020). The Miocene (25.2 - 5.6 million years ago) climate changes recorded by foraminifera and nannofossils assemblages in Bogor Basin, Western Java. *IOP Conference Series: Earth and Environmental Science*, *575*(1), 012222. https://doi.org/10.1088/1755-1315/575/1/012222

Kameo, K., Kubota, Y., Haneda, Y., Suganuma, Y., & Okada, M. (2020). *Calcareous nannofossil biostratigraphy of the Lower–Middle Pleistocene boundary of the GSSP, Chiba composite section in the Kokumoto Formation, Kazusa Group, central Japan, and implications for seasurface environmental changes, Progress in Earth and Planetary Science*, 7, 36. https://doi.org/10.1186/s40645-020-00355-x

Kanungo, S., Young, J., & Skowron, G. (2017). Microfossils: Calcareous Nannoplankton (Nannofossils). In Sorkhabi, R., *Encyclopedia of Petroleum Geoscience*. Springer Link. https://doi.org/10.1007/978-3-319-02330-4

Karatsolis, B-T., & Henderiks, J. (2023). Late Neogene nannofossil assemblages as tracers of ocean circulation and paleoproductivity over the NW Australian shelf. *Climate of the Past*, 19(4), 765–786. https://doi.org/10.5194/cp-19-765-2023

Kasem, A. M., Faris, M., Jovane, L., Ads, T. A., Frontalini, F., & Zaky, A. S. (2022). Biostratigraphy and Paleoenvironmental Reconstruction at the Gebel Nezzazat (Central Sinai, Egypt): A Paleocene Record for the Southern Tethys. *Geosciences (Switzerland)*, 12(2), 96. https://doi.org/10.3390/geosciences12020096

Khorassani, M. P. K., & Hadavi, F., Ghasemi-Nejad, E., & Mousavi-Harami, R. (2014). Biostratigraphy and Paleoecological Study of Pabdeh Formation in Interior Fars, Zagros Basin, Iran. *Open Journal of Geology*, 4(11), 571–581.

https://doi.org/10.4236/ojg.2014.411042

Kontakiotis, G., Antonarakou, A., & Zachariasse, W. J. (2013). Late Quaternary palaeoenvironmental changes in the Aegean Sea: interrelations and interactions between North and South Aegean Sea. *Bulletin of the Geological Society of Greece*, 47(1), 167–177. https://doi.org/10.12681/bgsg.10920

Kurniasih, A., Qadaryati, N., & Setyawan, R. (2019). Surface geological investigation as the initial stage of hydrocarbon exploration in Kei Besar Island, Southern Maluku. *IOP Conference Series: Earth and Environmental Science*, 279(1), 012018. https://doi.org/10.1088/1755-1315/279/1/012018

Ladner, B. C. (2007). Data Report: Calcareous Albian, Nannofossil biostratigraphy of sediments recovered at site 1276, Ocean Drilling Program leg 210. In. Tucholke, B.E. Sibuet, J.-C., and Klaus, A. (Eds.). *Proc. ODP, Sci. Results, 210: College Station, TX (Ocean Drilling Program), 1–9.* http://www-odp.tamu.edu/publications/210_SR/113/113.htm

Lowery, C. M., Corbett, M. J., Leckie, R. M., Watkins, D., Miceli, R., & A., Pramudito, A. (2014). Foraminiferal and nannofossil paleoecology and paleoceanography of the Cenomanian-Turonian Eagle Ford Shale of southern Texas. *Palaeogeography, Palaeoclimatology, Palaeoecology*, *413*, 49–65. https://doi.org/10.1016/j.palaeo.2014.07.025

Martini, E. (1971). Standard Tertiary and Quaternary Calcareous Nannoplankton Zonation. *Proceeding of 2nd Conference Planktonic Microfossils, Rome (1970)*, 739–785.

Mandur, M. M. M., Hewaidy, A. G. A., Farouk, S., & El Agroudy, I. S. (2022). Implications of calcareous nannofossil biostratigraphy, biochronology, paleoecology, and sequence stratigraphy of the Paleocene-Eocene of the Wadi Qena, Egypt. *Journal of African Earth Sciences*, 193, 104594. https://doi.org/https://doi.org/10.1016/j.jafrearsci.2022.104594

Monechi, S., Buccianti, A., & Gardin, S. (2000). Biotic signals from nannoflora across the iridium anomaly in the upper Eocene of the Massignano section: Evidence from statistical analysis. *Marine Micropaleontology*, 39(1–4), 219–237. https://doi.org/10.1016/S0377-8398(00)00022-0

Faris, M., Farouk, S., & Shabaan, M. (2021). An overview of the Paleocene-Eocene calcareous nannofossil biostratigraphy and bioevents in Egypt. *Stratigraphy & Timescales*, 6, 225–292. https://doi.org/10.1016/bs.sats.2021.09.003

Nannotax3. (2014). *Nannotax 3*. https://www.mikrotax.org/Nannotax3/

Newsam, C., Bown, P. R., Wade, B. S., & Jones, H. L. (2017). Muted calcareous nannoplankton response at the Middle/Late eocene turnover event in the western North Atlantic Ocean. *Newsletters on Stratigraphy*, 50(3), 297–309. https://doi.org/10.1127/nos/2016/0306

Okada, H., & Bukry, D. (1980). Supplementary modification and introduction of code numbers to the low-latitude coccolith biostratigraphic zonation (Bukry, 1973; 1975). *Marine Micropaleontology*, 5, 321–325. https://doi.org/10.1016/0377-8398(80)90016-X

Okada, H. (2000). Neogene and Quaternary calcareous nannofossils from the Blake Ridge, Sites 994, 995, and 997. *Proceedings of the Ocean Drilling Program, Scientific Results*, 164, 331–341.

Perch-Nielsen, K. (1985). Cenozoic

Calcareous Nannofossils. in Bolli, H. M., Saunders, J. B., and Perch-Nielsen, K. (Eds.), *Plankton Stratigraphy*. Cambridge University Press, 427–554.

Pratiwi, S. D., & Sato, T. (2016). Reconstruction of Paleoceanography Significance in the Western Pacific and Atlantic Oceans during the Neogene Based on Calcareous Nannofossil Productivity and Size Variations, Related to the Global Tectonic Events. *Open Journal of Geology*, *06*(08), 931–943. https://doi.org/10.4236/ojg.2016.68070

Raffi, I., Agnini, C., Backman J., Catanzariti, R., & Pälike, H. (2016). Cenozoic calcareous nannofossil biozonation from low and middle latitudes: A synthesis. *Journal of Nannoplankton Research*, *36*(2), 121–32. https://doi.org/10.58998/jnr2206

Raffi, I., & Backman, J. (2022). The role of calcareous nannofossils in building age models for Cenozoic marine sediments : a review. *Rendiconti Lincei. Scienze Fisiche e Naturali*, *33*(1), 25–38. https://doi.org/10.1007/s12210-022-01048-x

Ratumanan, R. C. F., Isnaniawardhani, V., & Muljana, B. (2022). Nannofossil Biostratigraphy of Elat Formation, Kei Besar Island, Southeast Maluku. *IOP Conference Series: Earth and Environmental Science*., 1148(1), 012027. https://doi.org/10.1088/1755-1315/1148/1/012027

Rosmadi, N. S., Sulaiman, N., Sulaiman, N., & Asis, J. (2022). Biostratigraphy and paleodepositional environment of the Temburong Formation at Batu Luang, Klias Peninsula, Sabah based on calcareous nannofossil. *Journal of Tropical Resources and Sustainable Science*, *10*(1), 20–27. https://doi.org/10.47253/jtrss.v10i1.894

D'Onofrio, R., Zaky, A. S., Frontalini, F., Luciani, V., Catanzariti, R., Francescangeli, F., Giorgino, M., Coccioni, R., Özcan, E., & Jovane, L. (2021). Impact of the Middle Eocene Climatic Optimum (MECO) on Foraminiferal and Calcareous Nannofossil Assemblages in the Neo-Tethyan Baskil Section (Eastern Turkey): Paleoenvironmental and Paleoclimatic Reconstructions. *Applied Sciences*, 11(23), 11339. https://doi.org/10.3390/app112311339

Roth, P. H. (1984). Preservation of Calcareous Nannofossils and Fine-Grained Carbonate Particles in Mid-Cretaceous Sediments from the Southern Angola Basin, Site 530. *Deep Sea Drilling Project Reports and Publications*, 75, 651–655. https://doi.org/10.2973/dsdp.proc.75.112.1984

Schneider, L. J., Bralower, T. J., Kump, L. R., & Patzkowsky, M. E. (2013). Calcareous nannoplankton ecology and community change across the Paleocene-Eocene Thermal Maximum. *Paleobiology*, 39(4), 628–647. https://doi.org/10.1666/12050

Senemari, S., & Jalili, F. (2021). Eocene to Oligocene nannofossils stratigraphy and environmental conditions in Izeh Province, Zagros Basin, East Tethys. *Journal of Palaeogeography*, 10(10), 1–13. https://doi.org/10.1186/s42501-021-00092-2

Senemari, S., & Mejía-Molina, A. (2022). Calcareous nannofossil biostratigraphy and paleoenvironment of the Eocene–Oligocene interval in the Pabdeh Formation in southwestern Iran. *International Journal of Earth Sciences*, 111(4), 1289–1305. https://doi.org/10.1007/s00531-022-02180-7

Shepherd, C. L., Kulhanek, D. K., Hollis, C. J., Morgans, H. E. G., Strong, C. P., Pascher, K. M., & Zachos, J. C. (2021). Calcareous nannoplankton response to early Eocene warmth, Southwest

Pacific Ocean. *Marine Micropaleontology*, 165, 101992. https://doi.org/10.1016/j.marmicro.2021.101992

Sheward, R. M, Poulton, A. J., Gibbs, S. J., Daniels, C. J., & Bown, P. R. (2017). Physiology regulates the relationship between coccosphere geometry and growth phase in coccolithophores. *Biogeosciences*, 14, 1493–1509. https://doi.org/doi:10.5194/bg-14-1493-2017

Suchéras-Marx, B., Giraud, F., Lena, A., & Simionovici, A. (2016). Picking nannofossils: How and why. *Journal of Micropalaeontology*, 36, 219–221. https://doi.org/10.1144/10.1144jmpaleo2016-013

Tangunan, D. N., Baumann, K.-H., Just, J., LeVay, L. J., Barker, S., Brentegani, L., De Vleeschouwer, D., Hall, I. R., Hemming, S., Norris, R., & the Expedition 361 Shipboard Scientific Party. (2018). The last 1 million years of the extinct genus Discoaster: Plio-Pleistocene environment and productivity at Site U1476 (Mozambique Channel). *Palaeogeography. Palaeoclimatologu. Palaeoecology*, 505, 187–197. https://doi.org/10.1016/j.palaeo.2018.05.043

Toffanin, F., Agnini, C., Rio, D., Acton, G., & Westerhold, T. (2013). Middle Eocene to early Oligocene calcareous nannofossil biostratigraphy at IODP Site U1333 (equatorial Pacific). *Micropaleontology*, 59(1), 69–82. http://www.jstor.org/stable/24413317

Umoh, E. E. (2023). Palaeoecological Aspects of Nannoplankton Assemblages of AS-2 Well, Niger Delta. *Ajayi Crowther Journal of Pure and Applied Sciences*, 2(2). https://doi.org/10.556534/acjpas.2023.02.02.107

Villa, G., Florindo, F., Persico, D., Lurcock, P., de Martini, A. P., Jovane, L., & Fioroni, C. (2021). Integrated calcareous nannofossil and magnetostratigraphic record of ODP Site 709: Middle Eocene to late Oligocene paleoclimate and paleoceanography of the Equatorial Indian Ocean. *Marine Micropaleontology*, 169, 102051. https://doi.org/10.1016/j.marmicro.2021.102051

Widhiyatmoko, M., Isnaniawardhani, V., & Zajuli, M. H. H. (2023). Distribusi Nannofosil dan Foraminifera pada Batas Pliosen-Plistosen Formasi Batilembuti di Pulau Yamdena, Provinsi Maluku dan Relevansinya dengan Tektonik Regional. *Jurnal Geologi Dan Sumberdaya Mineral*, 24(1), 39–50. https://doi.org/10.33332/jgsm.geologi.v24i1.737

Young, J. R. (1998). *Calcareous Nannofosil Biostratigraphy* (P. R. Bown (ed.)). British Micropalaeontological Society Publications Series. Chapman & Hall. https://zarmesh.com/wp-content/uploads/2021/11/Calcareous-Nannofossil-Biostratigraphy.pdf

ISSN: 2579-5821 (Print)
ISSN: 2579-5546 (Online)
URL address: http://journal.unhas.ac.id/index.php/geocelebes
DOI: 10.20956/geocelebes.v7i2.20603

Jurnal Geocelebes Vol. 7 No. 2, October 2023, 154 – 167

Analysis of Unconventional Oil and Gas Reservoirs using Well Logging, Geochemical and Seismic Data

Rahmat Catur Wibowo*, Aryka Claudia Eka Putri, Ordas Dewanto

Geophysical Engineering, Faculty of Engineering, Lampung University, Indonesia.

*Corresponding author. Email: rahmat.caturwibowo@eng.unila.ac.id

Manuscript received: 4 April 2022; Received in revised form: 5 October 2022; Accepted: 10 August 2023

Abstract

Since conventional oil and gas is under a depletion phase, unconventional oil, and gas have become prime candidates for current and future oil and gas production. Based on this, investment and research have increased significantly related to unconventional oil and gas exploitation, especially in the North East Java Basin, one of the sedimentary basins producing oil and gas. The research was conducted in the form of well-logging, geochemical, and seismic data analysis to determine the quality and quantity of oil and gas reservoirs. The thickness and TOC value of the reservoir were determined using well-logging data using the Passey method, resulting in a thickness ranging from 900-954 ft and an average TOC value of 3.87 Wt% in the Kujung III Formation. Based on geochemical data analysis, the reservoir has type II kerogen with an immature-early mature maturity level (Ro and Tmax). Meanwhile, based on seismic data, the reservoir thickens to the northwest, ranging from 500-600 m. Unconventional oil and gas reservoirs in the research area have the potential to be developed because they meet several criteria, such as being rich in organic material and thick, even though the maturity level is still in the immature phase. It is estimated that deeper areas will produce different levels of maturity as pressure and temperature increase.

Keywords: geochemistry; reservoir; seismic; unconventional oil and gas; well logging.

Citation: Wibowo, R. C., Putri, A. C. E., and Dewanto, O. (2023). Analysis of Unconventional Oil and Gas Reservoirs using Well Logging, Geochemical and Seismic Data. *Jurnal Geocelebes*, 7(2), 154-167, doi: 10.20956/geocelebes.v7i2.20603

Introduction

The North East Java Basin is one of the oil and gas basins that have the potential to produce oil and gas, marked by a new well owned by a subsidiary of PT. Pertamina Hulu Energi Tuban East Java is capable of producing 531 BPOD of oil (Suharyati et al., 2019). In addition, according to Mudjiono & Pireno (2002), the North East Java Sea Basin has petroleum systems such as source rocks, reservoirs, and cap rocks that are scattered in various formations. The Lower "OK" Member, Kujung Unit II Formation, and Ngimbang Formation have the potential to be good source rocks with Total Organic Carbon (TOC) values of more than 1%. The Lower "OK" Member shale has the potential to be a good source rock. The Kujung Formation Unit I is equivalent to the Prupuh deep-sea limestone in the East Java or Madura Basin. This unit has the best reservoir characteristics in the North East Java Sea Basin. The main cap rocks in the North East Java Sea Basin are the thick shale facies of the Kujung Formation Unit II (for the Ngimbang Formation reservoir) and the shale in the Rancak Unit (for the Kujung Formation Unit II reservoir). These shales are generally deposited on top of the Kujung Unit I Formation's reefs and effectively cover the trapped hydrocarbons (Satyana & Purwaningsih, 2003).

Source rocks are sedimentary rocks that contain fine-grained organic material such

as clay or shale and have the potential to produce and become oil and gas reservoirs (Muther et al., 2021). In conducting unconventional oil and gas exploration, several methods can be used, such as the well-logging method (Szabó et al., 2021), seismic method (Harilal & Tandon, 2012), and geochemical analysis (Setyawan et al., 2020). The well-logging method is one of the methods used to obtain subsurface physical information by drilling directly (Fatahillah et al., 2017). The data obtained by using the well-logging method has a depth domain. The seismic method is a method used to obtain subsurface information laterally by utilizing a seismic wave propagation system. Data obtained from measurements using the seismic method has a time domain. These two data are equalized in the domain so that further processing can be carried out so as to explain the subsurface conditions vertically and laterally (Field et al., 2015). The geochemical analysis uses chemical principles to explain the quality of the source rock through kerogen type and maturity level of the source rock (El-Khadragy et al., 2018).

This study aims to determine the kerogen type and maturity level of the reservoir, the TOC value, and the unconventional oil and gas reservoir zone based on seismic data in Field "X", North East Java Basin.

The Jendral Sudirman Road, Muara Bulian, Batang Hari crosses 2 formations, which are the alluvial formation (Qa), and the kasai formation (QTk) based on the Regional Geological Map of Muara Bungo Sheet.

Physiographically, the Batang Hari area is located in the western part of the South Sumatra Basin, which is a lowland area in eastern Sumatra, bounded by the Semangko Fault and Bukit Barisan to the southwest, the Sunda Shelf to the northeast, the Lampung Plateau to the southeast separating the basin from the Sunda Basin, and the Twelve Mountains and Thirty Mountains to the northwest separating the South Sumatra Basin from the Central Sumatra Basin (Barber et al., 2005).

Well Logging Method

An unconventional oil and gas reservoir zone can be interpreted qualitatively and quantitatively using well data using GR logs, resistivity logs, and sonic logs (Sumotarto et al., 2017). Qualitatively, a log will represent a potential source rock if it has high GR, high resistivity, and high sonic values (Passey et al., 2010).

There are various methods to quantitatively analyze the organic material content of well log data. One of the most commonly used methods is using sonic and resistivity logs. The method has been widely modified and is known as "ΔLogR" by Passey et al. (1990) (Figure 1). This method can determine the TOC value by performing an empirical calculation using the following equation.

$$TOC = \Delta LogR \; x \; 10^{(0{,}297 - 0{,}1688.LOM)} \quad (1)$$

$$\Delta LogR = Log10 \left(\frac{R}{R_{baseline}}\right) + 0{,}02 \; x \; (t - t_{baseline}) \quad (2)$$

with,
TOC = *Total Organic Carbon* (wt%)
LOM = *Level of Maturity*
ΔLogR = Separation curve between resistivity and sonic log data
R= Measured resistivity value (Ωm)
$R_{Baseline}$= Resistivity value at non-source zone (Ωm)
t = Measured transit time (us/f)
$t_{Baseline}$ = Transit time at non-source zone (us/f).

Using Passey's method, LOM values can be obtained from Vitrinite Reflectance (Ro) data correlated on a graph as shown in Figure 2.

Quantitatively, a reservoir zone can be recognized through the Total Organic

Carbon (TOC) content contained therein. TOC analysis is a stage to analyze the overall organic content of a rock. The depositional environment affects the organic carbon content of a rock. The Table 1 can be used as a reference in determining the richness of the source rock (Wibowo, 2013).

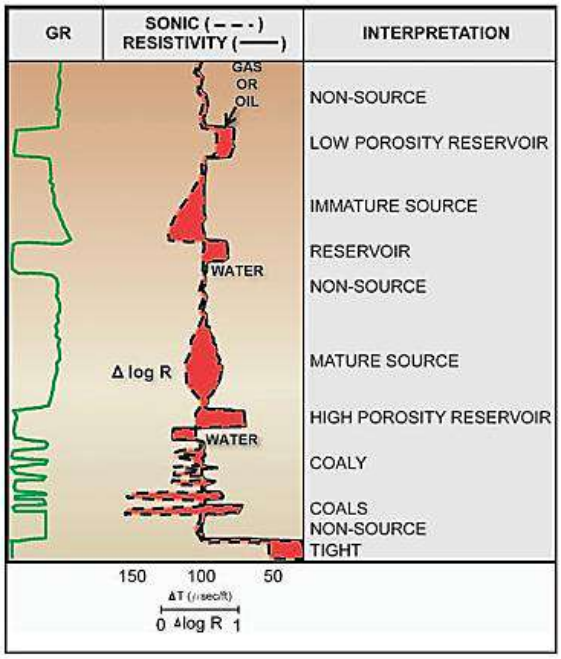

Figure 1. Response of Log Curve to Source Rock Zone (Passey et al., 2010).

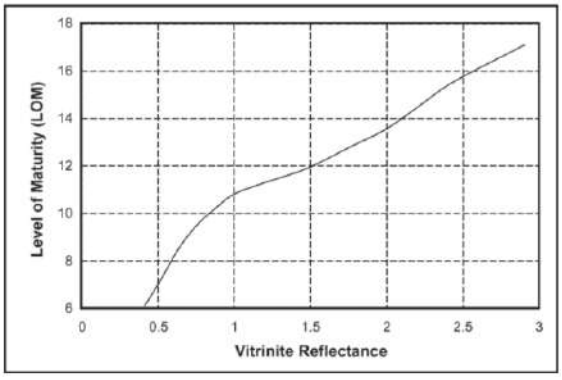

Figure 2. LOM graph from Ro data (Crain, 2000).

Table 1. TOC content of source rock quality (Peters & Cassa, 1994).

Total Organic Carbon (%)	Quality
0 – 0.5	Poor
0.5 – 1	Fair
1 – 2	Good
2 – 4	Very Good
>4	Excellent

Geochemical Analysis

Quantity and quality analysis of an unconventional oil and gas reservoir can also be known by using geochemical data (Zhao et al., 2019). The quantity of a reservoir can be known from the organic material content (TOC) as in Table 1. Meanwhile, the quality of a reservoir when viewed using geochemical data can be known through the type of organic material (Kerogen Type) and the level of maturity. Kerogen is the content of organic material in a sedimentary rock that is insoluble in organic solvents. There are four types of kerogen, which are Kerogen Type I, Kerogen Type II, and Kerogen Type III (Brooks et al., 1984; Olatunde, 2016; Scheeder et al., 2020).

Geochemical data such as Hydrogen Index (HI) and Thermal maturity level (Tmax) are used to determine the kerogen type and maturity of a reservoir. HI represents the amount of atomic hydrogen content of organic material contained in a rock (Niu et al., 2018). These hydrogen atoms are the basic elements that form hydrocarbon chains. The type of hydrocarbon formed will be influenced by the amount of hydrogen that forms hydrocarbon chain bonds. Thermal maturity based on the Tmax value indicates the maturity level of the source rock (Peters & Cassa, 1994). According to Peters & Cassa (1994), the maturity level of the source rock can be classified into immature, oil zone, and gas zone given in the van Krevelen Diagram.

Using the van Krevelen Diagram, these two data are correlated with each other to obtain information on the kerogen type and maturity level of the source rock (Song et al., 2013). According to Brooks et al. (1984), van Krevelen Diagram is a plot diagram of geochemical data such as the Hydrogen Index (HI) with Organic Index (OI) to characterize coal and qualify it (Brooks et al., 1984). This diagram was later modified to provide information on

kerogen type and thermal maturity of organic material as shown in Figure 3.

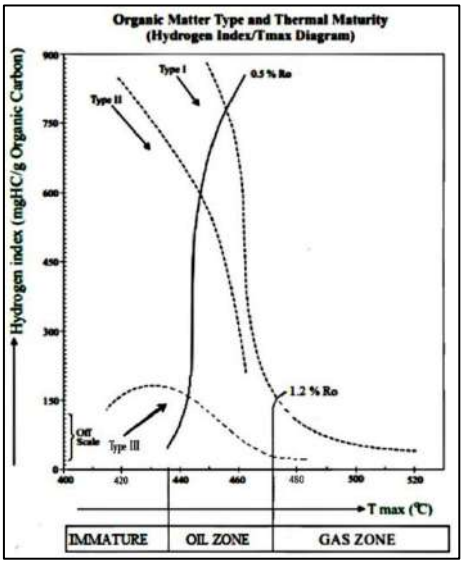

Figure 3. Modification of van Krevelen Diagram (Brooks et al., 1984).

In addition, the maturity level of a source rock can also be known from the Level of Maturity (LOM) value (Devi et al., 2017). This LOM value can be obtained from the pyrolysis stage of a rock sample. Pyrolysis is a stage to analyze the hydrocarbon component in a source rock. This pyrolysis stage is carried out by gradually heating a sample that does not contain oxygen in an inert atmosphere using a certain temperature. Pyrolysis parameters are divided into several types, which are as follows (Scheeder et al., 2020).

1. S1, is the total free hydrocarbons contained in the rock sample.
2. S2, is organic material that produces hydrocarbons through maturation and burial stages.
3. S3, is the total CO_2 produced during the pyrolysis stage. S2 is linearly related to TOC at a certain LOM of a source rock (Figure 4).

The relationship between Ro and LOM can be seen in Figure 2. A source rock can be said to be mature if it has a maturity level value or LOM between 7 - 12. If the LOM value is less than 7, then a source rock is classified as an immature source rock. If it has a LOM value of more than 12, then a source rock can be said to be past mature (Crain, 2000).

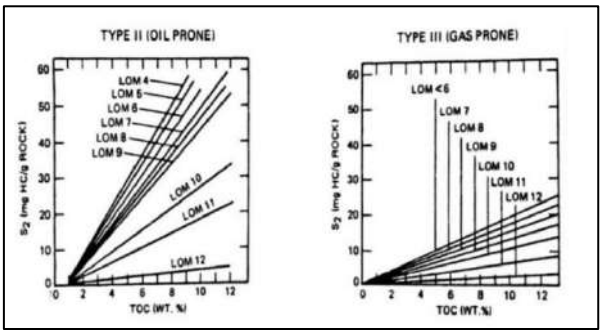

Figure 4. The relationship between S2 and TOC to determine the level of maturity (Brooks et al., 1984).

Seismic Method

The seismic method is one of the geophysical methods that can describe the subsurface of the earth laterally well (Wibowo et al., 2020).

The earth, which is the medium for wave propagation, consists of heterogeneous rock layers so that the discontinuity of the nature of this medium causes seismic waves to propagate some of their energy and will be reflected and some other energy will be forwarded to the medium below. Seismic surveys are conducted by creating vibrations using a source (Zou et al., 2018). The source will produce vibrations that will propagate in various directions under the earth's surface as a vibrating wave (Helal et al., 2015). Data recorded in the form of the travel time of reflected waves will provide information about the speed of wave propagation in a rock layer that it occupies (del Monte et al., 2018).

By using seismic data, lateral subsurface information of potential reservoir zones can be identified (Habib et al., 2016). In the petroleum system sequence, reservoirs are located below and tend to be in low areas. This can be said because a mature source rock is affected by higher temperatures and pressures (Athmer et al., 2014).

From the seismic data, a surface will be generated that is able to inform the high and low areas of the research site. A source rock tends to be in the low area (Fajana et al., 2019).

Research Method

The methods used in this research are seismic method, well-logging method, and geochemical analysis. The three methods are used to determine the qualitative and quantitative potential of unconventional oil and gas reservoirs in Field "X" of the North East Java Basin. In this study, three well data were used, which are Well S-1, Well K-1, and Well C-1. The types of logs used in this study are the Gamma-Ray (GR) log, resistivity log, and sonic log. In addition, 50 lines of post-stack 2D seismic data were used, and geochemical data on Well S-1. The geochemical data include maturity level data (Ro and Tmax) Hydrogen Index (HI), Total Organic Carbon (TOC), and S2. Then, check-shot data is used to equalize the domain between seismic data and well data.

In the first stage, this research analyzes well-logging data, for reservoir zone determination and qualitative analysis. The next stage is the geochemical analysis which aims to evaluate the potential reservoir zone qualitatively and quantitatively. The final stage is to see the distribution of reservoir potential based on seismic data.

Results and Discussion

Well Logging Analysis

In this study, qualitatively analyzed log data at Well S-1 to determine the reservoir zone in the study area. In Figure 5, there is a high GR log value and a separation between the DT log and the LLD log. So it can be said qualitatively that Well S-1 has a zone with the potential as a reservoir. If the zone indicated as a reservoir in Figure 5 is scaled up, it looks like Figure 6.

This method uses the empirical equation as in equation 1 to obtain the value of organic material content (TOC). Based on calculations using the Passey method, data were obtained as in Table 2.

Table 2. Results of TOC Value Calculation using the Passey Method.

Depth (ft)	$\Delta LogR$	TOC
5820	0.705	2.756
6000	0.358	0.669
6090	0.675	0.602
6180	0.778	0.307
6270	1.003	1.734
6360	0.551	0.201
6450	0.642	0.171
6630	0.530	1.071
6720	0.731	2.016

Based on Table 2 and Figure 5, it can be said that the organic material content of the reservoir zone in Well S-1 with a depth of 5820 - 6720 ft is quite very good (Table 1) although qualitatively based on Peters & Cassa (1994) it can be said to be immature (Tmax 361 - 437^0C). As in previous research conducted in this basin, the zone that is said to have the potential to become the source rock is around the Kujung Unit II Formation (Aprilana et al., 2018).

Table 3. Calculation Results of TOC Value of Well K-1 using Passey Method.

Depth (ft)	**ΔLogR**	TOC
5000	0.552	7.210
5109	0.303	3.964
5241	0.498	6.506
5400	0.466	6.085
5475	0.810	10.57
5540	0.268	3.504
5690	0.072	0.945
5806	0.066	0.873
5952	0.006	0.090

Based on the data from Well K-1, it can be seen that qualitatively there is a source rock zone at a depth of between 5000 ft to 6000 ft. This can be said to be so because of the presence of separations. This can be said because of the separation formed between

the sonic and resistivity log curves shown in yellow. Based on the type of log curve response (Passey et al., 2010), the shape of the separation in Well K-1 indicates that the reservoir zone is immature as shown in Figure 7.

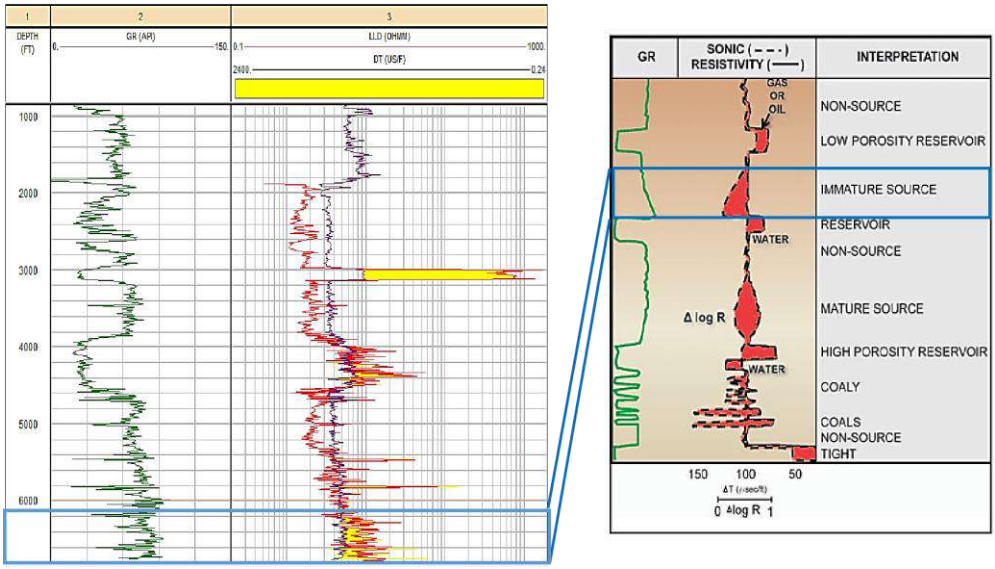

Figure 5. The Source Rock Zone of Well S-1 with yellow separation is the response curve based on Passey et al. (2010).

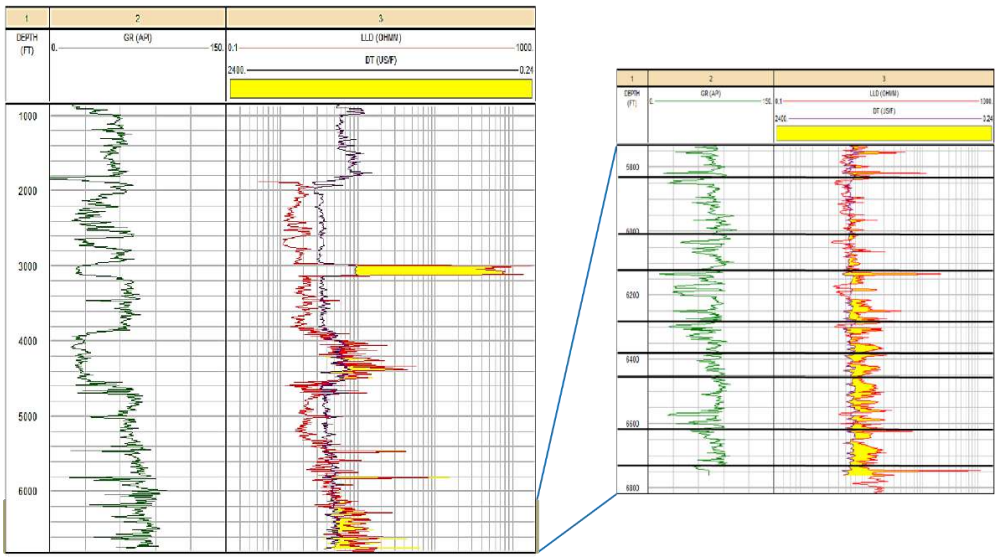

Figure 6. The TOC calculation process in Well S-1 with yellow separation is a curve response based on Passey et al. (2010).

In terms of quantity, the amount of organic material in Well K-1 was obtained using the same method as in Well S-1, which is the Passey method. Based on this calculation, the quantity of organic material in Well K-1 is obtained as shown in Table 3 and Figure 8. In Well K-1 there is a reservoir zone at a depth between 5000 - 5925 ft with reservoir quality characteristics from fair to very good and immature maturity level (Tmax 426 - 435^{0}C). The source rock zone is included in the Kujung Unit III Formation and at the beginning of the CD Formation.

Based on the high GR log curve response in Well K-1, it can be said that both formations are shale lithologic. The reservoir zone has an organic material

content (TOC) of 0.1 - 7.2 wt% as shown in Table 3.

Based on the log curve response type (Passey et al., 2010), the separation shape in Well C-1 indicates that the reservoir zone is immature as shown in Table 4 and Figure 9. The quantity of organic material in Well C-1 was obtained using the same method as in Well S-1, which using the Passey method. Therefore, several sample points were used to calculate the quantity of organic material. In Well C-1, five sample points were used as shown in Figure 10.

Table 4. Calculation Results of TOC Value of Well C-1 using Passey Method.

Depth (m)	$\Delta LogR$	TOC
1100.9	0.055	1.065
1131	0.056	1.058
1141.4	0.306	5.892
1158.1	0.121	2.330
1172.3	0.718	13.83

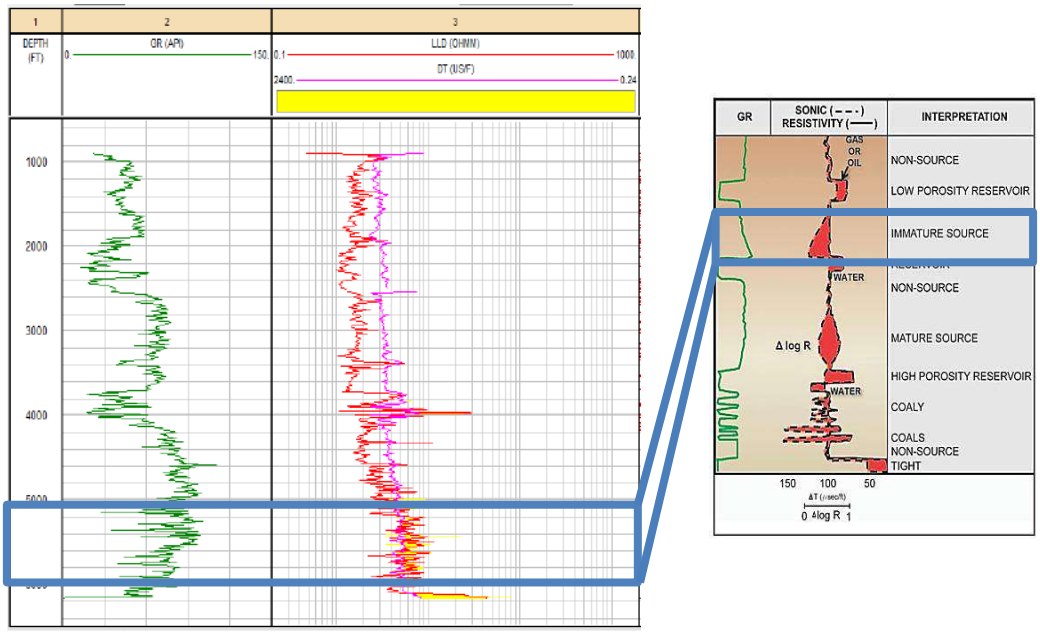

Figure 3. The Source Rock Zone in Well K-1 with yellow separation is the response curve based on Passey et al. (2010).

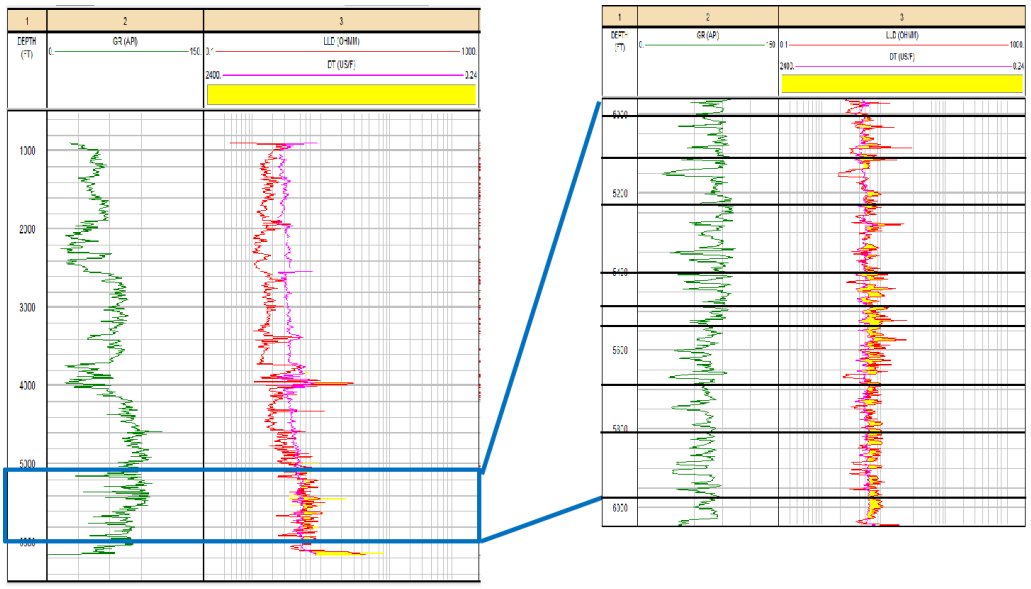

Figure 4. The TOC calculation process at Well K-1 with yellow separation is a curve response based on Passey et al. (2010).

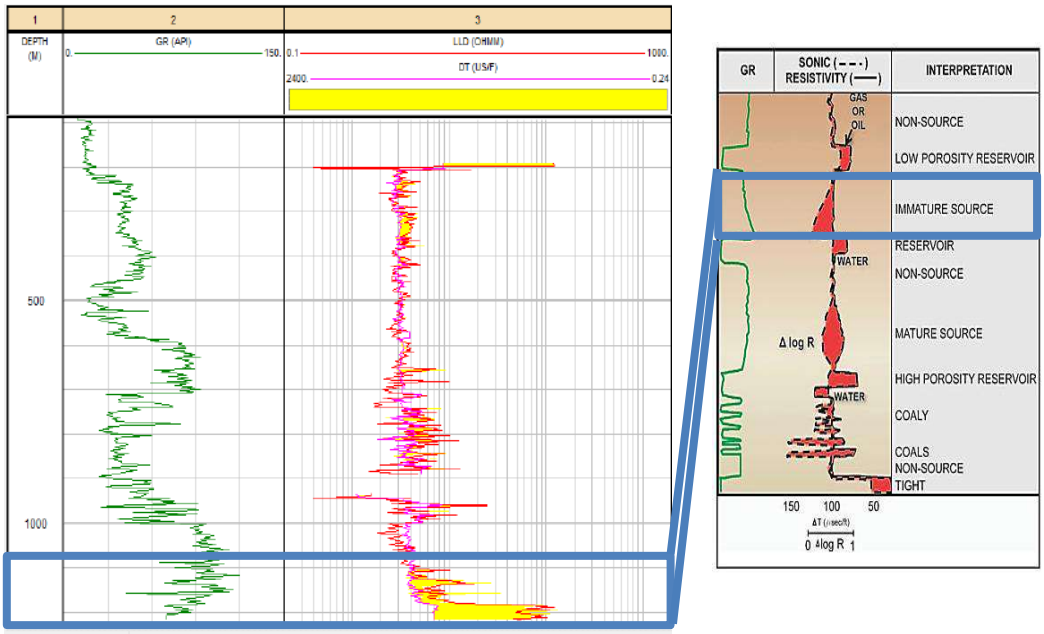

Figure 5. The reservoir zone in Well C-1 with yellow separations is the response curve based on Passey et al. (2010).

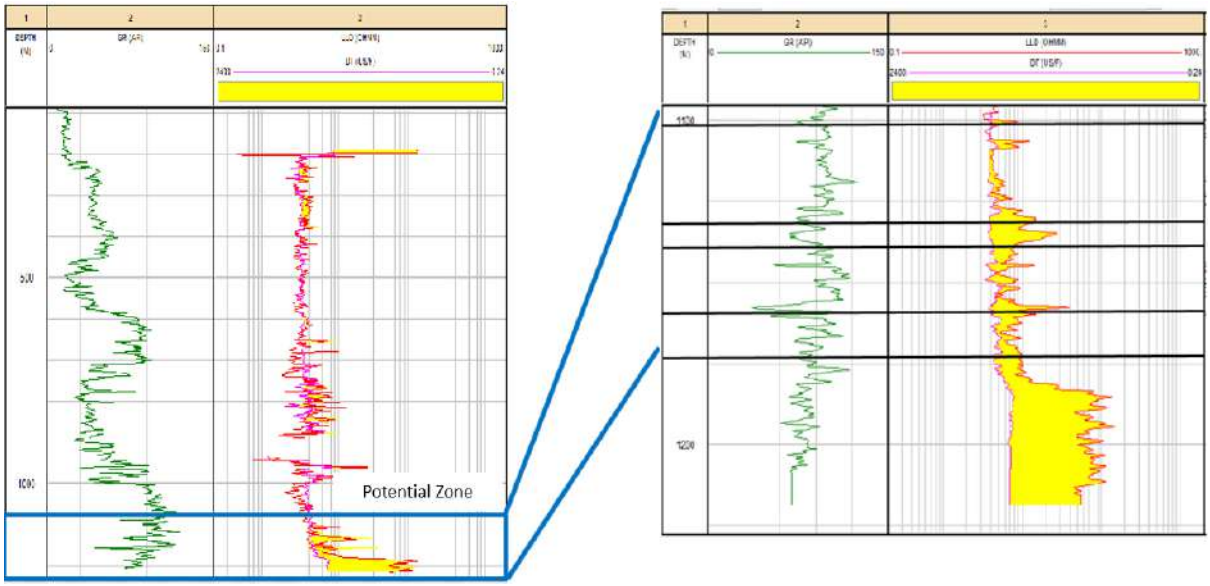

Figure 6. The TOC calculation process at Well C-1 with yellow separation is a curve response based on Passey et al. (2010).

Based on data processing carried out at Well C-1 using the Passey method, it can be said that the reservoir zone qualitatively and quantitatively based on well data is at a depth of between 1100 m to 1200 m, including the end of the Kujung Formation to the Talang Akar Formation, and is classified as an immature reservoir zone. Based on the high radioactive log curve response in Well C-1, it can be said that both formations are shale lithologic. The reservoir zones have an organic material content (TOC) of 1 - 13 wt% with good to excellent quality.

Geochemical Analysis

In general, the prediction of TOC values using the Passey et al. (1990) method produced a good correlation with R^2 0.853 (Table 5). The quality of a source rock can be assessed by the type of kerogen and the type of hydrocarbons that will be produced. Kerogen is the ability of the source rock to

produce products in the form of oil or gas. Kerogen itself has several types, which are kerogen types I, II, and III. Where each type of kerogen has a different product. One way to find out the type of kerogen from a source rock is to cross-correlate the Tmax data with the Hydrogen Index (HI) data on the van Krevelen Diagram. In Figure 11, which is a cross-correlation between HI and Tmax data in the van Krevelen Diagram, it can be indicated that the source rock in Well S-1 has immature type II kerogen (Figure 11). According to Muther et al. (2021), source rocks with kerogen type II have the potential to produce oil and gas products. Kerogen type II is a type of kerogen that is formed from several sources, such as marine algae, spores, and pollen, the waxy layer of a plant, plant fats, and fossil resins.

Table 5. Correlation results between TOC value calculation using Passey Method and TOC core.

Depth (ft)	$\Delta LogR$	TOC Passey	TOC Core	R^2
5820	0.705	2.756	1.973	0,853
6000	0.358	0.669	0.964	
6090	0.675	0.602	1.231	
6180	0.778	0.307	0.411	
6270	1.003	1.734	1.691	
6360	0.551	0.201	0.225	
6450	0.642	0.171	0.184	
6630	0.530	1.071	1.172	
6720	0.731	2.016	2.034	

In addition, the maturity level of a source rock can be determined by using the correlation between S2 data and TOC data. The combination of these two data can be used to obtain the Level of Maturity (LOM) value.

Based on the correlation results of S2 data with TOC in Figure 12, this research data has a maturity level with a dominant LOM value of less than 7. So, it can be said that the source rock is classified as immature.

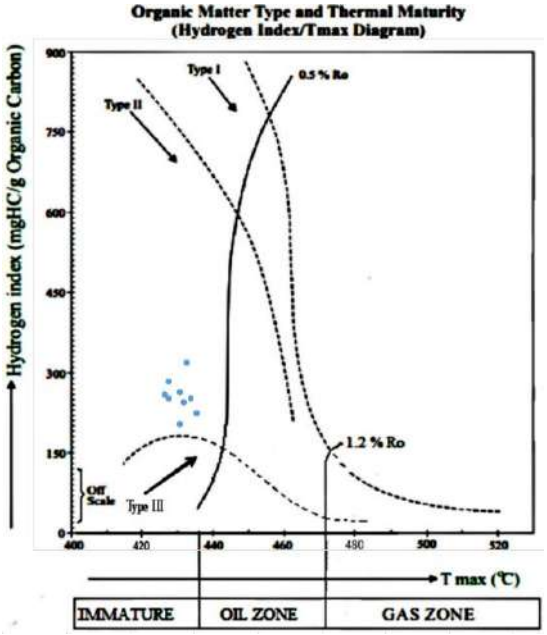

Figure 11. Quality of the Source Rock Zone at Well S-1.

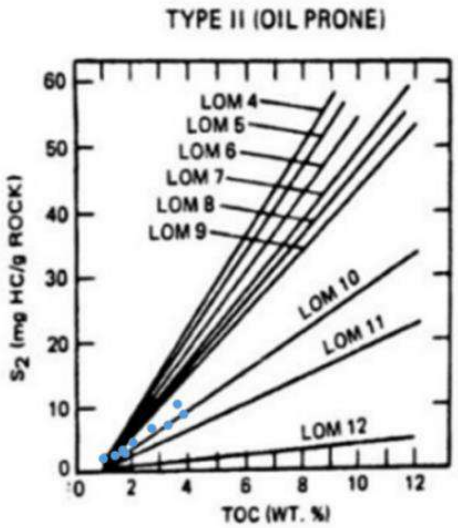

Figure 7. LOM values are based on S2 and TOC core data.

Seismic Data Analysis

Figure 13 is 2D seismic data on line A-79 which is traversed by K-1 well data. This line will be a reference in making composite lines and picking horizons at a later stage. Figure 13 shows the results of horizon picking on line A-79 which is a reference in picking horizons on other lines. The pink line shows the upper layer of the source rock and the light blue line shows the lower layer of the source rock.

Figure 14 is an interpretation of the lithology of the source rock zone (reservoir) on seismic data. Based on the figure, it can be said that the reservoir zone has a high GR value, so it has a shale lithology.

Figure 15 is the Top (upper layer) of the reservoir zone. Based on Figure 15, it can be seen that there is a low area indicated by light blue to dark blue color, ranging in value between 2100 m - 2700 m. If observed, the area around Well K-1, Well S-1, and Well C-1 includes a low area that allows it to be interpreted as a geological structure in the form of a syncline. Thus, it is possible that there is a hydrocarbon trap on the North-West side of the study area. Figure 16 shows the bottom of the reservoir zone. Based on Figure 16, it can be seen that there is a low area indicated by light blue to dark blue color, ranging in value between 2500 m - 3100 m.

If observed, the area around Well K-1, Well S-1, and Well C-1 includes a low area that allows it to be interpreted as a geological structure in the form of a syncline. So that it can allow the existence of hydrocarbon traps on the North-West side of the study area.

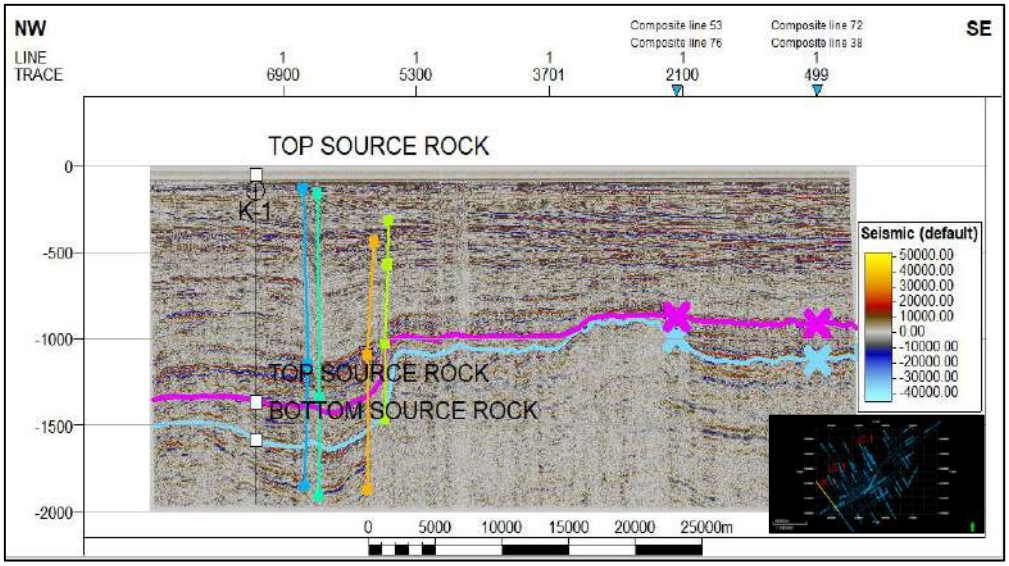

Figure 8. Horizon on Line A-79.

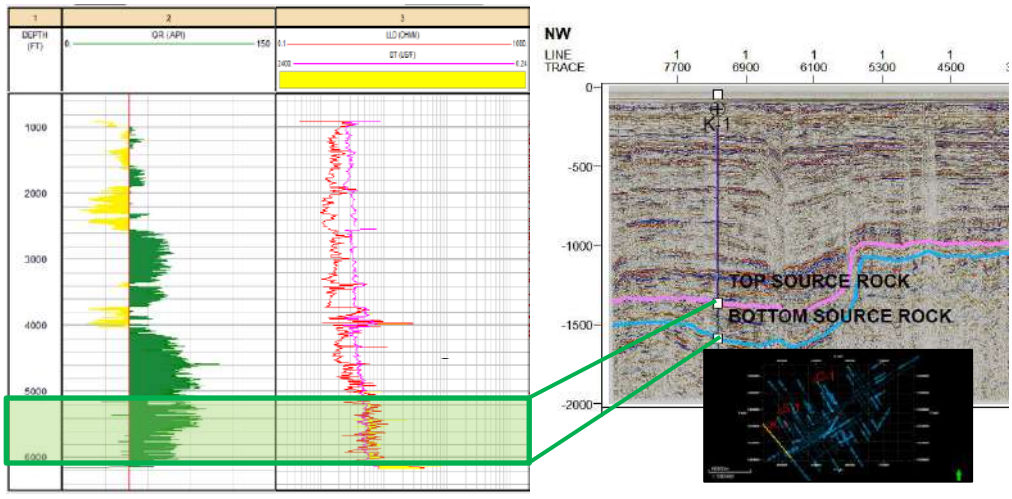

Figure 9. Source Rock Zone on Line A-79.

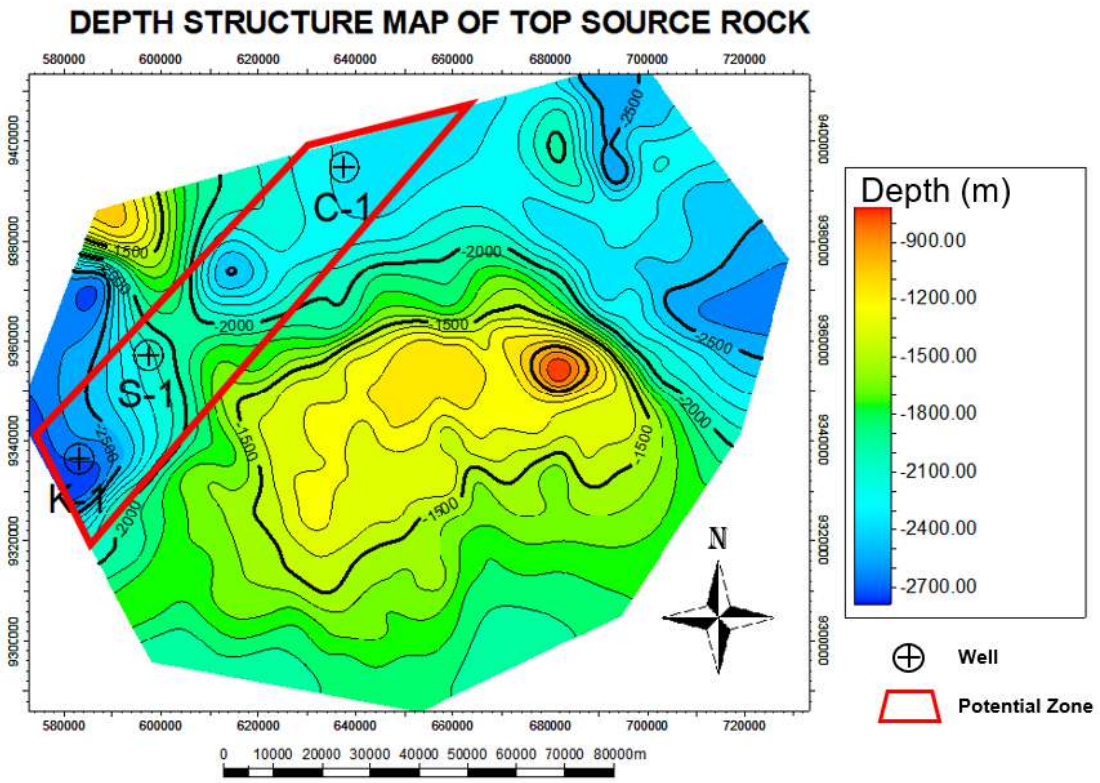

Figure 10. Top Reservoir Depth Structure Map.

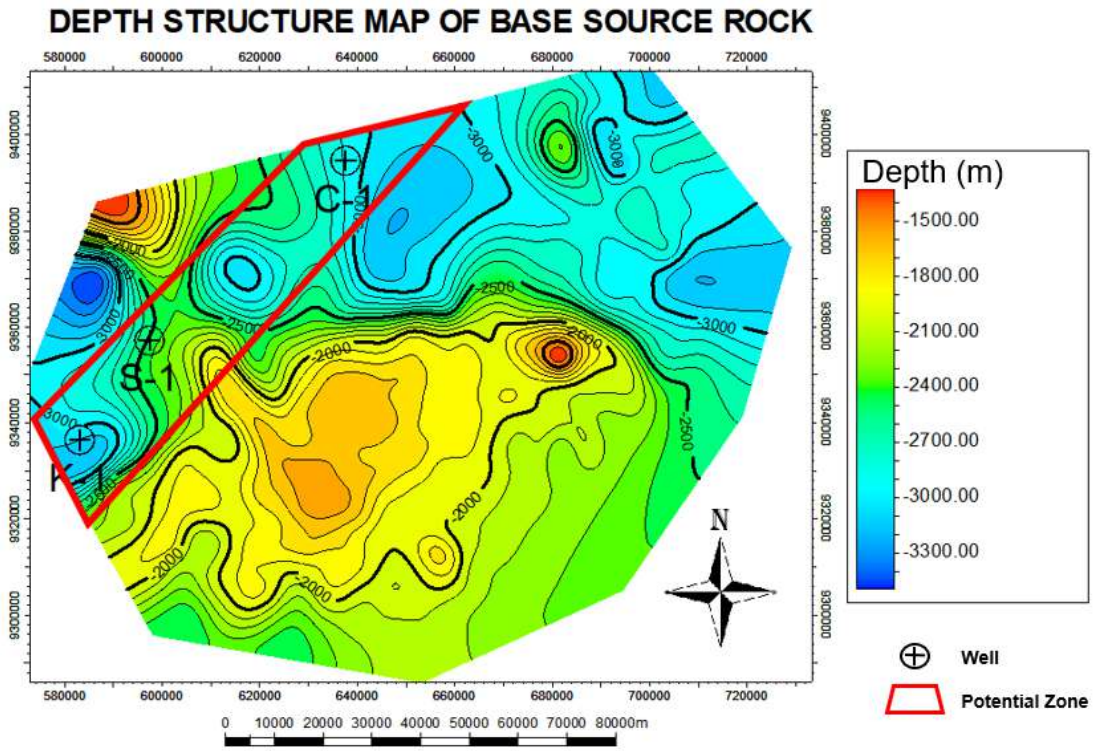

Figure 11. Bottom Reservoir Depth Structure Map.

Conclusion

Based on the results of qualitative and quantitative analysis based on well data, geochemical data, and seismic methods, the results of this study can be concluded as: The first, geochemical data analysis in Well S-1 shows that the reservoir zone in Field "X" of the North East Java Basin has Type II kerogen and an immature maturity level.

The second, based on prediction using the Passer method, the reservoir zone in Well S-1 has an average TOC value of 2.38% with very good quality. Well K-1 has an average TOC value of 4.41% with excellent quality, and Well C-1 has an average TOC value of 4.83% with excellent quality. The last, the reservoir zone in Field "X" of the North East Java Basin is in a low area in the northwest direction of the study area.

Acknowledgments

Thanks to all parties who have helped with this research, especially LPPM Unila.

Author Contribution

Rahmat Catur Wibowo: Conceived and designed the experiments, Performed the experiments, Analyzed and interpreted the data, and Wrote the paper; Aryka Claudia Eka Putri: Performed the experiments; Ordas Dewanto: Analyzed and interpreted the data.

Conflict of Interest

The authors declare that they have no known competing financial interests or personal relationships that could have appeared to influence the work reported in this paper.

References

Aprilana, C., Premonowati, P., Hanif, I. S., Choirotunnisa, C., Shirly, A., Utama, M. K., Sinulingga, Y. R., & Syafitra, F. (2018). New Prespective Paleogeography of East Java Basin; Implicationrespond to Oil and Gas Eksploration at Kujung Formation Carbonate Reservoar. *IOP Conference Series: Earth and Environmental Science*, 132(012006). https://doi.org/10.1088/1755-1315/132/1/012006

Athmer, W., Borgos, H. G., Dahl, G. V., Tetzlaff, D. M., Handwerger, D., & Sonneland, L. (2014). Integrating Seismic Interpretation, Classification and Geologic Process Modeling for Shale Reservoir. *Proceedings of the 9th Hydrocarbon Exploration and Development Congress and Exhibition. Mendoza*, pp. 461–477.

Barber, E. J., Crow, M. J., & Milsom, J. S. (2005). *Sumatra: Geology, Resources, and Tectonic Evolution. (Vol. 4, Issue 3)*. The Geological Society.

Brooks, J., Welte, D., & Jovanovich, H.B. (1984). *Petroleum Geochemistry*.

Crain, E. R. (2000). *Petrophysical Handbook.* https://spec2000.net/11-vshtoc.htm.

del Monte, A. A., Antonielli, E., de Tomasi, V., Luchetti, G., Paparozzi, E., & Gambacorta, G. (2018). Methods for source rock identification on seismic data: An example from the Tanezzuft Formation (Tunisia). *Marine and Petroleum Geology*, 91, 108–124. https://doi.org/10.1016/j.marpetgeo.2017.12.015

Devi, A., Boruah, S., & Gilfellon, G. B. (2017). Geochemical Characterization of Source Rock from the North Bank Area, Upper Assam Basin. *Journal Geological Society of India*, 89, 429–434. https://doi.org/10.1007/s12594-017-0625-8

El-Khadragy, A. A., Shazly, T. F., Mousa, D. A., Ramadan, M., & El-Sawy, M. Z. (2018). Integration of well log analysis data with geochemical data to evaluate possible source rock. Case study from GM-ALEF-1 well, Ras Ghara oil Field, Gulf of Suez-Egypt. *Egyptian Journal of Petroleum*, 27(4), 911–918. https://doi.org/10.1016/j.ejpe.2018.01.005

Fajana, A. O., Ayuk, M. A., Enikanselu, P. A., & Oyebamiji, A. R. (2019). Seismic interpretation and petrophysical analysis for hydrocarbon resource evaluation of 'Pennay' field, Niger Delta. *Journal of Petroleum Exploration and Production Technology*, 9, 1025–

1040. https://doi.org/10.1007/s13202-018-0579-4

Fatahillah, Y., Utama, W., Suprayogi, K., Hilyah, A., & Maulana, I. (2017). Source rock formation evaluation using TOC & Ro log model based on well-log data procesing : study case of Ngimbang formation, North East Java basin. *MATEC Web of Conferences*, 101, 04016. https://doi.org/10.1051/matecconf/201710104016

Field, W., Raef, A. E., Mattern, F., Philip, C., & Totten, M. W. (2015). 3D seismic attributes and well-log facies analysis for prospect identification and evaluation: interpreted palaeoshoreline implications, Weirman Field, Kansas, USA. *Journal of Petroleum Science and Engineering*, 133, 40–51. https://doi.org/10.1016/j.petrol.2015.04.028

Harilal, & Tandon, A. K. (2012). Unconventional Shale-gas plays and their characterization through 3-D seismic attributes and logs. *9 Biennial International Conference & Exposition on Petroleum Geophysics*. p. 8. https://spgindia.org/spg_2012/spgp083.pdf

Habib, M., Charles, S. P., Guangqing, Y., Danlami, M. S., Congjiao, X., Jakada, H., Abba, H. A., & Omeiza I. A. (2016). An inversion of reservoir properties based on a concurrent modeling approach : the case of a West African reservoir. *Journal of Petroleum Exploration and Production Technology*, 6(4), 617–628. https://doi.org/10.1007/s13202-016-0236-8

Helal, A., Farag, K., & Shihata, M. (2015). Unconventional seismic interpretation workflow to enhance seismic attributes results and extract geobodies at Gulf of Mexico case study. *Egyptian Journal of Geology*, 59, 1–14.

Mudjiono, R., & Pireno, G. E. (2002). Exploration of the North Madura Platform, Offshore East Java, Indonesia. *Proceedings, Indonesian Petroleum Association*. Jakarta, pp. 707–726. https://doi.org/10.29118/ipa.980.707

Muther, T., Qureshi, H. A., Syed, F. I., Aziz, H., Siyal, A., Dahaghi, A. K., & Negahban, S. (2021). Unconventional hydrocarbon resources: geological statistics, petrophysical characterization, and field development strategies. *Journal of Petroleum Exploration and Production Technology*, 12, 1463–1488. https://doi.org/10.1007/s13202-021-01404-x

Niu, H., Han, X., Wei, J., Zhang, H., & Wang, B. (2018). Geochemical characteristics of Lower Jurassic source rocks in the Zhongkouzi Basin Geochemical characteristics of Lower Jurassic source rocks in the Zhongkouzi Basin. *IOP Conf. Series: Earth and Environmental Science*, 108(032050). https://doi.org/10.1088/1755-1315/108/3/032050

Olatunde, P. S. (2016). Geochemical Techniques for the Analysis of Geochemical Data and its Application in the Nigerian Oil and Gas Industries. *Chemical Sciences Journal*, 7(3), 1000137. https://doi.org/10.4172/2150-3494.1000137

Passey, Q. R., Bohacs, K. M., Esch, W. L., Klimentidis, R., & Sinha, S. (2010). From Oil-Prone Source Rock to Gas-Producing Shale Reservoir – Geologic and Petrophysical Characterization of Unconventional Shale-Gas Reservoirs. *International Oil and Gas Conference and Exhibition in China, Beijing, China*. https://doi.org/10.2118/131350-MS

Passey, Q. R., Creaney, S., Kulla, J. B., Moretti, F. J., & Stroud, J. D. (1990). A Practical Model for Organic

Richness from Porosity and Resistivity Logs. *The American Association of Petroleum Geologist Bulletin*, 74(12), 1777–1794. https://doi.org/10.1306/0C9B25C9-1710-11D7-8645000102C1865D

Peters, K. E., & Cassa, M. R. (1994). Chapter 5 - Applied Source Rock Geochemistry. In *The petroleum system–from source to trap*. AAPG Memoir 60 93–120.

Satyana, A. H., & Purwaningsih, M. E. M. (2003). Geochemistry of the East Java Basin: New Observations on Oil Grouping, Genetic Gas Types and Trends of Hydrocarbon Habitats. *Proceedings, Indonesian Petroleum Association*. Jakarta, p. 23. https://doi.org/10.29118/ipa.831.03.g.021

Scheeder, G., Weniger, P., & Blumenberg, M. (2020). Geochemical implications from direct Rock-Eval pyrolysis of petroleum. *Organic Geochemistry* 146, 104051. https://doi.org/10.1016/j.orggeochem.2020.104051

Setyawan, R., Subroto, E. A., Sapiie, B., Condronegoro, R., & Syam, B. (2020). Geochemical and Geomechanical Study on Gumai and Talangakar Formation to Determine Potential of Shale Gas in Jambi Sub-Basin, South Sumatra Basin. *Journal of Geoscience, Engineering, Environment, and Technology* 5, 94–102. https://doi.org/10.25299/jgeet.2020.5.2.4191

Song, D., He, D., & Wang, S. (2013). Source Rock Potential and Organic Geochemistry of Carboniferous Source Rocks. *Journal of Earth Science*, 24(3), 355–370. https://doi.org/10.1007/s12583-013-0339-9

Suharyati., Pambudi, S. H., Wibowo, J. L., & Pratiwi, N. I. (2019). *Indonesia Energy Out Look 2019*, DEWAN ENERGI NASIONAL. Jakarta.

Sumotarto, T. A., Haris, A., Riyanto, A., & Usman, A. (2017). Shale characterization on Barito field, Southeast Kalimantan for shale hydrocarbon exploration. *AIP Conference Proceedings*, 1862(030195), 1–6. https://doi.org/10.1063/1.4991299

Szabó, N. P., Valadez-vergara, R., Tapdigli, S., Ugochukwu, A., Szabó, I., & Dobróka, M. (2021). Factor analysis of well logs for total organic carbon estimation in unconventional reservoirs. *Energies (Basel)* 14, 1–17. https://doi.org/10.3390/en14185978

Wibowo, R. C. (2013). "Unconventional Reservoir" Shale Gas Potential Based On Source Rock Analysis In Sumatran Back Arc Basin. In Setiawan, N.I., Budianta, W., Idrus, A. (Eds.), *Proceedings of International Conference on Geological Engineering Geological Engineering Department, Engineering Faculty, Gadjah Mada University*. Geological Engineering Department, Engineering Faculty, Gadjah Mada University, Yogyakarta, pp. 151–163.

Wibowo, R. C., Ariska, S., & Dewanto, O. (2020). Inversi Geostatistik Menggunakan Analisa Multi-Atribut Stepwise Regression Untuk Karakterisasi Reservoir. *RISET Geologi dan Pertambangan* 30(2), 187 – 202.

Zhao, P., Ostadhassan, M., Shen, B., Liu, W., Abarghani, A., Liu, K., Luo, M., & Cai, J. (2019). Estimating thermal maturity of organic-rich shale from well logs: Case studies of two shale plays. *Fuel*, 235, 1195–1206. https://doi.org/10.1016/j.fuel.2018.08.037

Zou, G., Xu, Z., Peng, S., & Fan, F. (2018). Analysis of coal seam thickness and seismic wave amplitude : A wedge model. *Journal of Applied Geophysics*, 148, 245–255. https://doi.org/10.1016/j.jappgeo.2017.11.013

ISSN: 2579-5821 (Print)
ISSN: 2579-5546 (Online)
URL address: http://journal.unhas.ac.id/index.php/geocelebes
DOI: 10.20956/geocelebes.v7i2.22588

Jurnal Geocelebes Vol. 7 No. 2, October 2023, 168 – 175

Advanced Processing of 2D Marine Reflection Seismic Data Using the Common Reflection Surface (CRS) Stack Method with K-L Filter Application

Emir Dzakwan Kamal Zein[1*], Syamsurijal Rasimeng[1], Egie Wijaksono[2]

[1]Geophysics Engineering Department, Faculty of Engineering, University of Lampung, Indonesia.
[2]Research and Development Center of Oil and Gas Technology "LEMIGAS", South Jakarta, Indonesia.

*Corresponding author. Email: emirdzakwan63@gmail.com

Manuscript received: 11 September 2022; Received in revised form: 11 August 2023; Accepted: 14 August 2023

Abstract

Data processing using the seismic reflection method is an important stage in the exploration of natural resources and minerals. This research was conducted to determine the effective and efficient stacking and filtering methods in reconstructing the subsurface geological structure of the earth from the results of data processing using ProMAX software. The data processing method used is the conventional stack and the Common Reflection Surface (CRS) stack. Aperture values of 0 ms – 50 m and 3000 ms – 150 m in the CRS stack process produce the most optimum seismic sections. Both methods produce a different quality of seismic cross-section display. The 2D cross-section model from the conventional stack method looks noisier than the results from the CRS stack method. In addition, the reflector pattern on the cross-section of the results of the CRS stack method is clearer and visible with a relatively large amplitude compared to the results of the conventional stack method. To maximize the quality of data display, data enhancement is applied, which is the K-L filter. The eigenimages value of 0.10% on the K-L filter with a horizontal window width of 120 is used to reduce random noise. Thus, an increase in the S/N ratio will be obtained in the seismic data so that the 2D cross-sectional model of the seismic reflection method can approach the original conditions of the subsurface geological structure.

Keywords: conventional stack; common reflection surface stack; K-L filter.

Citation: Zein, E. D. K., Rasimeng, S., and Wijaksono, E. (2023). Advanced Processing of 2D Marine Reflection Seismic Data Using the Common Reflection Surface (CRS) Stack Method with K-L Filter Application. *Jurnal Geocelebes*, 7(2):168-175, doi: 10.20956/geocelebes.v7i2.22588

Introduction

The process of searching for natural resources and minerals can be done by utilizing seismic waves. The acquisition of the seismic method utilizes seismic energy sources, including waterguns, dynamite, airguns, vibroseis, and others. Usually, exploration using the seismic method is divided into three stages, which are seismic data acquisition, seismic data processing and seismic data interpretation. Several seismic data processing processes can be grouped into four functions, which are data preparation, data correction, data reduction, and data quality improvement. Each company's workflow in processing seismic data is different. Conventional methods of processing seismic data consume significant time and resources (Desai et al., 2021).

The signal-to-noise ratio in the reflection seismic data is controlled by the seismic data collection stage. Conventional 2D surveys are generally carried out in the acquisition phase of the seismic method which has certain drawbacks. The development of seismic method acquisition techniques has not been able to solve the existing problems. The key to obtaining good interpretation results is that it depends

on the quality of the data obtained (Prabowo et al., 2021). One solution to data quality problems can be solved at the data processing stage (Zhu et al., 2015). A low signal-to-noise ratio can degrade the quality of data analysis such as inversion and imaging. Thus, seismic noise must be reduced as well as being a very important step (Chen et al., 2019).

Stacking is part of an important process in processing seismic data because it can produce an initial appearance below the earth's surface before the migration process takes place. Stacking must be applied to increase the signal-to-noise ratio. Several seismic data stacking methods that are commonly used include Common Mid-Point (CMP), Common Reflection Surface (CRS), and Common Reflection Point (CRP). One of the stacking method options used and the direction of measurement of important data is to reduce reflector ambiguity so that it is more efficient in reconstructing complex subsurface geological structures (Dani & Sule, 2021). The results of the conventional method stack depend heavily on the velocity model of the velocity analysis process (Daruartati et al., 2015). The CRS (Common Reflection Surface) method as a zero-offset (ZO) method for the stacking stage does not require a macro-velocity model (Garabito, 2021). With the use of the CRS method, the ambiguity in conducting velocity analysis is not too important to consider.

As for maximizing data quality after the stacking process, it is necessary to carry out a filtering process that aims to reduce the presence of noise. In this study, the eigenvector filter method is used as the main screening method. The eigenvector filter uses the Kahrunen-Loeve theory to decompose trace data into eigenimages using eigenvectors. The use of the Kahrunen-Loeve (K-L) method for seismic signals has been considered by Shukla & Jaiswal (2017), and most recently by Wang et al. (2020). In the field of image processing, the K-L transformation is commonly applied in data transmission and data analysis (Zaharov et al., 2014) as well as digital image enhancement (Sharma et al., 2018).

This research will explain how effective, efficient, and optimal the use of the Common Reflection Surface (CRS) stacking method is compared to conventional methods. The discussion regarding the application of the K-L filter in this study is also important because there is still little literature regarding the creation of this filter in reducing random noise.

Materials and Methods

This research was carried out at the Oil and Gas Testing Center "LEMIGAS". Data processing using ProMAX 2D software.

Data Preparation

The research data used is 2D reflection seismic data as a result of measurements in the Nias Sea by the Research and Development Institute for Oil and Gas Technology "LEMIGAS".

Table 1. Acquisition Parameters.

Acquisition Parameters	GM3-BIO-NIAS-L10.1
Source Interval	25 m
Group Interval	12.5 m
Total source	548
Total channel	96
Minimum Offset	50 m
Maximum Offset	1237.5 m
CDP Interval	6.25 m
Maximum Fold	24
Line Length	13.675 m
Line Azimuth	40°

Data processing

Seismic data processing is carried out using two different methods, which are the conventional method and the Common Reflection Surface (CRS) method. The use of two methods to compare the level of the ratio to the signal in order to obtain a subsurface model that matches the original conditions. This data processing consists of

various steps arranged in a flow workspace. The flow consists of several processes, including data input, geometry setting, editing, filtering, True Amplitude Recovery (TAR), deconvolution, velocity analysis, stacking, and data enhancement.

1. Conventional Stack

The conventional stack method is performed by averaging the NMO-corrected data or migrated data sets (Jang & Lee, 2022). This method is only optimal when the noise components in all traces are unrelated, normally distributed, stationary, and with the same magnitude (Mandal et al., 2014; Pussak et al., 2014). Common-midpoint stacking (CMP) is a method commonly used in data processing because it can separate signals from the noise that has the same frequency.

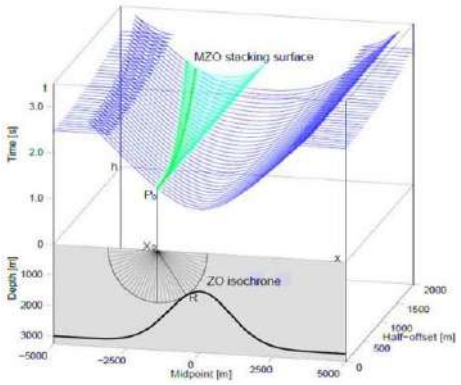

Figure 1. Operators of NMO/DMO stacks (Jäger, 1999).

In Figure 1 there is a symbol h as the offset distance, t is the time, and x is the CDP (Common Depth Point). Different rays can be reflected by a single CDP point. The sum along the multi-coverage data line indicated by the blue line is done to accumulate the different number of rays. After that, it is accumulated in one trace that represents the Po point. Between the time axis and the offset distance axis, there is a hyperbolic curve caused by the offset factor. Thus, a velocity analysis is needed so that the gather becomes straight. The CMP Stack operator is represented by a light green line. The conventional method stack stages are shown along the line in bold green.

2. *Common Reflection Surface* (CRS) *Stack*

The Common Reflection Surface (CRS) method introduced by Muller in 1998 is a zero-offset (ZO) simulation method based on 2-D data that does not require explicit knowledge of macro-velocity models (Pahlavanloo et al., 2017). The CRS method stack operator has several parameters using three attributes of the kinematic wave field which represent the curvature and coincident direction of propagation of the two wavefronts that appear on the acquisition surface, which are the normal incidence point (NIP) wavefront and the normal wavefront (Hubral, 1983).

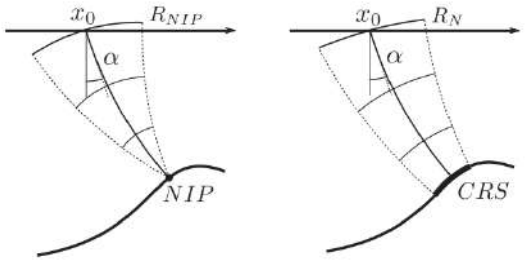

Figure 2. Normal incidence point (NIP), RNIP radius of curvature of a wavefront, and α is incidence angle (Rad & Macelloni, 2020).

The NIP wave radius or R_{NIP} parameter is a wave that propagates from the surface to the reflector and then returns to the surface. NIP waves shrink to a point on the reflector assuming that energy is not lost during wave propagation. The source of the new wave, which is the NIP wave, appears after the wave arrives at a reflector point so that the distance from the reflector to point x_0 can be determined. The waves that propagate in the normal direction or the R_N parameter are created from the area source around the point of occurrence. The R_N parameter contains information about the reflector curvature. The critical angle between the surface and the normal beam at x_0 is the angle parameter α (Daruartati et al., 2015). The CRS stack equation mathematically uses a second-order Taylor expansion written as follows:

$$t^2(x_m, h) = \left[t_0 + \frac{2\sin\alpha}{v_0}(x_m - x_0)\right]^2 + \frac{2t_0\cos^2\alpha}{v_0}\left[\frac{(x_m - x_0)^2}{R_N} + \frac{h^2}{R_{NIP}}\right] \quad (1)$$

Based on Equation (1), the time sample is symbolized (t_0). Meanwhile (x_0) is the coordinate of the appearance of the normal beam at half offset (h) equal to zero, $(x_m - x_0)$ is the midpoint aperture. The constant velocity near the surface is (v_0). The radius of normal wave curvature is symbolized (R_N), while the normal incident point radius of curvature is symbolized (R_{NIP}), and (α) is the angle of incidence of the reflected wave.

The CRS method can get closer to the actual subsurface geological model by accumulating the distances of the CMP and CDP around it without requiring velocity analysis. In Figure 3 the sum along the midpoint half offset surface is carried out at the CRS Stack stage which is indicated by the green line and then the product is accumulated at the Po point.

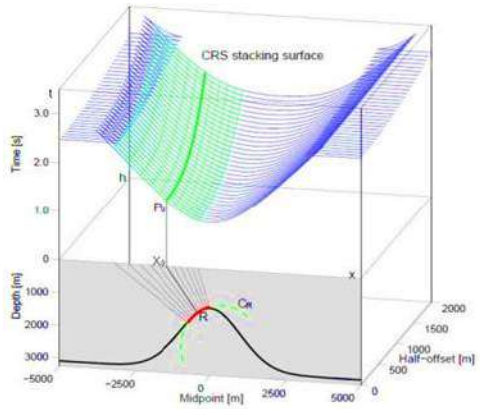

Figure 3. Operator from CRS stack (Jäger, 1999)

3. Data Enhancement

The eigenvector filter (Figure 4) is the same as the K-L Kahrunen-Loeve transformation (Hsu, 1990). The NMO-corrected 2D seismic section is treated as a 2D matrix which can be decomposed into its eigenvalues with the appropriate eigenvalues. The existence of a seismic event in the form of a flat reflection pattern is indicated by a high eigenvalue. Conversely, seismic events that are random and less prominent or include noise are shown with small eigenvalues. Thus, improving data quality can take advantage of this filter. If $S(t, x)$ is a data matrix, the corresponding singular-value decomposition (SVD) can be written as $S = U\sum V^T$. Meanwhile, U and V are unitary matrices consisting of left and right eigenvectors of S and $\sum$ a diagonal matrix containing eigenvalues of S (Liu & Liu, 2020).

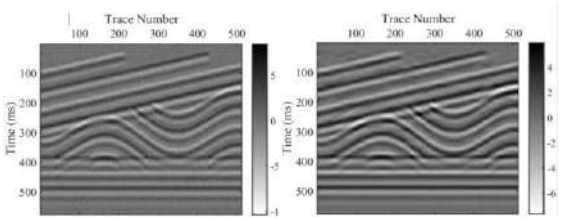

Figure 4. An example of implementing the K-L transformation (Wang et al., 2020).

Results and Discussion

The results of this study are seismic cross-sections with intervals of 0-2200 ms obtained from data processing using the conventional stack method and the CRS stack method both before and after applying data enhancement using the K-L filter.

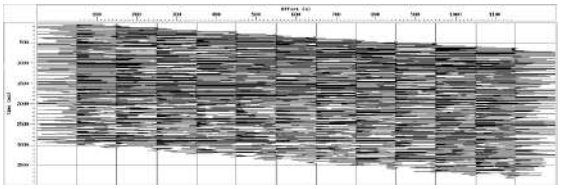

Figure 5. CMP gather.

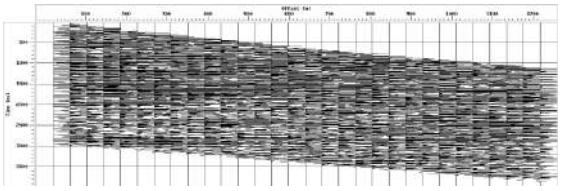

Figure 6. CRS supergather.

The CRS method has a higher number of traces than conventional methods. The number of traces in the CRS Supergather is controlled by the aperture selection because the aperture in the CRS Stack operator indicates the number of traces from adjacent CMP used in the stacking process.

The CRS method also has a similar amplitude and collects so that it produces a better gather appearance than the conventional method. Gather on the conventional method looks more random and fluctuating. This is shown in Figure 5 and Figure 6.

1. Conventional Stack Method

The stacking process using conventional methods before applying data enhancement on GM3-BIO-NIAS-L10.1 produces a subsurface model as shown in Figure 7. Random noise is still visible in the display which is partially indicated by a yellow box so that it disrupts the main reflector pattern and can complicate later interpretation.

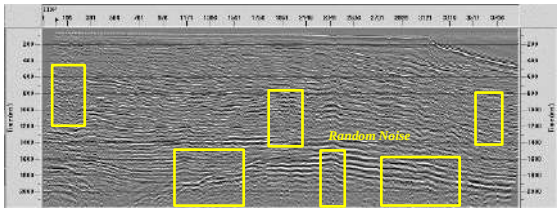

Figure 7. The result of the conventional method stack without the K-L filter.

2. CRS Stack Method

The stacking process using the CRS method on GM3-BIO-NIAS L10.1 before data enhancement is shown in Figure 8. The ZO aperture values on the CRS stack are 0 – 50 ms and 3000 – 150 ms. This value is selected based on trials so that the most optimum cross-sectional quality can be obtained. The appearance of the subsurface model looks cleaner than conventional methods even though data enhancement has not been applied. The main reflector pattern with a large amplitude is visible at certain time intervals indicated by red arrows.

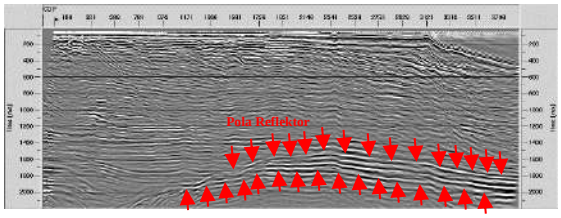

Figure 8. CRS method stack results without K-L filter.

3. Application of K-L Filters

This filter is applied to the conventional method stack results and the CRS method stack results. Generally, the eigenimages in this filter are divided into 3 groups based on their value. Flat components are generally reconstructed using low eigenimages, dipping components using middle eigenimages, and more random components using a higher number of eigenimages. Therefore, to display the noise output from the results of the conventional stack method and the CRS method which will be reduced later by the K-L filter, can use the eigenimage value range of 10% to 100% with a horizontal window width of 120 as shown in Figure 9 and Figure 10.

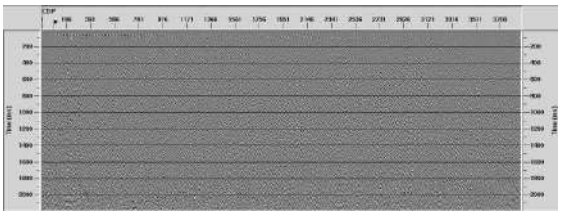

Figure 9. K-L filter noise output from conventional stack results.

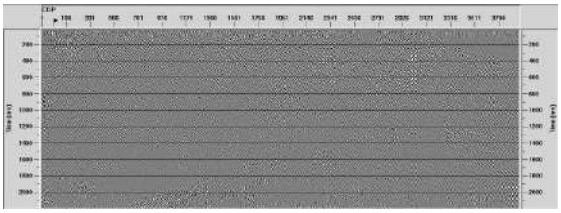

Figure 10. K-L filter noise output from CRS stack results.

The application of the K-L filter to the two results of the stacking method uses an eigenimages value range of 0% to 10% so that the output noise that was previously generated with an eigenimages value range of 10-100% will be reduced. The horizontal window width used is 120, which is obtained from the trial results while still based on existing theory. Thus, the results obtained from the conventional stack method after the application of data enhancement are shown in Figure 11, while Figure 12 is the result of the CRS method

stack after the application of data enhancement.

Based on the seismic section, the results of the conventional stack method by applying the K-L filter in Figure 11 shows that the random noise has been reduced, even though the 2D seismic section still looks relatively noisy. Likewise in Figure 12 which is a seismic cross-section of the results of the CRS stack method by applying the K-L filter, the presence of random noise has been maximally eliminated so that the 2D seismic cross-section display is much cleaner than the stack results display using conventional methods with the application of data enhancement. The main reflector pattern is clearer and seen with a larger amplitude in Figure 12. This indicates an increase in seismic resolution and signal-to-noise ratio after using the CRS method and combined with the application of data enhancement using the K-L filter.

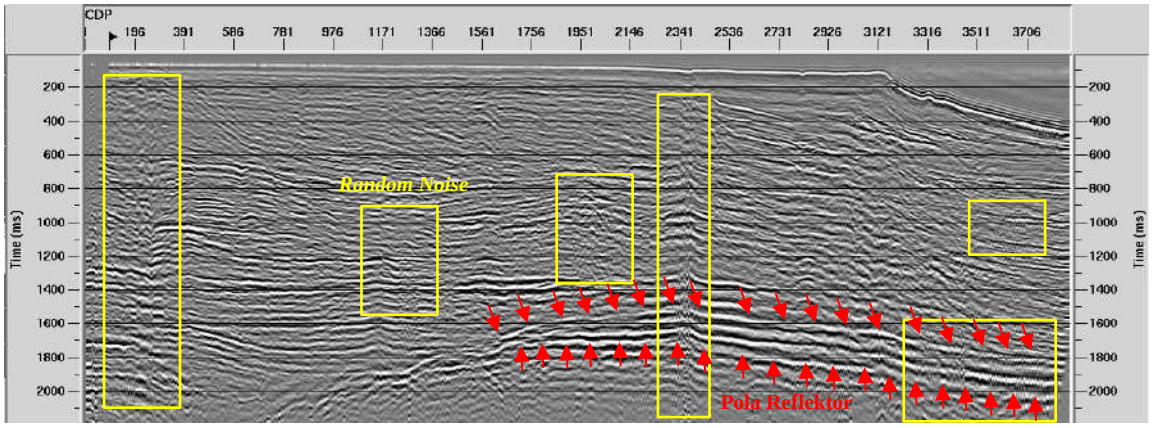

Figure 11. Results of conventional stacking method with K-L filter.

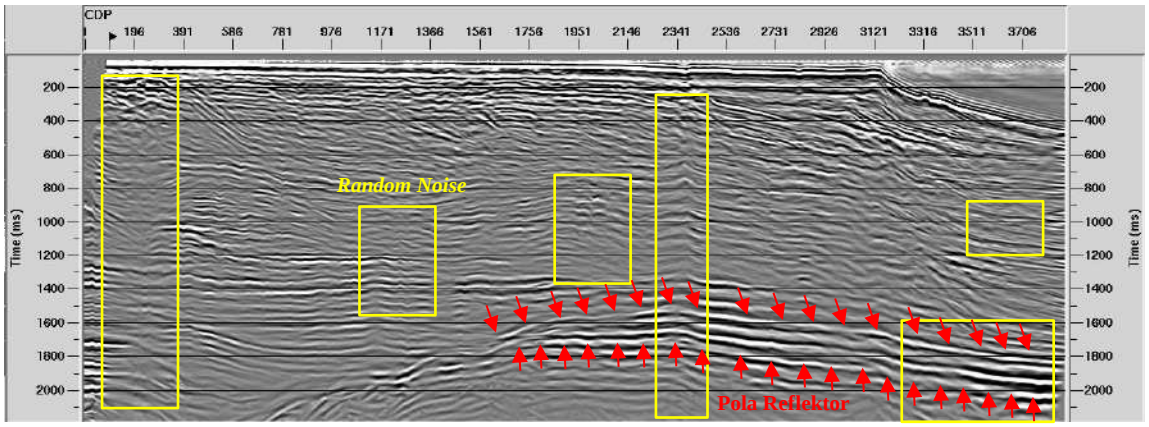

Figure 11. Results of CRS stacking method with K-L filter.

Conclusion

Processing of seismic data using the conventional stack method with the K-L filter combination has not yet produced an optimum 2D seismic cross-section so the use of the Common Reflection Surface (CRS) stack method combined with the K-L filter is required in order to increase the relatively high signal-to-noise ratio.

Acknowledgments

Thanks are conveyed to the Research and Development Center of Oil and Gas Technology "LEMIGAS" which has provided data and permission for this research to take place.

Author Contribution

E.D.K.Z. write theory, perform data processing, and perform data analysis. S.R.

and E.W. validate analytical methods and help develop this research. All authors discussed the results and contributed to the final manuscript.

Conflict of Interest

All authors declare that they have no conflicts of interest.

References

Chen, Y., Zhang, M., Bai, M., & Chen, W. (2019). Improving the signal-to-noise ratio of seismological datasets by unsupervised machine learning. *Seismological Research Letters*, 90(4), 1552-1564. https://doi.org/10.1785/0220190028

Dani, I., & Sule, M. R. (2021). Pemodelan Seismik pada Struktur Geologi Kompleks menggunakan Metode Common Reflection Surface (CRS). *Jurnal Geofisika Eksplorasi*, 7(3), 164–177. https://doi.org/10.23960/jge.v7i3.135

Daruartati, H., Setyawan, A., & Kusuma, I. A. (2015). Aplikasi Metode Common Reflection Surface (Crs) Untuk Meningkatkan Hasil Stack Data Seismik Laut 2d Wilayah Perairan "Y". *Youngster Physics Journal*, 4(4), 291–298. https://ejournal3.undip.ac.id/index.php/bfd/article/view/9407

Desai, A., Xu, Z., Gupta, M., Chandran, A., Vial-Aussavy, A., & Shrivastava, A. (2021). Raw nav-merge seismic data to subsurface properties with mlp based multi-modal information unscrambler. *Advances in Neural Information Processing Systems*, 34, 8740–8752. https://openreview.net/pdf?id=HLalhDvDwrQ

Garabito, G. (2021). Prestack seismic data interpolation and enhancement with common-reflection-surface–based migration and demigration. *Geophysical Prospecting*, 69(5), 913–925. https://doi.org/10.1111/1365-2478.13074

Hsu, K. (1990). Wave separation and feature extraction of acoustic well-logging waveforms using Karhunen-Loeve transformation. *Geophysics*, 55(2), 176–184. https://doi.org/10.1190/1.1442824

Hubral, P. (1983). Computing true amplitude reflections in a laterally inhomogeneous earth. *Geophysics*, 48(8), 1051–1062. https://doi.org/10.1190/1.1441528

Jäger, R. (1999). *The common reflection surface stack: theory and application*. MSc Thesis. University of Karlsruhe, Karlsruhe, Germany.

Jang, S., & Lee, D. (2022). Application of Reverse Time Migration to Faults Imaging in Rakhine Basin, Myanmar. *Geofluids*, 2022(1968793), 13 pages. https://doi.org/10.1155/2022/1968793

Liu, B., & Liu, Q. (2020). Random noise reduction using SVD in the frequency domain. *Journal of Petroleum Exploration and Production Technology*, 10, 3081–3089. https://doi.org/10.1007/s13202-020-00938-w

Mandal, B., Sen, M. K., Vaidya, V. R., & Mann, J. (2014). Deep seismic image enhancement with the common reflection surface (CRS) stack method: evidence from the Aravalli–Delhi fold belt of northwestern India. *Geophysical Journal International*, 196(2), 902–917. https://doi.org/10.1093/gji/ggt402

Pahlavanloo, A., Soleimani Monfared, M., & Gallo, C. (2017). Improving seismic image in complex structures by new solving strategies in the CO-CRS and the CO-CDS methods. *Iranian Journal of Geophysics*, 10(5), 42–56. https://dorl.net/dor/20.1001.1.20080336.1396.10.5.5.2

Prabowo, A., Junursyah, G. M. L., & Hidayat, W. (2021). Analisis Kualitas Data Magnetotelurik Berdasarkan Parameter Koherensi Pada Daerah

Bandung, Jawa Barat. *Jurnal Mineral, Energi, dan Lingkungan*, 4(2), 78–84. https://doi.org/10.31315/jmel.v4i2.3679

Pussak, M., Bauer, K., Stiller, M., & Bujakowski, W. (2014). Improved 3D seismic attribute mapping by CRS stacking instead of NMO stacking: Application to a geothermal reservoir in the Polish Basin. *Journal of Applied Geophysics*, 103, 186–198. https://doi.org/10.1016/j.jappgeo.2014.01.020

Rad, P. B., & Macelloni, L. (2020). Improving 3D water column seismic imaging using the Common Reflection Surface method. *Journal of Applied Geophysics*, 179, 104072. https://doi.org/10.1016/j.jappgeo.2020.104072

Sharma, A., Singh, A. K., & Kumar, P. (2018). Combining haar wavelet and Karhunen-Loeve transform for robust and imperceptible data hiding using digital images. *Journal of Intelligent Systems*, 27(1), 91-103. https://doi.org/10.1515/jisys-2017-0032

Shukla, K., & Jaiswal, P. (2017). Wavefield-based regularization of multicomponent seismic data. *SEG Technical Program Expanded Abstracts 2017* (pp. 2575-2579). Society of Exploration Geophysicists. https://doi.org/10.1190/segam2017-17794904.1

Wang, D., Gao, J., Liu, N., & Jiang, X. (2020). Structure-oriented DTGV regularization for random noise attenuation in seismic data. *IEEE Transactions on Geoscience and Remote Sensing*, 59(2), 1757–1771. https://doi.org/10.1109/TGRS.2020.3001141

Zaharov, V. V., Farahi, R. H., Snyder, P. J., Davison, B. H., & Passian, A. (2014). Karhunen–Loève treatment to remove noise and facilitate data analysis in sensing, spectroscopy and other applications. *Analyst*, 139(22), 5927–5935. https://doi.org/10.1039/C4AN01300J

Zhu, L., Liu, E., & McClellan, J. H. (2015). Seismic data denoising through multiscale and sparsity-promoting dictionary learning. *Geophysics*, 80(6), WD45-WD57. https://doi.org/10.1190/geo2015-0047.1

ISSN: 2579-5821 (Print)
ISSN: 2579-5546 (Online)
URL address: http://journal.unhas.ac.id/index.php/geocelebes
DOI: 10.20956/geocelebes.v7i2.22223

Jurnal Geocelebes Vol. 7 No. 2, October 2023, 176 – 185

Relocation of the Hypocenter of an Earthquake with the Double Difference Method in the Regional Study Area of Yogyakarta

Fani Rohmiasih[1], Andi[1]*, Nugroho Budi Wibowo[2]

[1]Physics, UIN Sunan Kalijaga, Yogyakarta, Indonesia.
[2]Badan Meteorologi Klimatolog dan Geofisika, Yogyakarta, Indonesia.

*Corresponding author. Email: andi@uin-suka.ac.id

Manuscript received: 19 August 2022; Received in revised form: 12 April 2023; Accepted: 28 August 2023

Abstract

The relocation of the earthquake hypocentre is necessary in order to determine the position of the earthquake centre with higher accuracy. An accurate hypocentre position is important for earthquake-prone areas mapping, seismicity analysis, and fault zone identification. The double difference algorithm technique using the hypoDD program can be used for hypocentre relocation. This article reports the earthquake relocation of 23 earthquakes in the Yogyakarta region recorded at four observation stations. The result shows that the hypocentre shift spreads randomly with a shift distance of less than 20 km, with the most shifting direction of the epicentre to the northeast. The Earthquake's hypocentre after relocation in the land area is estimated to be triggered by a fault under the Gamping Wungkal Formation, while the earthquake around Mount Merapi is estimated to be triggered by volcanic activity. The Relocation result in the sea area show that the hypocentre leads to the subduction line.

Keywords: double difference; fault; hypoDD; residual histogram; subduction.

Citation: Rohmiasih, F., Andi, A., and Wibowo, N. B. (2023). Relocation of the Hypocenter of an Earthquake with the Double Difference Method in the Regional Study Area of Yogyakarta. *Jurnal Geocelebes* 7(2):176-185, doi: 10.20956/geocelebes.v7i2.22223

Introduction

Yogyakarta is in the collision zone of the Eurasian plate with Indo-Australian plate which makes this region prone to earthquakes (Fathani & Wilopo, 2017). Moreover, the earthquakes in Yogyakarta were caused by the activities of the local faults in this region (Wibowo & Sembri, 2017). Earthquake researches need to be carried out as disaster mitigation measure. The exact location of the hypocentre is important for mapping the earthquake-prone areas and detailed investigation of the geological subsurface.

A common problem in seismicity analysis is that hypocentres are sometimes located far from the fault where the earthquake originated. Factors affecting the accuracy of hypocentre determination include the type and number of seismic waves recorded, the geometry of the observation station, the accuracy of the reading of the time of first arrival, and knowledge of the seismic wave velocity structure. There are many ways to determine the position of the hypocentre more precisely. One technique that can be used for relocation earthquake hypocentre is double difference method (Puspita C et al., 2015; Sabtaji & Nugraha, 2015; Diaz et al., 2018; Kusmita et al., 2020). This method uses travel time data from two earthquake events to an observation station (Waldhauser & Ellsworth, 2000; Harlianti et al., 2017; Setiadi et al., 2017; Setiadi & Rohadi, 2018).

Yulianto et al. (2017) used the double difference method to relocate hypocentres around Molucca collision zone. The results show better hypocentre location according to the RMS of time residual shifting.

Waldhauser & Ellsworth (2000) used the double difference method to relocate earthquakes in the northern Haward fault zone in California. The result is a clearer picture of seismicity and shows a horizontal hypocentre line describing a small area of the fault where stress is released. In the study by Ramdhan et al. (2020), the double difference method is used to relocated the hypocentre of Central Java and surrounding areas. The result describes the Opak fault zone with dip fault plane inclined to the east and detect shallow magma activity of Merapi.

The purpose of this study is to relocate earthquakes that occurred in Yogyakarta in 2019 using earthquake data from BMKG. Result of the relocation are expected to improve the accuracy of hypocentre location. The position of the hypocentre after the displacement can then be used to analyse the tectonic features in the Yogyakarta region.

The Double Difference Method

The double difference method is one of the earthquake relocation techniques. This method was introduced by Waldhauser & Ellsworth (2000). The double difference method is the development of the Geiger method which uses travel time between the two hypocentres. The principle of the double difference method is if there are two centre earthquakes with a smaller distance between the two hypocentres compared to the distance to the observing station, then the wave beam pattern (raypath) and waveform of the two earthquakes can be considered the same (Setiadi et al., 2017; Supendi et al., 2019; Nurbaiti et al., 2019). Figure 1, describes an illustration of the double difference method. The black and white circles are earthquake events that are closed. The thick black lines show pairs of earthquakes with cross-corrected data. Dotted line shows earthquake pairs with catalogue/ bulletin data.

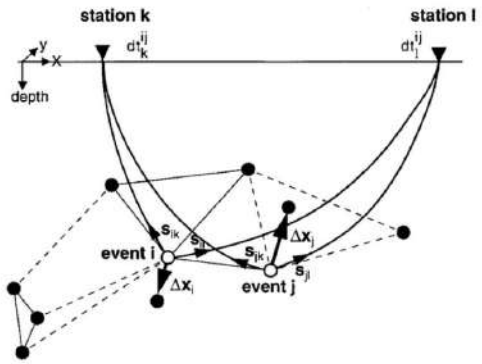

Figure 1. Illustration of the double difference method (Waldhauser & Ellsworth, 2000).

The double difference equation for relocating the earthquake hypocentre is expressed in the equation:

$$drk_{ij} = (Tk_i - Tk_j)_{obs} - (Tk_i - Tk_j)_{cal} \qquad (1)$$

The values of i and j indicate two adjacent hypocenters, and the values of k are recording stations for two adjacent hypocenters.

Method

In this research, the earthquake hypocentre in Yogyakarta was relocated using the double-difference method. The BMKG Yogyakarta research data includes 23 earthquake events and was recorded at four observation stations. The hypocentre was relocated using the hypoDD program, which used the double-difference method to relocate the earthquake hypocentre (Waldhauser, 2001; Utama et al., 2015; Syafriani et al., 2023).

The relocation of earthquake hypocenters using the double-difference method is done in two steps. First, the data are clustered using the program ph2dt. The second step is the relocation of the hypocenter with the calculation of the paired earthquake travel time using the program hypoDD. The complete procedure of the research flow is shown in Figure 2.

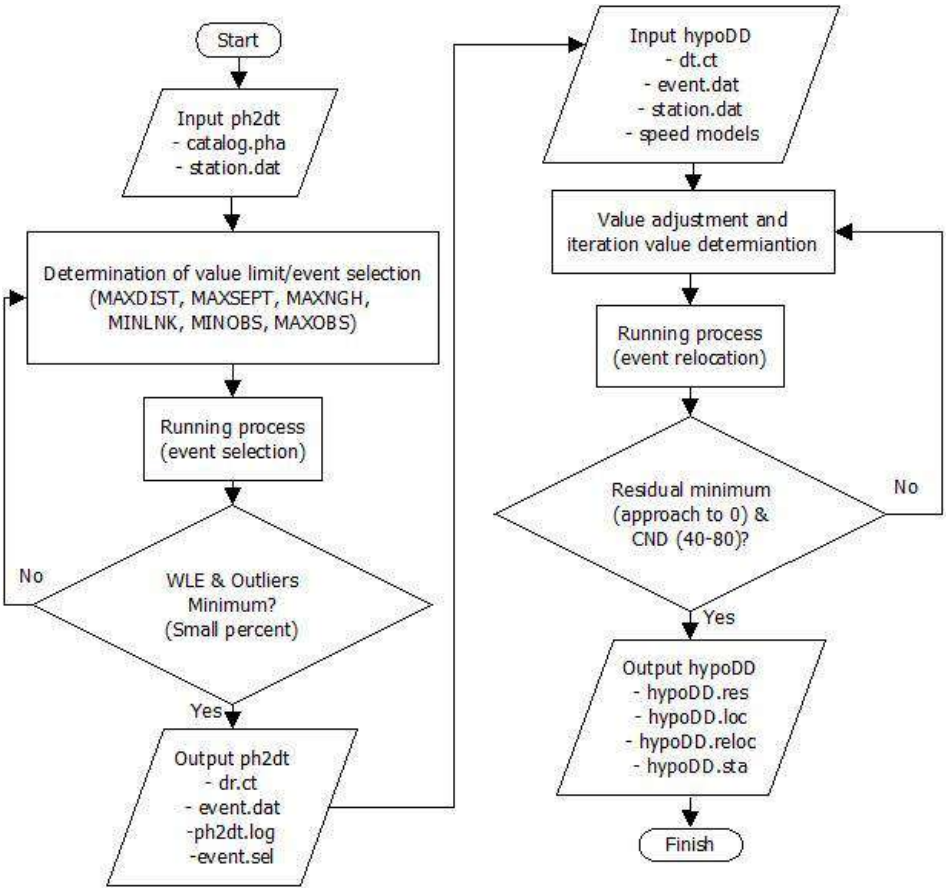

Figure 2. Research flow chart.

P wave velocity model for depths less than 20 km using Wegner wave velocity model, while for depth more than 20 km using the AK135 model. The results that need to be considered in hypoDD processing are the CND (Condition Number for the system of Double Difference equation) value and the residual value. The CND value is the ratio between the maximum and minimum values of the eigenvalues in equation used in the hypoDD program. The required CND values are between 40 and 80. The residual value is the RMS (Root Mean Square) value of the residual time generated by the hypoDD program.

Results and Discussion

The residual histogram is a graph that shows the residual time of earthquake waves. Figure 3, the residual histogram after relocation, shows that the residual values are closer to zero compared to the residual values before relocation. The result shows an improvement in quality when the distribution of the residual time values is considered. The residual time of the earthquake is the difference between the observed travel time and the calculation results. The closer the residual time is to zero, the closer the hypocenter is to the actual position. The research results map in Figure 4 shows that the location of earthquakes in the sea tends to change randomly or in all directions after resettlement. The earthquakes in the marine areas may originate from subduction in the south of Yogyakarta and active faults under the sea.

The distribution of earthquakes on the map before and after land resettlement shows in Figure 5 that there are 2 earthquake events around Mount Merapi and 13 earthquake events in the Gunungkidul area. The epicentre of the earthquake around Mount Merapi is located about 10 km south of the peak of Merapi. After the displacement, the

epicentre has moved closer to the summit of Mount Merapi. The earthquakes around Mount Merapi are earthquakes caused by volcanic tectonics (VT), i.e., earthquakes related to magma activity (Ramdhan et al., 2020). Data from Geological Agency of the Ministry of Energy and Mineral Resources show that the time of earthquake was close to the increase in volcanic activity Mount Merapi in October-November 2019.

Earthquakes in land areas mostly near minor faults in the Wonosari Formation. The Wonosari Formation has a layer thickness of 800 meters (Qodri & Sopamena, 2022). The earthquake hypocentre int the land are of the research results is at a depth of 3-18 km. This indicates that the earthquake is not sourced by faults in the Wonosari Formation, but may be caused by another, older formation beneath Wonosari Formation.

Figure 5 shows the geological composition of the study area. here are several formations under the Wonosari Formation, which are the Sambipitu Formation, the Nglanggran Formation, the Semilir Formation, the Oyo Formation, the Kobobutak Formation, and the Wungkal Formation. Thus, earthquakes from the land research area under the Wonosari Formation can be suspected under the Wungkal Formation (Limestone Wungkal) (Wibowo and Sembri, 2017), because the formation has the oldest age and is located at a depth of more than 1 km (Surono, 2009).

Figure 6 & 8 shows the distribution of earthquakes before and after relocation in earthquakes that occur in land areas with cross sections A-A'. Before the relocation there were many earthquake events with a depth of 10 km (fix depth) obtained from earthquake catalogue data. On the line A-A' at a depth of less than 20 km, there is a change in the hypocentre after relocation, some are shifted and shallower, others deeper. The changes in the distribution of location and depth earthquakes after relocation tend to be more evenly distributed and dominated by shallow earthquakes less than 20 km. Earthquakes less than 20 km deep are consistent with studies showing that the maximum depth of earth's crust in the study area has a maximum depth of 30 km (Ramdhan et al., 2020). Earthquakes in land areas with shallow depths and small magnitudes are possible due to local fault activity in the study area.

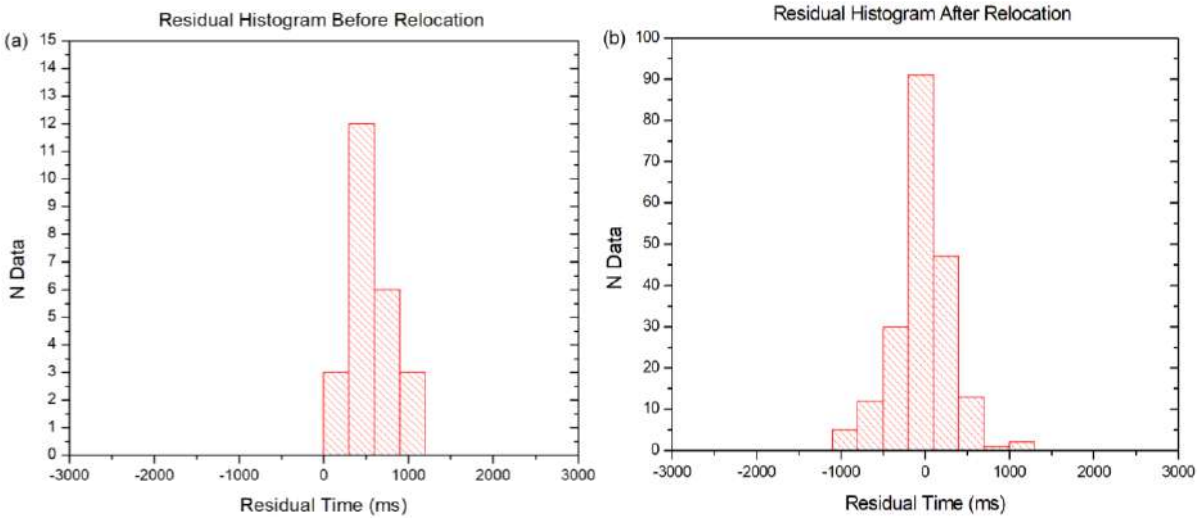

Figure 3. (a) - (b) Residual histogram before and after relocation, respectively.

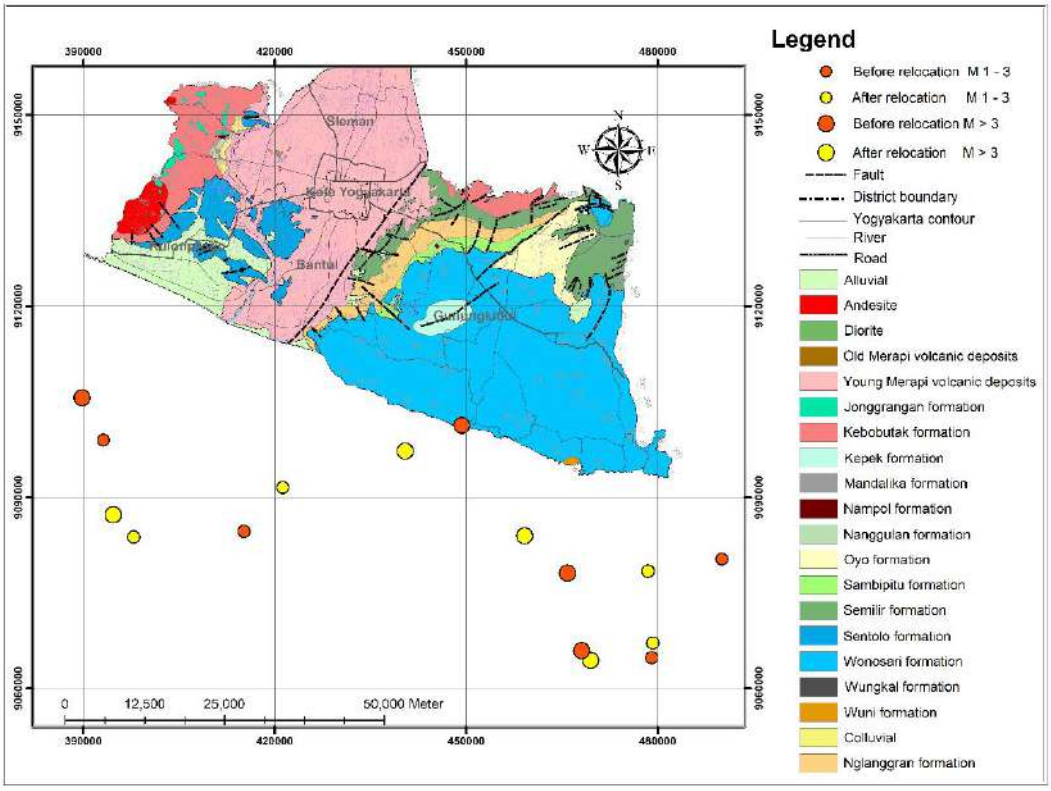

Figure 4. Distribution of sea area epicentres before and after relocation (modification from Wartono et al., 1977).

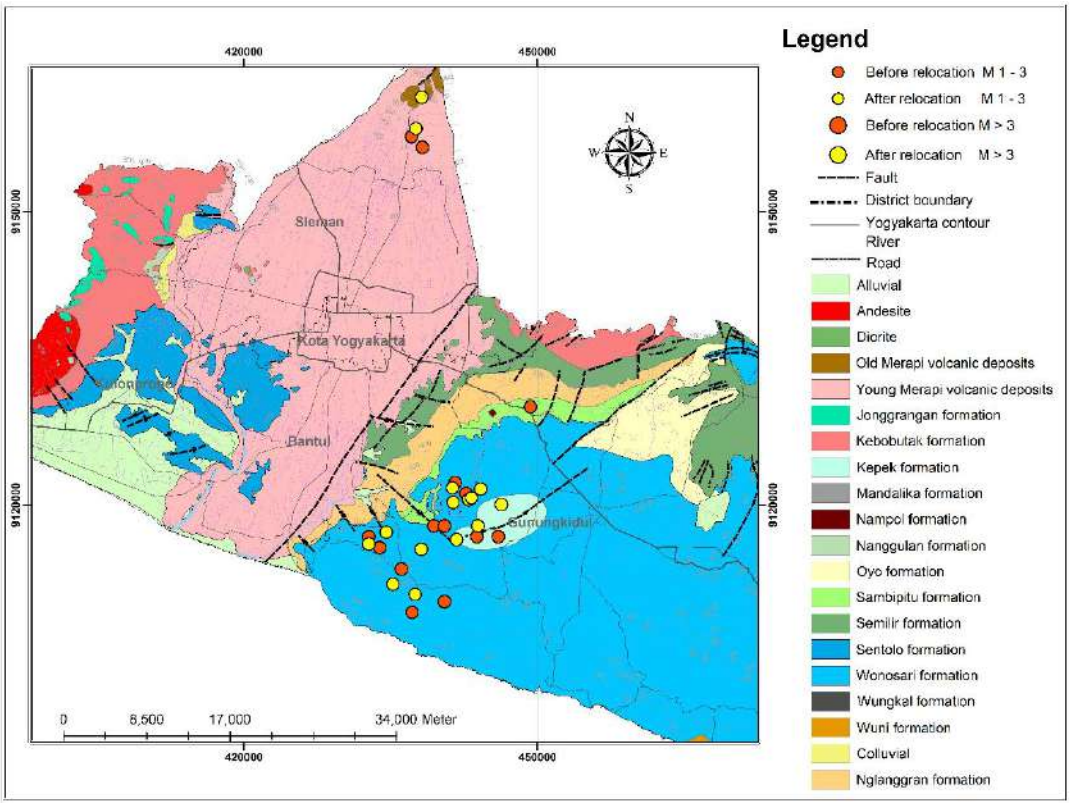

Figure 5. Distribution of land area epicenters before and after relocation (modification from Wartono et al., 1977).

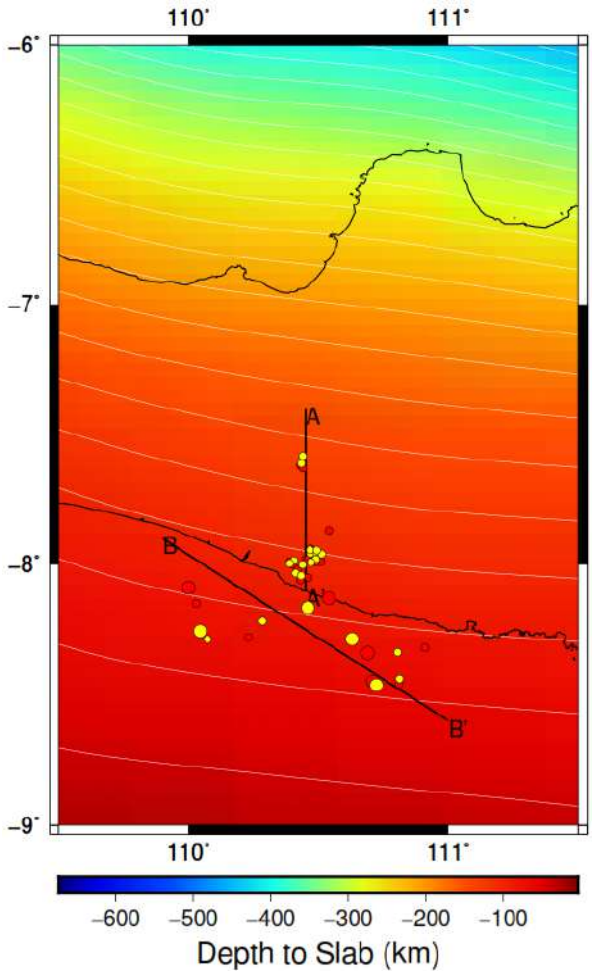

Figure 6. Distribution of earthquake hypocentres before and after relocation, line A-A' on land and line B-B' on sea.

Figure 7 & 8 shows the distribution of earthquakes before and after relocation for earthquakes that occur in marine areas with cross section B-B'. On the B-B' line with a depth 60 to 125 km indicates an earthquake that has shifted in the direction of subduction (red line). On the B-B' line with a depth of less than 20 km, 2 shallow earthquake events in the ocean with small shifts are shown. Shallow earthquakes in the marine area are expected because active faults are present under the sea.

Figure 9 is a compass diagram of earthquake relocation showing the direction and distance of earthquake displacement. The diagram shows that the earthquake shifted in all directions with a distance less than 20 km. Figure 9 shows that the most distant earthquake shifted 19.0644 km from 0^o to the southeast, where 0^o is the north direction according to the compass. Figure 10 is a rose diagram of earthquakes relocation results, showing the number of earthquakes and the shift angle. From the diagram, earthquake displacement after relocation has shifted in all direction with the smallest azimuth of $4{,}729^o$ to the largest azimuth of $359{,}4892^o$. However, there are some earthquakes that tend to a particular direction, and that is toward the northeast and northwest. The result of the shift can be influenced by the location of the stations around the study area.

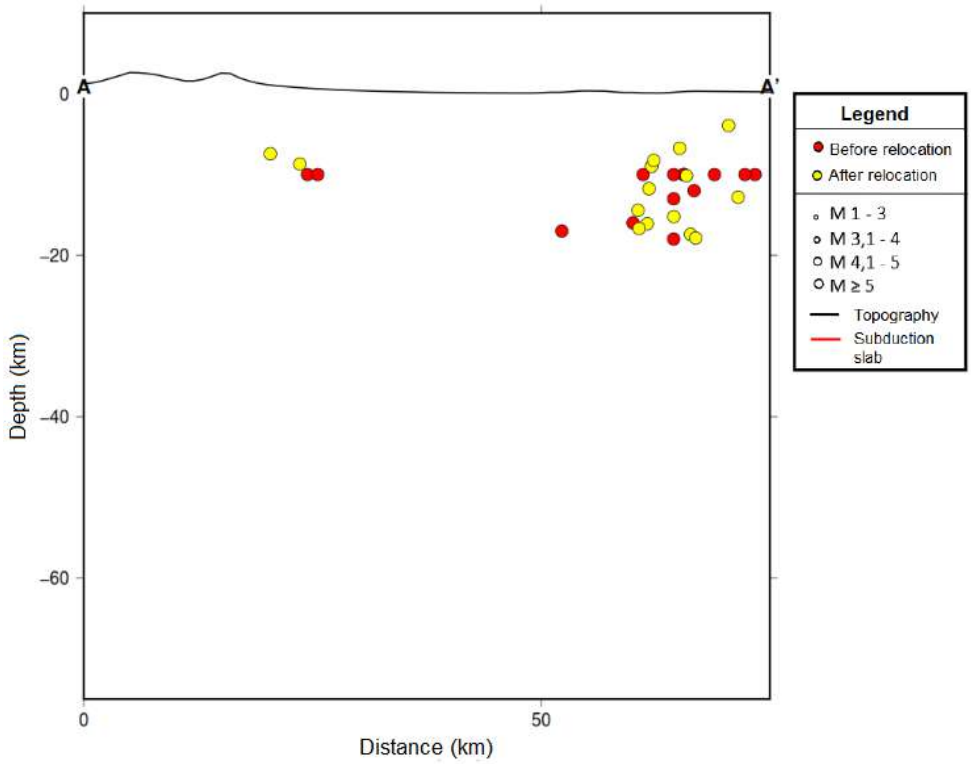

Figure 7. Distribution of hypocentre depths in the land area (line A-A' is virtually the same as line A-A' in figure 5).

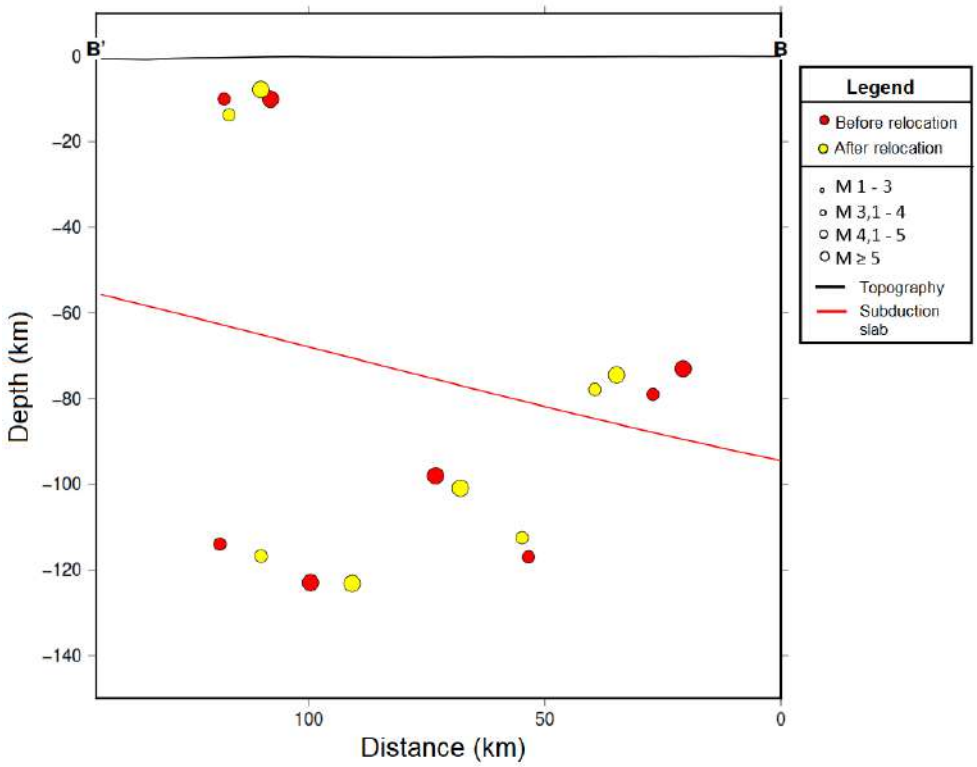

Figure 8. Distribution of hypocentre depths in the sea area (line B-B' is virtually the same as line B-B' in figure 5).

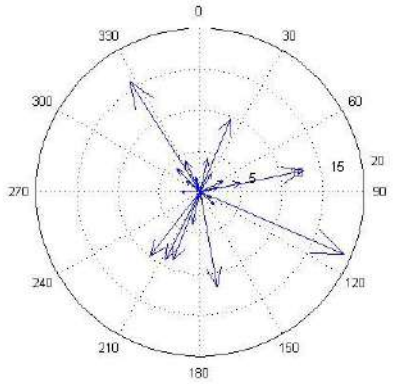

Figure 9. Compass diagram show the distance and direction hypocentre shift after relocation.

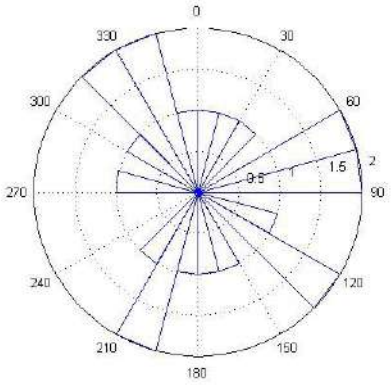

Figure 10. Rose diagram show the number and angle hypocentre shift after relocation.

Conclusion

The hypocentre relocation results can relocate the entire earthquake data by generating a residual value close to zero, which indicates position of hypocentre after relocation close to the actual position. Based on the relocation result, the source of earthquake can be analysed, i.e., the earthquakes on land caused by faults and the earthquakes in the ocean caused by subduction. The relocation results show that the source of the land earthquake in the Wonosari area is under the Wungkal Formation, while the land earthquake in the Merapi area was probably caused by a tectonic volcanic earthquake. The hypocentre of the earthquake has shifted after relocation in all directions and less than 20 km, dominated by the direction to the northeast and northwest.

Acknowledgments

We would like to thank BMKG Yogyakarta and UIN Sunan Kalijaga Yogyakarta for giving us the opportunity to conduct this research.

Author Contribution

Fani Rohmiasih: Conceptualization, Investigation, Visualization, Writing-original draft, Formal analysis. Andi: Investigation, Visualization, Writing-review & editing, Formal analysis, Validation. Nugroho Budi Wibowo: Investigation, Formal analysis, Writing-review & editing, Validation.

Conflict of Interest

The authors declare no conflict of interest.

References

Diaz, N., Suarbawa, K. N., & Mursitantyo, A. (2018). Relokasi Gempabumi di Pulau Bali Bagian Utara Tahun 2015-2017 dengan menggunakan Metode Double Difference (DD). *Buletin Fisika*, 19(2), 64–72. https://ojs.unud.ac.id/index.php/buletinfisika/article/view/43518

Fathani, T. F., & Wilopo, W. (2017). Seismic microzonation studies considering local site effects for yogyakarta city, indonesia. *International Journal of GEOMATE*, 12(32), 152–160. http://dx.doi.org/10.21660/2017.32.63655

Harlianti, U., Nugraha, A. D., & Indrastuti, N. (2017). Relocation of volcano-tectonic earthquake hypocenter at Mt. Sinabung using double difference method. *AIP Conference Proceedings*, 1857(070004), 1-6. https://doi.org/10.1063/1.4987092

Kusmita, T., Pribadi, I., MZ, N., & Rohadi, S. (2020). Studi Awal Seismotektonik di Wilayah Jawa Barat Berdasarkan Relokasi Hiposenter Metode Double

Difference. *Jurnal Geosaintek*, 6(1), 43–50. http://dx.doi.org/10.12962/j25023659.v6i1.6697

Nurbaiti, Y., Ibrahim, E., Hasanah, M. U., & Wijatmoko, B. (2019). Application of double-difference method for relocating aftershocks hypocenters in Opak Fault Zone. *IOP Conference Series: Earth and Environmental Science*, 311(012028) 1-6. https://iopscience.iop.org/article/10.1088/1755-1315/311/1/012028

Puspita C., Nugraha, A. D., & Puspito, N. T. (2015). Earthquake hypocenter relocation using double difference method in East Java and surrounding areas. *AIP Conference Proceedings*, 1658(030021), 1–3. https://doi.org/10.1063/1.4915029

Qodri, M. F., & Sopamena. R. A. (2022). Mineralogical and geochemical characterization of the Wonosari formation limestone at Gunungkidul Indonesia as preliminary investigation of Portland cement raw material. IOP *Conference Series: Earth and Environmental Science*, 1151(012026), 1–9. https://iopscience.iop.org/article/10.1088/1755-1315/1151/1/012026

Ramdhan, M., Kristyawan, S., & Sembiring, A. S. (2020). Seismisitas di Wilayah Jawa Tengah dan Sekitarnya Berdasarkan Hasil Relokasi Hiposenter dari Empat Jaringan Seismik Menggunakan Model Kecepatan 3-D. *Eksplorium*, 41(1), 61–72. http://dx.doi.org/10.17146/eksploriu m.2020.41.1.5828

Sabtaji, A., & Nugraha, A. D. (2015). 1-D seismic velocity model and hypocenter relocation using double difference method around West Papua region. *AIP Conference Proceedings*, 1658(030005) 1-8. https://doi.org/10.1063/1.4915013

Setiadi, T. A. P., Rohadi, S., & Heryandoko, N. (2017). Earthquake relocation in Mollucas Sea using teleseismic double difference method for tectonic setting analysis. *AIP Conference Proceedings*, 1857(020007). 1–6. https://doi.org/10.1063/1.4987049

Setiadi, T. A. P., & Rohadi, S. (2018). Relokasi Gempa Bumi Teleseismik Double-Difference di Wilayah Bali - Nusa Tenggara dengan Model Kecepatan 3D. *Jurnal Lingkungan dan Bencana Geologi*, 9(1), 45–52. http://dx.doi.org/10.34126/jlbg.v9i1.149

Supendi, P., Nugraha, A. D., Widiyantoro, S., Abdullah, C. I., Puspito, N. T., Palgunadi, K. H., & Wiyono, S. H. (2019). Hypocenter relocation of the aftershocks of the Mw 7.5 Palu earthquake. *Geoscience Letters*, 6(1), 1–11. https://doi.org/10.1186/s40562-019-0148-9

Surono. (2009). Litostratigrafi Pegunungan Selatan Bagian Timur Daerah Istimewa Yogyakarta dan Jawa Tengah. *Geo-Sciences*, 19(3), 209–221. https://doi.org/10.33332/jgsm.geologi.v19i3.206

Syafriani., Raharjo, F. D., Ahadi, S., & Ramdhan, M. (2023). Study of Seismicity Based on the Results of Hypocenter Relocation Using Double Difference (HypoDD) Method in West Sumatera and Its Surrounding. *Jurnal Penelitian Pendidikan IPA*, 9(7), 5150–5156. https://doi.org/10.29303/jppipa.v9i7.3792

Utama, M. R. J., Nugraha, A. D., & Puspito, N. T. (2015). Seismicity studies at Moluccas area based on the result of hypocenter relocation using HypoDD. *AIP Conference Proceedings*, 1658(030022) 1-4. https://doi.org/10.1063/1.4915030

Waldhauser, F. (2001). hypoDD -- A Program to Compute Double-Difference Hypocentre Locations.

Menlo Park, U.S Geol. Survey. https://doi.org/10.3133/ofr01113

Waldhauser, F. & Ellsworth, W. L. (2000). A double difference earthquake location algorithm: Method and application to the northern Hayward fault, California. *Bulletin Seismological Society of America*, 90(6), 1353–1368. https://doi.org/10.1785/0120000006

Wartono, R., Sukandarrumidi., & H. M. D. Rosidi (1977). *Peta Geologi Lembar Yogyakarta*. Pusat Penelitian dan Pengembangan Geologi.

Wibowo, N. B., dan Sembri, J. N. (2017). Analisis Seismisitas dan Energi Gempabumi di Kawasan Jalur Sesar Opak-Oyo Yogyakarta. *Jurnal Sains Dasar*, 6(2), 109–115. https://journal.uny.ac.id/index.php/jsd/article/view/15544

Yulianto, Y., Nugraha, A. D., & Wiyono, W. S. (2017). Hypocenters relocation using double-difference method around Molucca Collision Zone. *AIP Conference Proceedings*, 1857(020002), 1–4. https://doi.org/10.1063/1.4987044

ISSN: 2579-5821 (Print)
ISSN: 2579-5546 (Online)
URL address: http://journal.unhas.ac.id/index.php/geocelebes
DOI: 10.20956/geocelebes.v7i2.25258

Jurnal Geocelebes Vol. 7 No. 2, October 2023, 186 – 193

Potential of Limestone as a Groundwater Reservoir based on Porosity Analysis in the Tintingon Area, Banggai District

Nurhikmah Supardi[1]*, Syarifullah Bundang[2], Meltini Pakiding[1]

[1]Geological Engineering Study Program, Tadulako University, 94148, Indonesia.
[2]Mining Engineering Study Program, Khairun University, 97719, Indonesia.

*Corresponding author. Email: nurhikmah.supardi90@gmail.com

Manuscript received: 30 January 2023; Received in revised form: 2 October 2023; Accepted: 11 October 2023

Abstract

The research area is in Tintingon Village, Banggai Regency, Central Sulawesi Province. This study aims to determine the quality of limestone as a groundwater reservoir based on porosity analysis. This study begins with sampling limestone at seven stations, then selecting fresh samples for laboratory analysis. Laboratory analysis consists of two, namely petrographic analysis and porosity analysis. The petrographic analysis aims to determine the microscopic naming of limestone and the type of pores in the rock. Porosity analysis aims to test the ability of limestone to accommodate fluids as a groundwater reservoir. Based on the petrographic analysis, it is known that the microscopic naming of limestone in the study area is wackestone and packstone. The types of limestone porosity are vug, intercrystal, channel and interparticle. Analysis of limestone porosity in the study area is known to be 15.24 – 29.95%. The porosity value is categorized as good to excellent so the research area is very good as a groundwater reservoir rock.

Keywords: groundwater; limestone; porosity; reservoir; Tintingon.

Citation: Supardi, N., Bundang, S., & Pakiding, M. (2023). Potential of Limestone as a Groundwater Reservoir based on Porosity Analysis in the Tintingon Area, Banggai District. *Jurnal Geocelebes* 7(2):186–193, doi: 10.20956/geocelebes.v7i2.25258

Introduction

Limestone is a sedimentary rock composed mostly calcium carbonate ($CaCO_3$) (Ali & Ahmed, 2019; Santika & Mulyadi, 2017). These rocks come from the remains of marine organisms (Aryaseta et al., 2022). Limestone aquifer lithology formations have flow media characteristics in the form of pores, fractures, and dissolution passages, so they have the potential to drain groundwater at high speeds (Febriarta et al., 2020).

One that affects the availability of groundwater in limestone areas is the presence of pores in the rock. Porosity is a measure of the volume in the rock available to accommodate the reservoir fluids. Therefore, the volume of oil, gas and water in each reservoir depends directly on the porosity (Oyeneyin, 2015). However, carbonate reservoirs are generally characterized by strong heterogeneity, making the exploitation and prediction of prolific reservoirs difficult (Makhloufi et al., 2013; Matonti et al., 2015; Corbett et al., 2017). The heterogeneity of carbonate reservoirs is closely related to their pore morphology and pore connectivity. However, these properties are difficult to determine (He et al., 2016).

Limestone can be used for various needs, both industrial and household needs (Okto et al., 2021). Several studies on limestone have been conducted on Sulawesi Island, including Nurwaskito et al. (2015) who examined the quality of limestone as the main raw material for Portland Cement in South Sulawesi. Permana (2018) examined the quality of limestone as an industrial

mineral in Gorontalo. Yoanita et al. (2016) conducted research in Central Sulawesi on the study of gypsum synthesis from limestone and research on limestone as a raw material for cement in Gorontalo conducted by Eksan et al. (2019). All of researchers jointly studied the benefits of limestone in the industrial sector. The potential of limestone is not only from an industrial perspective but also from an environmental sustainability perspective as a groundwater reservoir reserve.

Research on the quality of limestone as a groundwater reservoir on the island of Sulawesi, especially in the city of Gorontalo, has been carried out by experts. The results showed that the potential of limestone in the city of Gorontalo as a groundwater reservoir is in the very good category with a porosity of 20–25% (Permana & Eraku, 2020). According to Munawir et al. (2019) who conducted research on aquifer analysis in limestone based on secondary porosity in Lam Kabeu – Pidie, concluded that the porosity value in the area is between 5–45%. Limestone that has not been classified will have a smaller porosity value between 0–10%. Another study conducted by Wiloso & Ratmy (2018), concluded that limestone at the research location with a porosity value of 22.23% could be an excellent aquifer.

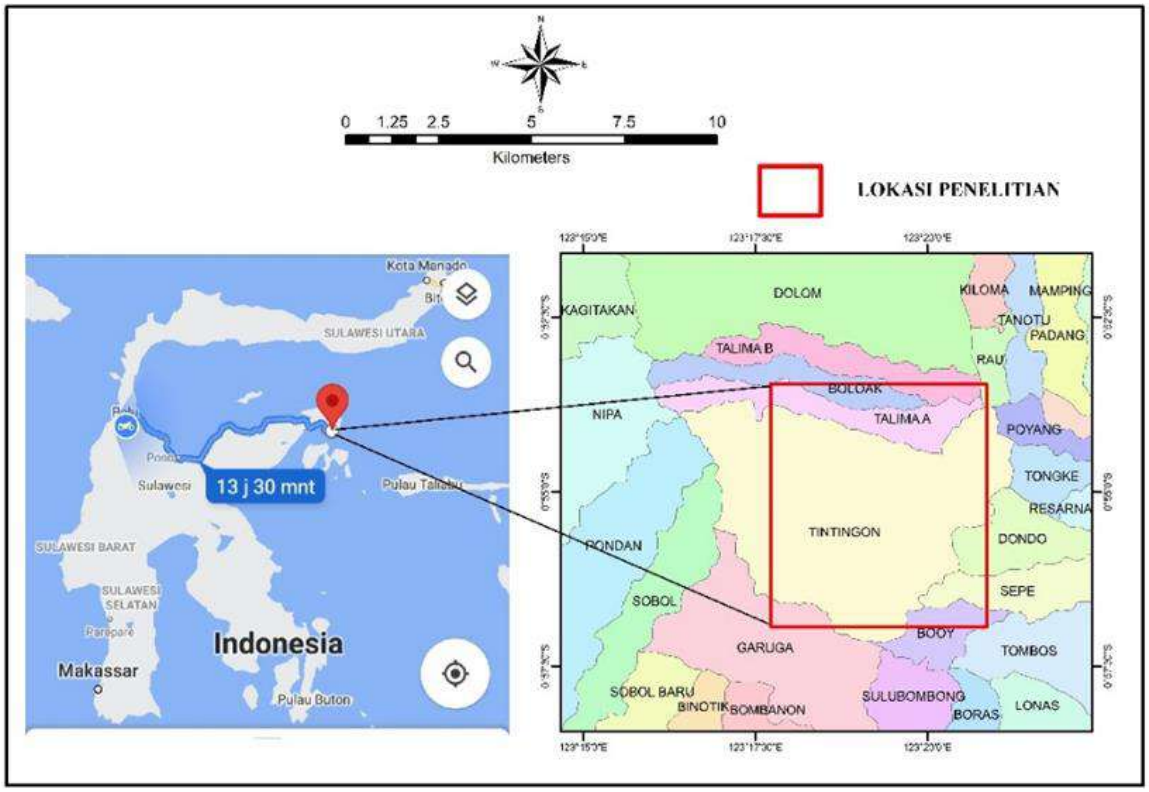

Figure 1. Location of the research area (the red box).

Limestone in Central Sulawesi has not been properly utilized (Yoanita et al., 2016). Research on the quality of limestone as a groundwater reservoir in Central Sulawesi has never been carried out, especially in the Tintingon area, Balantak Selatan District, Banggai Regency (Figure 1). The limestone in this area is close to community settlements and is one of the reasons research projects for the availability of groundwater reservoirs needs to be carried out. This is to support the need for clean water as a basic need for the local community. The purpose of this study was to determine the potential of limestone as a groundwater reservoir based on porosity analysis. The Tintingon area is included in the Salodik Formation based on the

geological map of the Luwuk sheet. The Salodik Formation consists of sandy limestone, marl, sandstone, and chert (Rusmana et al., 1993). Especially in the Tintingon area, it is composed of limestone lithology.

Research Methods

This research requires tools and materials used in the field and the laboratory. Tools and materials in the field include a geological hammer, geological compass, GPS, roll meter, and sample bag. Tools and materials in the laboratory include polarizing microscopes, digital balances, microwaves, desiccators, and rock samples. This research consists of three stages. The first stage is data collection. Data collection was in the form of stratigraphic measurements on representative limestone outcrops. The measurement path starts from the bottom to the top of the outcrop, by measuring the thickness of each layer found. Based on the measured stratigraphic measurements, the overall thickness of the outcrop was 194.66 meters, which was dominated by calcarenite limestone (Figure 2). Rock samples were taken from fresh rock outcrops for further analysis in the laboratory.

Figure 2. The appearance of calcarenite limestone outcrops with the direction of photo N120^{0}E.

The second stage is laboratory analysis. Laboratory analysis consists of two, which are petrographic analysis and porosity analysis. The petrographic analysis aims to determine the microscopic characteristics of the limestone and the pore types in the rock. Petrographic analysis was initiated by making thin sections on 7 rock samples taken from 7 field observation stations with a size of 0.03 mm.

Porosity analysis was carried out on 7 rock samples taken from 7 field observation stations to test the ability of limestone to hold liquid as a groundwater reservoir. Porosity analysis in this study was carried out by measuring in the laboratory. This test begins with preparing a limestone sample which is cut in the shape of a 5x5x5 cm cube. The sample that has been cut is then recorded as the original sample weight value (Wn). After the limestone samples

have been weighed, the samples are dried in an oven with a temperature of 800-1000^{0}C for 24 hours, the samples are then cooled in a cooler (desiccator), and each sample is weighed again as a dry sample weight (Wo) and record the value. After weighing the dry sample, the limestone is put into a container filled with water and soaked for 24 hours. After soaking the sample for 24 hours, the sample is weighed and its value is recorded as the saturated sample weight (Ww). After obtaining the saturated sample weight value, pull the rope tied to the sample until the sample position is suspended in the water and record the value as the dependent saturated weight (Ws).

The third stage is data processing and interpretation. This stage includes determining the pore type of rock in thin sections and calculating the porosity of the rock. One of the geologists who classify the pore types of carbonate rocks is Choquette & Pray (1970) (Figure 3). This classification relates the pore size, shape, and packing of the rock.

$$Porosity\ (\%) = \frac{Ww-Wo}{Ww-Ws} x\ 100\% \quad (1)$$

Calculation of rock porosity using equation (1). Where Ww is the weight of the saturated sample after being saturated for 24 hours (grams), Wo is the weight of the dry sample after being baked for 24 hours (grams) and Ws is the weight of the saturated sample depending on water (grams). The results of the porosity calculation are equated with the qualitative classification (Table 1) proposed by Todd (1980).

Table 1. Classification of porosity scale values (Todd, 1980).

Score (%)	Porosity
1 – 10	Large porosity
10 – 20	Medium porosity
20 – 30	Small porosity

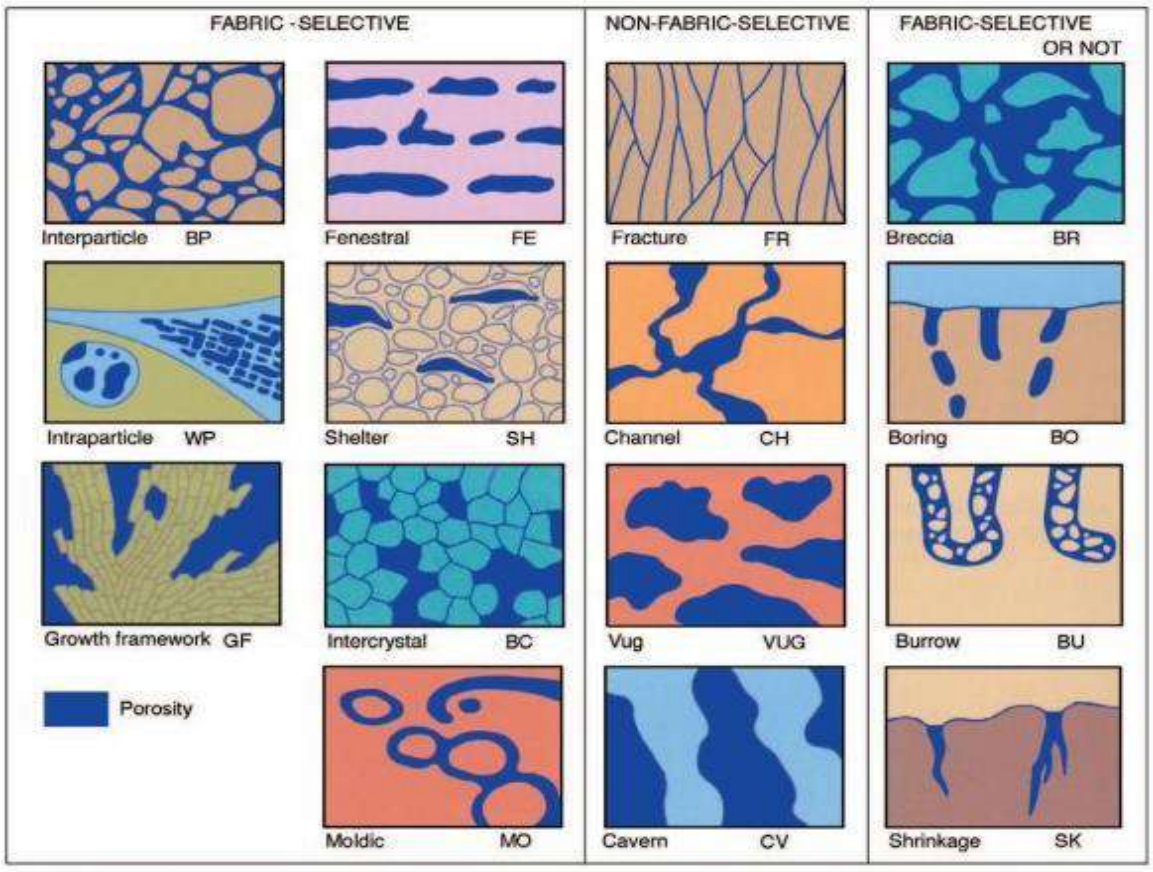

Figure 3. Types of pores in carbonate rocks (Choquette and Pray, 1970).

Results and Discussion

The results and discussion include a description of the lithology and pore types at each station as well as the results of the porosity calculation.

The first station has a fresh white color, gray weathered color, fine to medium grain size (¼-½ mm) with a layer thickness of ±27.75 meters, the grains are circular to very round, there is bioclase in the form of clam shells. Based on thin sections, the rock at this station is packstone (Dunham, 1962) with a pore type, vug (Figure 4.a).

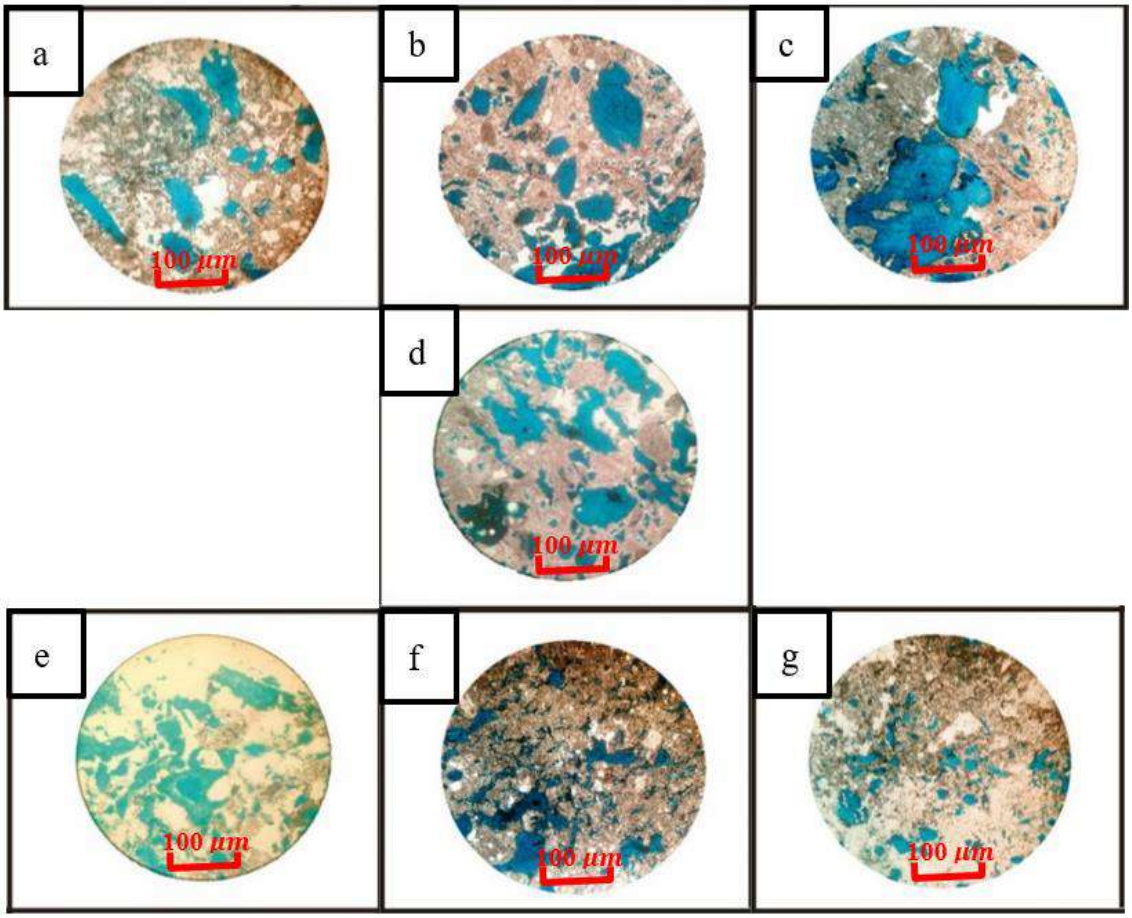

Figure 4. Lithology and pore type of samples in the study area.

The second station has a fresh white color, weathered blackish-gray color, medium to coarse grain size (½-1 mm) with a layer thickness of ±14.70 meters, the grains are semi-round to very round, there are bioclase in the form of shells and fossils macro. Based on thin sections, the rock at this station is wackestone (Dunham, 1962) with a pore type, which is vug (Figure 4.b).

The third station has a fresh grayish-white color, black weathered color, medium to coarse grain size (½-1 mm) with a layer thickness of ±48 meters, granules are half-round to very round, there is bioclase in the form of shells. Based on thin sections, the rock at this station is wackestone (Dunham, 1962) with a pore type in the form of a channel (Figure 4.c).

The fourth station has a fresh white color, grayish-black weathered color, fine to coarse grain size (¼-1 mm) with a layer thickness of ±33.21 meters, the grains are semi-round to very round, there is bioclase in the form of macro fossil shells. Based on

thin sections, the rock at this station is wackestone (Dunham, 1962) with a vug pore type (Figure 4.d).

The fifth station has a fresh grayish-white color, weathered gray color, fine to coarse grain size (¼-1 mm) with a layer thickness of ±40.10 meters, granules in the shape of a semi-round to very round shape, there are bioclase in the form of macro fossil shells. Based on thin sections, the rock at this station is wackestone (Dunham, 1962) with a vug pore type (Figure 4.e).

The sixth station has a fresh white color, black weathered color, medium to coarse grain size (½-1 mm) with a layer thickness of ±10 meters, the grains are half-round to very round, there is bioclase in the form of macro-fossil shells. Based on thin sections, the rock at this station is wackestone (Dunham, 1962) with interparticle pore types (Figure 4.f).

The seventh station has a fresh grayish-white color, black weathered color, very fine to fine grain size (1/8-¼mm) with a layer thickness of ±20.90 meters, the grains are in the shape of a semi-round to very round shape. Based on thin sections, the rock at this station is packstone (Dunham, 1962) with an intercrystal pore type (Figure 4.g).

Porosity testing and calculations were carried out on 7 limestone samples from each station. Porosity calculation using equation (1).

Based on the calculation results, the porosity value for each limestone sample is obtained as outlined in Table 2.

Table 2. The results of the porosity calculation are compared with the classification (Todd, 1980).

Station	Parameters Test			Porosity (%)	Todd Classification (1980)
	Wo (gr)	Ww (gr)	Ws (gr)		
1.	295.1	313.9	222.7	20.61	large porosity
2.	320.9	348.7	222.8	22.08	large porosity
3.	387.3	412.0	294.3	20.99	large porosity
4.	233.0	259.3	171.5	29.95	large porosity
5.	248.9	272.2	175.1	24	large porosity
6.	185.8	204.5	116.5	21.25	large porosity
7.	266.0	280.9	183.1	15.24	medium porosity

The results of the porosity calculation above show that samples 1, 2, 3, 5 and 6 have very good porosity. Sample 4 has special porosity and sample 7 has good porosity. The porosity value of the limestone in the study area is 15.24 – 29.95%. Based on this, the limestone in the study area is very good as a groundwater reservoir rock where the greater the porosity of the rock, the greater the amount of water that can be stored in the rock. The presence of water or fluid in the reservoir rock is inseparable from the source rock.

Calculation of the porosity of the limestone in the study area shows the same value as the porosity of the limestone in the city of Gorontalo, which is in the very good category with a porosity of 20–25% (Permana & Eraku, 2020).

Conclusion

Based on the results of laboratory analysis, it can be concluded that the lithology of the limestone in the study area is wackestone and packstone with vug, channel, interparticle and intercrystal pore types. Limestone porosity is 15.24 – 29.95%. The porosity value is in the medium to large category so that the research area is very good as a groundwater reservoir rock.

Acknowledgements

We would like to thank our fellow lecturers in Geological Engineering at Tadulako

University who have provided input so that this research can be completed.

Author Contribution

This paper was completed thanks to the collaboration of all the authors. The idea on this topic was first proposed by Nurhikmah Supardi. Most of the data analysis was done by Nurhikmah Supardi. Meltini Pakiding was in charge as completing laboratory testing and Syarifullah Bundang helped arrange the background and some editing. Hopefully this kind of collaboration will continue.

Conflict of Interest

This research was conducted independently without any financial support from any parties.

References

Ali, M. A. M., & Ahmed, H. M. (2019). Engineering Characteristics of Egyptian Limestone. *Mining of Mineral Deposits*, 13(2), 75–81. https://doi.org/10.33271/mining13.02.075

Aryaseta, B., Wardhani, P. C., & Zainab, S. (2022). Studi Eksperimental Sifat Fisik dan Mekanik Batu Gamping. *KERN: Jurnal Ilmiah Teknik Sipil*, 8(1), 37–42.

Choquette, P. W. & Pray, L. C. (1970). Geologic Nomenclature and Classification of Porosity in Sedimentary Carbonates. *American Association of Petroleum Geologists Bulletin*, 54, 207–250. https://doi.org/10.1306/5D25C98B-16C1-11D7-8645000102C1865D

Corbett, P. W. M., Wang, H., Câmara, R. N., Tavares, A. C., de Almeida, L. F. B., Perosi, F., Machado, A., Jiang, Z., Ma, J., & Bagueira, R. (2017). Using The Porosity Exponent (M) and Pore-Scale Resistivity Modelling to Understand Pore Fabric Types in Coquinas (Barremian-Aptian) of The Morro Do Chaves Formation, NE Brazil. *Marine & Petroleum Geology*, 88, 628–647. https://doi.org/10.1016/j.marpetgeo.2017.08.032

Dunham, R. J. (1962). *Classification of Carbonate Rocks According to Deposition Textures*. AAPG Memoir 1.

Eksan, D. H., Zainuri, A. & Kasim, M. (2019). Potensi Batugamping untuk Bahan Baku Industri Semen Daerah Biluhu Timur dan Sekitarnya. *Jambura Geoscience Review*, 1(2), 68–76. https://doi.org/10.34312/jgeosrev.v1i2.2380

Febriarta, E., Marfai, M. A., Hizbaron, D. R., & Larasati, A. (2020). Kajian Spasial Multi Kriteria DRASTIC Kerentanan Air Tanah Pesisir Akuifer Batugamping di Tanjungbumi Madura. *Jurnal Ilmu Lingkungan*, 18(3), 476–487. https://doi.org/10.14710/jil.18.3.476-487

He, J., Ding, W., Li, A., Sun, Y., Dai, P., Yin, S., Chen, E., & Gu, Y. (2016). Quantitative Microporosity Evaluation Using Mercury Injection and Digital Image Analysis in Tight Carbonate Rocks: A Case Study from The Ordovician in The Tazhong Palaeouplift, Tarim Basin, NW China. *Journal of Natural Gas Science and Engineering*, 34, 627–644. https://doi.org/10.1016/j.jngse.2016.07.025

Makhloufi, Y., Collin, P-Y., Bergerat, F., Casteleyn, L., Claes, S., David, C., Menendez, B., Monna, F., Robion, P., Sizun, J-P., Swennen, R., & Rigollet, C. (2013). Impact Of Sedimentology and Diagenesis on The Petrophysical Properties of a Tight Oolitic Carbonate Reservoir. The Case of The Oolithe Blanche Formation (Bathonian, Paris Basin, France). *Marine & Petroleum Geology*, 48, 323–340.

https://doi.org/10.1016/j.marpetgeo.2013.08.021

Matonti, C., Guglielmi, Y., Viseur, S., Bruna, P. O., Borgomano, J., Dahl, C., & Marié, L. (2015). Heterogeneities and Diagenetic Control on The Spatial Distribution of Carbonate Rocks Acoustic Properties at The Outcrop Scale. *Tectonophysics*, 638, 94–111. https://doi.org/10.1016/j.tecto.2014.10.020

Munawir, A., Jauhari, A., Kurniawan, M. O., & Muhammad, A. N. (2019). Analisis Akuifer Anggota Batugamping Lam Kabeu – Pidie dengan Metode Porositas Sekunder. *Prosiding Pendidikan Geografi FKIP UMP*, 289–300. https://digitallibrary.ump.ac.id/463/

Nurwaskito, A., Amril, F., & Widodo, S. (2015). Analisis Kualitas Batugamping sebagai Bahan Baku Utama Semen Portland pada PT. Semen Tonasa Provinsi Sulawesi Selatan. *Jurnal Geomine*, 2(1), 117–123. https://doi.org/10.33536/jg.v2i1.33

Okto, A., Masri, M., Mili, M. Z., & Hasria, H. (2021). Karakteristik Batugamping Formasi Wapulaka dan Pemanfaatannya sebagai Bahan Galian Industri di Desa Wuna, Kabupaten Muna Sulawesi Tenggara. *Jurnal Mineral, Energi dan Lingkungan*, 5 (1), 11–17. https://doi.org/10.31315/jmel.v5i1.4030

Oyeneyin, B. (2015). Fundamental Principles of Management of Reservoirs with Sanding Problems. *Developments in Petroleum Science*, 63, 129–138. https://doi.org/10.1016/B978-0-444-62637-0.00003-8

Permana, A. P. (2018). Potensi batugamping terumbu gorontalo sebagai bahan galian industri berdasarkan analisis geokimia XRF. *Enviroscienteae*, 14 (3), 2302–3708. http://dx.doi.org/10.20527/es.v14i3.5688

Permana, A. P., & Eraku, S. S. (2020). Kualitas batugamping Gorontalo sebagai reservoir air tanah berdasarkan analisis jenis porositas. *EnviroScienteae*, 16(1), 1–6. http://dx.doi.org/10.20527/es.v16i1.8993

Rusmana, E., Koswara, A. & Simandjuntak, T. O. (1993). *Peta Geologi Lembar Luwuk. Pusat Penelitian dan Pengembangan Geologi*. Bandung.

Santika, A. W., & Mulyadi, D. (2017). Geokimia Batugamping Daerah Montong, Tuban, Jawa Timur. *Riset Geologi dan Pertambangan*, 27(2), 227–238. https://jrisetgeotam.lipi.go.id/index.php/jrisgeotam/article/view/493

Todd, D. K. (1980). *Groundwater Hydrology*. New York. John Wiley and Sons.

Wiloso, D. A., & Ratmy (2018). Analisis Porositas Batugamping Sebagai Akuifer di Desa Ponjong, Kecamatan Ponjong Kabupaten Gunungkidul, Daerah Istimewa Yogyakarta. *Jurnal Teknologi*, 11(2), 125–132.

Yoanita, G., Mappiratu., & Prismawiryanti. (2016). Kajian sintesis gipsum dari batugamping asal Sulawesi Tengah. *Jurnal Riset Kimia Kovalen*, 2(1), 39–47. http://jurnal.untad.ac.id/jurnal/index.php/kovalen/article/view/6044

ISSN: 2579-5821 (Print)
ISSN: 2579-5546 (Online)
URL address: http://journal.unhas.ac.id/index.php/geocelebes
DOI: 10.20956/geocelebes.v7i2.23930

Jurnal Geocelebes Vol. 7 No. 2, October 2023, 194 – 203

Presentation of Green Open Space of Makassar City in WebGIS

Samsu Arif, Aswar Syafnur*, A. Muh. Imran Ismail, Aza Azzahra, Wikal

Geophysics Department, Hasanuddin University, Makassar, 90245, Indonesia

Email: aswar.syafnur@unhas.ac.id

Manuscript received: 9 November 2022; Received in revised form: 24 September 2023; Accepted: 31 October 2023

Abstract

Green open space has three basic functions, among others, to function socially, namely as a facility for the public with the functions of recreation, education and sports, as well as establishing communication between city residents; to function physically, namely as the lungs of the city, protecting the water system, soundproofing, fulfilling visual needs, restraining the development of built-up land/as a buffer, and protecting city residents from air pollution; and functions as an aesthetic that is a binder between building elements in the city, a giver of characteristics in shaping the face of the city, and an element in the arrangement of urban architecture. Law No. 26 of 2007 concerning Spatial Planning, it is explained that the spatial planning of the city area must include a plan for the provision and utilization of green open space which covers at least 30% of the city area consisting of 20% public green open space and 10% consisting of private green open space. . But in reality, there are still many big cities that are not difficult to achieve the provisions of the law. This research will identify green open space in Makassar City by utilizing satellite image data and then presenting the green open space in the form of spatial information into a Web GIS so that it can be easily accessed openly. Based on the results of the analysis, the percentage of open green space in Makassar reached 9.08%, consisting of private green open space of 4.07% and public green open space of 5.01%.

Keywords: Green Open Space; Makassar; WebGIS.

Citation: Arif, S., Syafnur, A., Ismail, A. M. I., Azzahra, A., & Wikal. (2023). Presentation of Green Open Space of Makassar City in WebGIS. *Jurnal Geocelebes*, 7(2):194–203, doi: 10.20956/geocelebes.v7i2.23930

Introduction

Makassar as the capital of South Sulawesi Province, which is also seen as the gateway to Eastern Indonesia, is iconic of the infrastructure development that continues to be carried out to support the activities of its people. In the context of Green Open Space, infrastructure development in Makassar City is not in line with the amount of provision of Green Open Space areas. Infrastructure development plays a role in cutting Green Open Space which results in a decrease in the efficiency of space and land use and the quality of life in the area (Samsudi, 2010). The reduction of green open space in urban areas causes emotional, dimensional, and psychological instability so that people's space for activities and thinking is limited (Zulkarnaen et al., 2016).

The total population in 2020 in urban areas has a percentage of 56.7% and will increase in 2035 to 66.6% (Sinatra et al., 2022). This increase in population causes the need for space to increase. The increasing need for area, especially for housing, then affects the decreasing quantity and quality of green spaces in urban areas (Dollah & Rasmawarni, 2019; Zulkarnaen et al., 2016). Therefore, the need for green spaces in urban areas must be seen quantitatively and qualitatively. Based on Permen PU No. 5/PRT/M/08 concerning Guidelines for the Provision and Utilization of Green Spaces in urban areas, the population and oxygen demand with the availability of green

spaces must be adjusted (Kurnianti & Rahmi, 2020; Devi & Santosa, 2022).

Law No. 26/2007 (BPK, 2007) on Spatial Planning explicitly mandates 30% of the city area to be Green Open Space, 20% public Green Space and 10% private Green Space. This 30% green space allocation is stipulated in the Regional Regulation (Perda) on city Spatial Planning. Spatial Planning as the spatial dimension of urban development is a tool to coordinate urban development in a sustainable manner. In line with the mandate of PR Law No. 26 of 2007 article 3 (BPK, 2007), it is necessary to realize a form of urban area development that harmonizes the natural environment and the artificial environment. Urban areas are areas that have non-agricultural main activities with an arrangement of regional functions as a place for urban settlements, concentration and distribution of government services, social services, and economic activities.

As the center of development, urban areas will attract and increase the population ratio in a region. Increased population growth will have an impact back to increased development for settlements in urban areas. The current development of urban development shows a tendency for unbalanced development activities (Yanti et al., 2023). Based on this, it is deemed necessary to identify Makassar City's green spaces and present them in WebGIS so that they can be accessed directly and openly.

Definition of Green Open Space

Open space is an elongated area in the form of a path or large area that is open or has no buildings. Green Open Space is a vegetated area, such as plants and plants located in urban areas with socio-cultural, aesthetic, and physical functions of the city (Setyani et al., 2017; Abdillah et al., 2021). The existence of green spaces is an important factor in supporting urban ecology. It also affects air comfort which is influenced by humidity and temperature as described in the thermal comfort index. A decrease in air temperature by 5.86% and an increase in humidity by 4% resulted from green spaces in good condition (Prakoso & Herdiansyah, 2019).

Function of Green Open Space

Green Open Space has two functions, which are intrinsic and extrinsic functions. Intrinsic functions consist of ecological functions, while extrinsic functions include social and cultural, economic, and aesthetic functions. In an urban area, these four main functions can be combined according to the needs, interests, and sustainability of the city such as water system protection, ecological balance, and biological conservation.

It can be concluded that basically green open space has three basic functions, including social functions, which are as a public facility with recreational, educational and sports functions, as well as establishing communication between city residents; physically functions, such as part of the air circulation or lungs of the city, protecting water systems, sound absorbers, fulfilling visual needs, regulating the microclimate so that water and air circulation can take place naturally and play a role in producing oxygen; and functions as aesthetics, such as increasing comfort, binding between building elements in the city, giving characteristics in shaping the face of the city, and elements in urban architectural arrangements (Imansari & Khadiyanta, 2015; Zubair et al., 2017).

Types of Green Open Space

Green Open Space can be in the form of urban forests, public cemetery parks, city parks, sports fields, railroad banks, green lanes, highways, and river banks (Noveri et al., 2020). Based on the explanation in the Regulation of the Minister of Public Works No. 5/PRT/M/2008, the division of existing types is in accordance with the typology that can be seen on Figure 1.

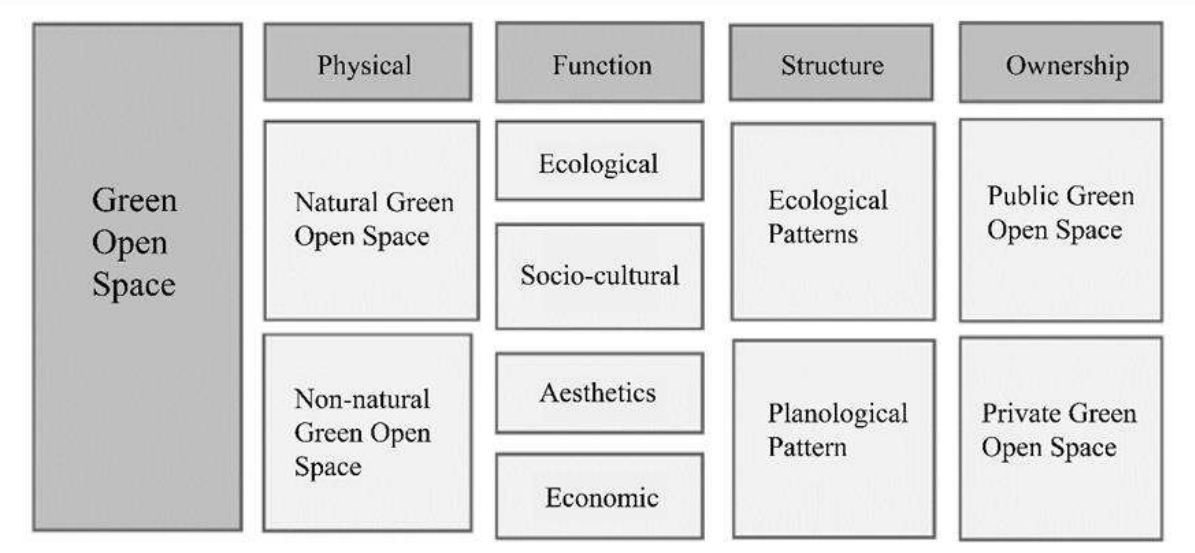

Figure 1. Typology of Green Open Space (Minister of Public Works No. 5, 2008).

In terms of ownership, Green Open Space can be in the form of Public Green Open Space and Private Green Open Space. The following is the characteristic of public and private green spaces (Table 1).

Table 1. Ownership of green space (Minister of Public Works No.5, 2008).

No.	Types	Public green space	Private green space
1	Yard green space		
	a Residential yards		v
	b Office yards, shops, and business premises		v
	c Roof gardens		v
2	Urban Park and Forest		
	a Neighborhood Park	v	v
	b RW park	v	v
	c Urban Village Park	v	v
	d Sub-district Park	v	v
	e City Park	v	
	f Urban Forest	v	
	g Green belt	v	
3	Road Green Belt		
	a Road island and road median	v	v
	b Pedestrian path	v	v
4	Specific function green space		
	a Railway green belt	v	
	b Green belt of high voltage electricity network	v	
	c Riverside green space	v	
	d Shoreline green space	v	
	e Green space for safeguarding raw water sources	v	
	f Cemetery	v	

According to the Regulation of the Minister of Public Works No. 05/PRT/M/2008 on Table 1, the determination of Green Open Space area based on population is done with the standard of Green Open Space area per capita (Manshur et al., 2020). The table listing the provision of green space based on population can be seen below (Table 2).

Table 2. Provision of green space based on population (Minister of Public Works No.5, 2008).

No.	Environmental unit	Green Space type	Minimum area /Unit (m^2)	Minimum area /Kapita (m^2)	Location
1	250 people	Household garden	250	1,0	In the middle of the neighborhood
2	2500 people	Home garden	1.250	0,5	In the center of RW activities
3	30.000 people	Neighborh ood garden	9.000	0,3	Clustered with school/district center
4	120.000 people	Sub-district park	24.000	0,2	Clustered with school/district center
5	480.000 people	Cemetery	Customized	1,2	Scattered
		City Park	144.000	0,3	In the center of the region/city
		City Forest	Customized	4,0	In/on the periphery
		For certain functions	Customized	12,5	Customized with needs

Geographic Information System

Geographic Information System (GIS) is a system that uses a computer as a base used to manipulate information or store geographically related data (Frizani et al., 2021). This system is designed to be able to analyze, capture, store, organize, and capture all types of existing geographic data. GIS can be used for spatial analysis, such as Green Open Space maps (Manshur et al., 2020; Nugrahanto et al., 2021). The development of existing technology allows GIS technology to be built based on web. WebGIS is a form of website that describes the geographic information of an area, so that it can make it easier for users to find the latest geographic information in the city (Idris & Mustofa, 2021).

Pleiades Imagery

From some of the previous descriptions, the role of green spaces in urban areas is very important, so in the evaluation and direction of Detailed Spatial Planning (Rencana Detail Tata Ruang - RDTR), accurate information is needed to see changes in green spaces that occur. In supporting the monitoring of Green Open Space area, Pleiades imagery is used which has a high spatial resolution of 0.5 meters (Mukhoriyah et al., 2019). The Pleiades high-resolution sensor loads images in panchromatic mode with a resolution of 0.7 meters resampled to 0.5 meters at ground level (LAPAN, 2007).

Research Methods

The location of this research is Makassar city with an area of 17670.31 ha. This research will identify Green Open Space by utilizing high resolution image data, Pleiades.

This research was conducted using the digitization method. Digitization was carried out on Pleiades imagery. Digitization is the process of converting raster data into vector data using GIS software, so digitization is not only limited to the process of converting analog maps into digital maps. It works by interpreting spatial objects and then converting those spatial objects into a collection of x,y coordinates with a certain type of geometry (point, line, polygon).

Results and Discussion

Research related to the presentation of Makassar City Green Open Space in

WebGIS was conducted by identifying Makassar city land cover using high-resolution images. The satellite image used is Pleiades with a resolution of 2 m multispectral and 0.5 m panchromatic (Figure 2). Interpretation to identify Green Open Space is done by analyzing Pleiades images by first identifying land cover in the Makassar city area by considering the Makassar City RTRW map and conducting a survey to the location. After identifying the land cover, then classifying the land cover which includes Green Open Space.

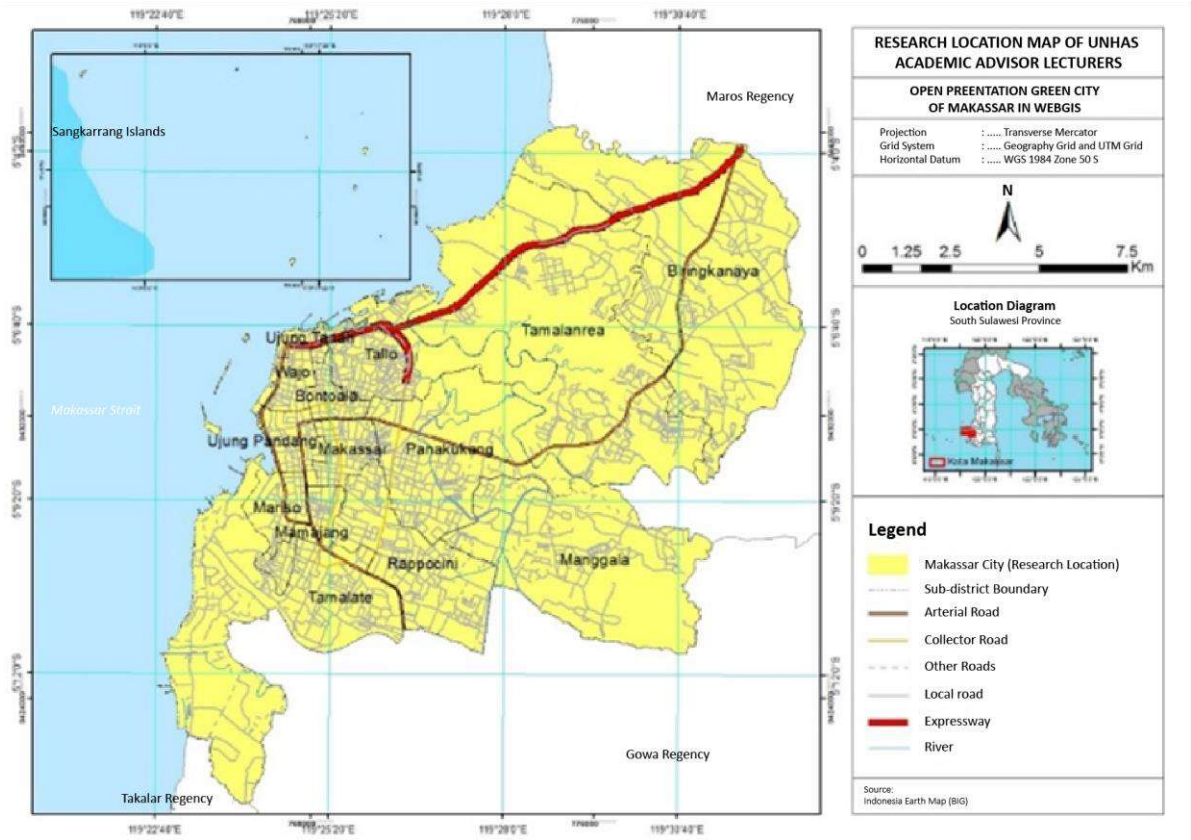

Figure 2. Makassar City Administration Map.

Identification of land cover was carried out by digitizing images using ArcGIS software. Based on the results of the Pleades image interpretation in 2021, 28 types of land cover were detected in Makassar City (Table 2), where the distribution of the area is presented in Figure 3. The land cover in question includes: lakes, docks, sports facilities, urban forests, mangrove huta, industry, roads, greenways, ponds, commercial, fields, vacant land, fields, tombs, sand, ports, settlements, education, offices, swamps, rice fields, shrubs, river borders, rivers, landfills, parks and ponds.

Based on the imagery used, almost half of Makassar City has been covered by settlements covering an area of 8393.65 Ha (47.50%), where the largest settlements are in Biringkanaya District (1747.0933 ha), Manggala (1144.7717 ha) and Tamalate covering an area of 1076.0592 (ha). Land cover in the form of settlements has the greatest influence on changes in green open space areas, so it is very important to tighten the rules to leave 30% green open space in residential areas, both in the form of thematic parks and residential parks themselves.

In addition, industry uses a large amount of land, which is 996.96 ha or about 5.64%. As a land use that can increase pollution, the industrial area must contribute land division that takes into account the

availability of green space in each industrial land.

Currently there is still a large amount of land left for land uses such as rice fields covering 2907.40 ha or 16.45%, ponds covering 1337.61 ha (7.6%) and fields covering 1360.85 ha (7.70%). However, these three types of land use always experience land conversion related to the fulfillment of needs for settlements or other public facilities, so it cannot guarantee to maintain its contribution in the provision of green spaces in the city of Makassar.

Land uses that can be maintained to contribute to the increase of Green Open Space in Makassar City are urban forest (55.77 ha), mangrove forest (55.25 ha), sports facilities (67.51 ha), field (8456 ha), cemetery (73.65 ha) and park (73.76 ha). The green belt covering an area of 52.56 ha can be improved as a green space through planting trees that have a long life with deep roots, so that the possibility of damaging the road, or falling can be avoided for a long time. The distribution of land use types is presented in Figure 3.

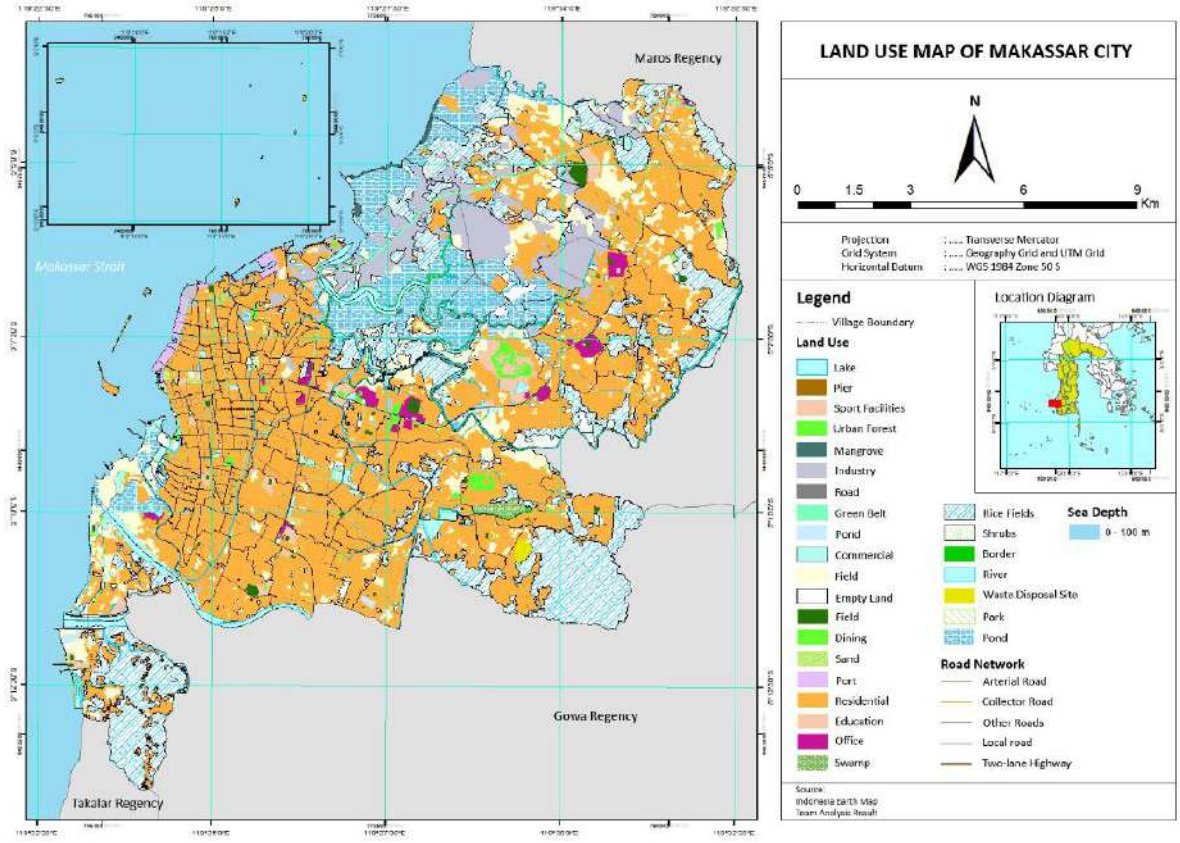

Figure 3. Makassar City Land-use Map.

One concept of providing green open space in an area is based on the area itself. In this case, the open space area must be able to meet the standard of open space area needed in a city. This open space can be in the form of public and private green spaces. According to Law No. 26 of 2007 on Spatial Planning (BPK, 2007), it is stated that each region is required to allocate at least 30% of its space or area for Green Open Space, where 20% is reserved for public Green Space which is green open space owned and managed by the city government and used for the benefit of the community in general, and 10% is reserved for private Green Space on lands owned by the private sector or the community. Public and private green spaces have several main functions such as ecological functions as well as additional functions, namely socio-cultural, economic, aesthetic/ architectural. Especially for green spaces with social

functions such as rest areas, sports facilities and or play areas, these green spaces must have good accessibility for everyone, including accessibility for people with disabilities.

Table 3. Area and Percentage of Private and Public Green Spaces in Makassar City Detailed by Sub-districts.

District	Private green space (Ha)	Public green space (Ha)	Total area (Ha)
Biringkanaya	164.052	154.273	318.325
Bontoala	2.533	9.005	11.538
Kep. Sangkarrang	0.813	4.136	4.949
Makassar	20.628	3.668	24.296
Mamajang	9.013	6.283	15.296
Manggala	198.938	70.306	269.245
Mariso	9.595	30.199	39.795
Panakukang	94.029	97.177	191.206
Rappocini	39.288	29.889	69.177
Tallo	31.481	63.137	94.617
Tamalanrea	74.207	329.302	403.509
Tamalate	46.563	59.745	106.309
Ujung Pandang	10.507	22.757	33.264
Ujung Tanah	13.520	2.394	15.914
Wajo	4.065	2.372	6.437
Green Space Total	**719.233**	**884.643**	**1603.876**
Area of Makassar City (Ha)		**17670.000**	
Percentage of Green Space (%)	**4.07**	**5.01**	**9.08**

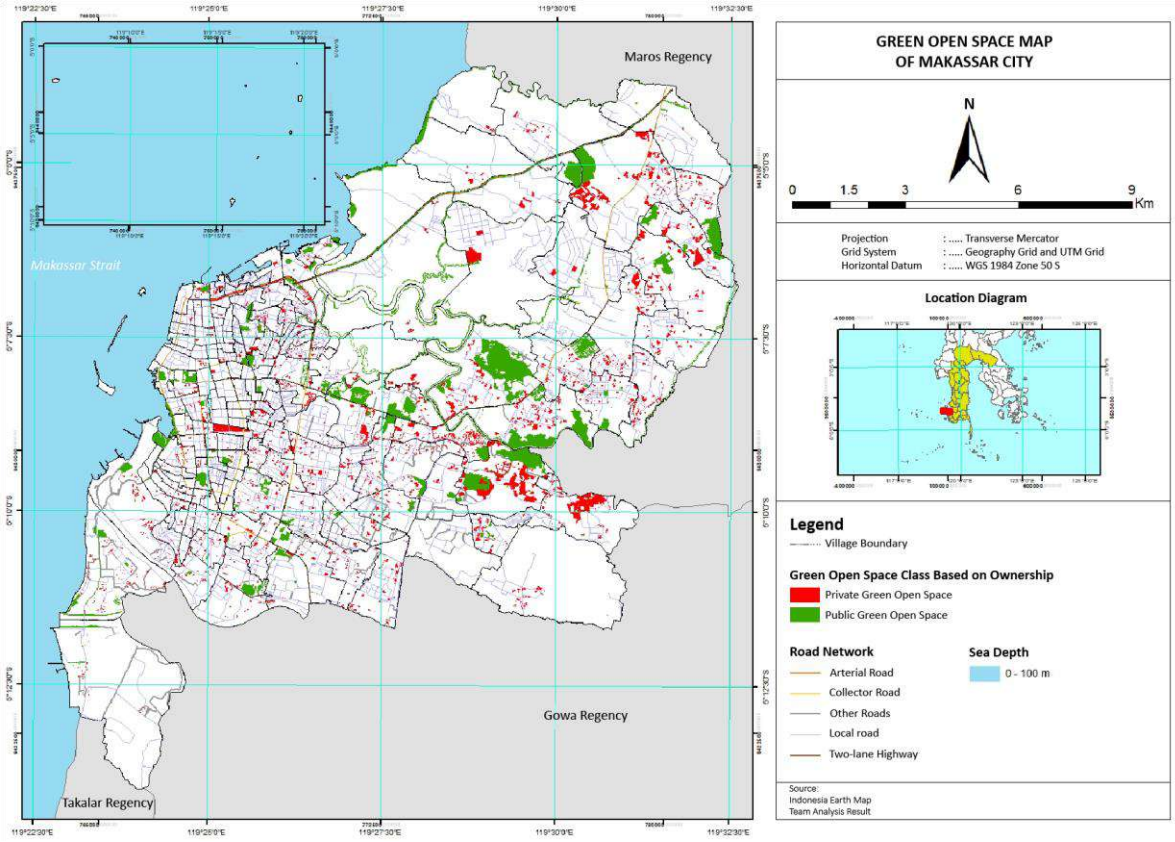

Figure 4. Map of Public and Private Green Space Distribution in Makassar City.

The area of private green spaces in Makassar City reached 719,233 ha (4.07%) and the area of public green spaces was 884,643 (5.01%). Based on this, the

percentage of green spaces in Makassar City reached 9.08% of the total area of Makassar City (Table 3). The largest private green spaces is located in four sub-districts, which are: Biringkanaya, Manggala, Panakukang, and Tamalanrea, where these four sub-districts cover the largest area among the other 15 sub-districts. The largest public green space is in Tamalanrea sub-district with an area of 329,302 ha, followed by Biringkanaya sub-district with an area of 154,273 ha and Panakukang sub-district with an area of 97,177 ha. The largest private green spaces is in Manggala sub-district with an area of 198,938, followed by Biringkanaya sub-district with an area of 164,052 ha. The four sub-districts contributed the most to the percentage of green spaces area in Makassar city. However, the sub-districts with the highest percentage of green spaces in their area are Mariso at 13.65%, Panakukang at 12.32% and Manggala at 11.76%. The distribution in each ward is presented in Table 3 and Figure 4.

The results of the above identification are then presented in a WebGIS so that they can be accessed openly, here is the WebGIS display (Figure 5):

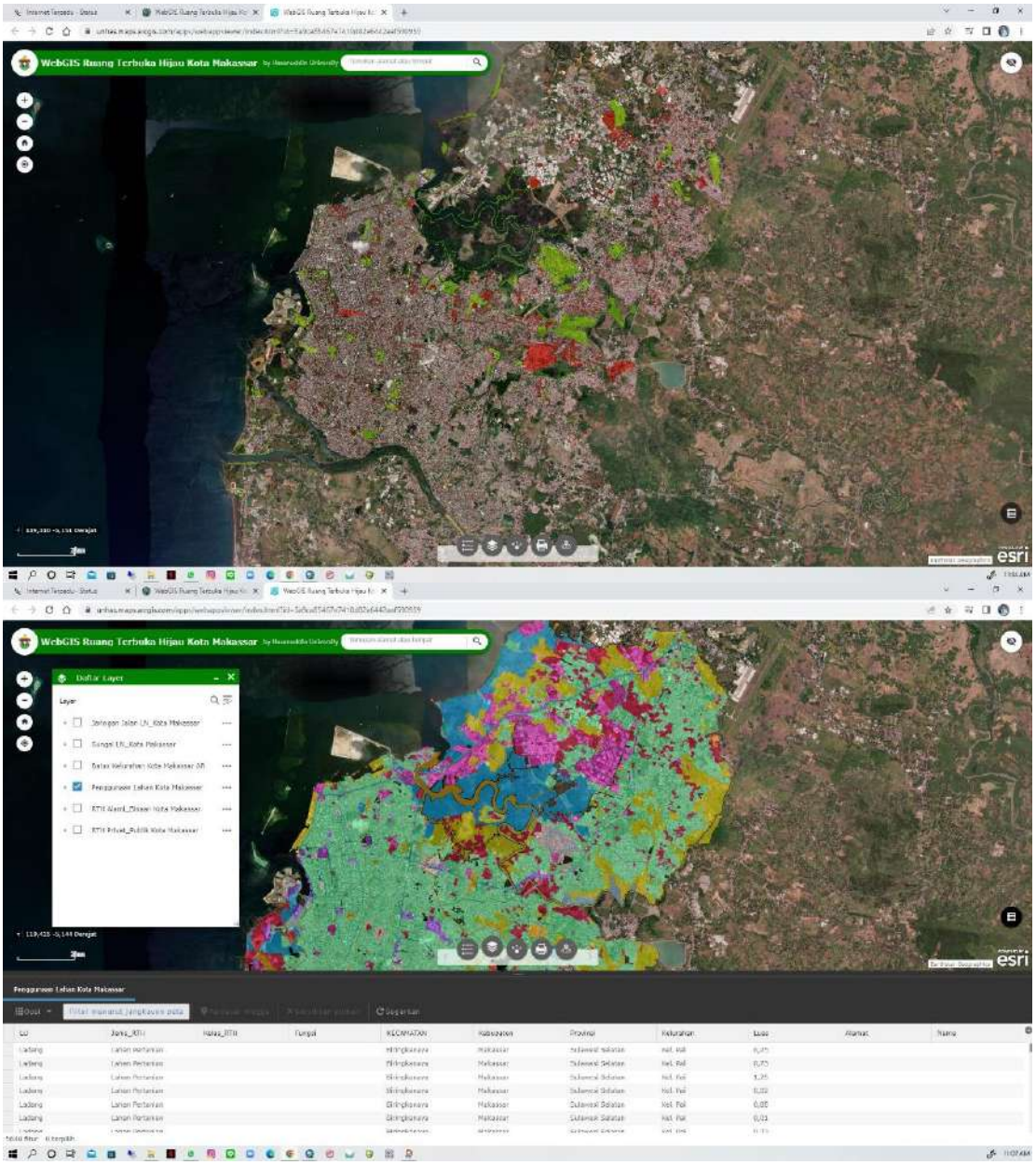

Figure 5. Web View of Makassar City Green Space GIS.

Conclusions

Based on the identification results using Pleiades imagery, the total area of green spaces in Makassar city reached 1603.876 hectares consisting of 719.233 ha of private green spaces and 884.643 ha of public green spaces and based on the identification results, it is known that the Makassar city green space area is 9.08% of the Makassar city area consisting of 4.07% private green space and 5.01% public green space.

Author Contribution

Samsu Arif formulated the title and objectives of the research and made a map of the green open space of Makassar city in the form of webgis. Aswar Syafnur edited, revised the journal, and created a green open space distribution map for Makassar city. Imran Ismail created a research location map and land use map. And the last Aza azzahra and Wikal looked for references and assisted Aswar Syafnur in revising and editing the research results.

Conflict of Interest

All authors must disclose any financial and personal relationships with other people or organizations that could inappropriately influence (bias) their work.

References

Abdillah, M. Z., Nawangnugraeni, D. A., & Yuniarto, A. H. P. (2021). Geographic Information System (GIS) for Mapping Greenpark using Leaflet JS. *Jurnal Teknik Informatika Kaputama (JTIK)*, 5(2), 259–266. https://jurnal-backup.kaputama.ac.id/index.php/JTIK/article/view/604/0

Devi, N. S., & Santosa, P. B. (2022). Analisis Geospasial Perubahan Ruang Terbuka Hijau Wilayah Kota Purwokerto dari Tahun 2013 sampai 2020. *Journal of Geospatial Informatuon Science and Engineering*, 5(2), 121–131. https://doi.org/10.22146/jgise.74620

Dollah, A. S., & Rasmawarni, R. (2019). Struktur Sebaran Ruang Terbuka Hijau di Kota Makassar. *Jurnal Linears*. 2(1), 8–17. https://doi.org/10.26618/j-linears.v2i1.3023

Frizani, D. E., Nugraha, A. L., & Awaluddin, M. (2021). Pengembangan WEBGIS untuk Informasi Kerentanan Terhadap Ancaman Banjir. *Jurnal Geodesi Undip*, 10(2), 11–18. https://ejournal3.undip.ac.id/index.php/geodesi/article/view/30629

Idris, I. S. K., & Mustofa, Y. A. (2021). Monitoring Fasilitas Pertamanan Kota Gorontalo Berbasis Sistem Informasi Geografis. *Jurnal Informatika*. 7(1), 21–26. https://doi.org/10.26877/jiu.v7i1.5858

Imansari, N., & Khadiyanta, P. (2015). Penyediaan Hutan Kota dan Taman Kota sebagai Ruang Terbuka Hijau (RTH) Publik Menurut Preferensi Masyarakat di Kawasan Pusat Kota Tangerang. *Ruang*, 1(3), 101–110. https://ejournal2.undip.ac.id/index.php/ruang/article/view/78

BPK. (2007) *Undang-Undang Republik Indonesia Nomor 26 Tahun 2007 Tentang Penataan Ruang*. https://peraturan.bpk.go.id/Details/39908/uu-no-26-tahun-2007

Kurnianti, R., & Rahmi, D. H. (2020). Ketersediaan Ruang Terbuka Hijau dan Urban Heat Island di Kota Makassar. *Jurnal Litbang Sukowati*, 3(2), 150–163. https://doi.org/10.32630/sukowati.v3i2.78

LAPAN. (2017). *Pleiades: Citra Satelit Resolusi Sangat Tinggi*. https://inderaja-catalog.lapan.go.id/application_data/default/pages/about_Pleiades.html.

Manshur, N. H., Nugraha, A.L., & Firdaus, H. S. (2020). Analisis dan Visualiasi Kesesuaian Ruang Terbuka Hijau

Kota Purwokerto Menggunakan *WEBGIS*. *Jurnal Geodesi Undip*, 9(1), 227–236. https://ejournal3.undip.ac.id/index.php/geodesi/article/view/26167/

Minister of Public Works no 5. (2008). *Peraturan Menteri Pekerjaan Umum Nomor: 05/PRT/M/2008 tentang Pedoman Penyediaan dan Pemanfaatan Ruang Terbuka Hijau di Kawasan Perkotaan*. Direktorat Jenderal Penataan Ruang Departemen Pekerjaan Umum.

Mukhoriyah., Sari, N. M., Sharika, M., & Hanifati, L. N. (2019). Identifikasi Ketersediaan Ruang Terbuka Hijau Kecamatan Kramat Jati Kodya Jakarta Timur Menggunakan Citra Pleiades. *Jurnal Planologi*, 16(2), 158–168.

Noveri, I., Najib, K., & Yusuf, M. (2020). The Analysis of Public Green Open Space Management in Jambi City. *Policy & Governance Review*, 4(3), 182-196. https://doi.org/10.30589/pgr.v4i3.305

Nugrahanto, P. O., Awaluddin, M., & Nugraha, A. L. (2021). Visualisasi Secara Online Ruang Terbuka Hijau Kecamatan Semarang Timur. *Jurnal Geodesi Undip*, 10(1),163–168. https://ejournal3.undip.ac.id/index.php/geodesi/article/view/29637

Prakoso, P., & Herdiansyah, H. (2019). Analisis Implementasi 30% Ruang Terbuka Hijau di DKI Jakarta. *Majalah Ilmiah Globe*, 21(1), 17–26.

Samsudi. (2010). Ruang Terbuka Hijau Kebutuhan Tata Ruang Perkotaan Kota Surakarta. *Journal of Rural and Development*, 1(1), 11–19. https://jurnal.uns.ac.id/rural-and-development/article/view/1836

Setyani, W., Sitorus, S. R. P., & Panuju, D. R. (2017). Analisis Ruang Terbuka Hijau dan Kecukupannya di Kota Depok. *Buletin Tanah dan Lahan*. 1(1), 121–127. https://journal.ipb.ac.id/index.php/btanah/article/view/17701

Sinatra, F., Azhari, D., Asbi, A. M., & Affandi, M. I. (2022). Prinsip Pengembangan Ruang Terbuka Hijau Kota Sebagai Infrastruktur Hijau di Kota Bandar Lampung. *Jurnal Planologi*, 19(1), 19–36.

Yanti, O. S., Purwoko, A., & Lindarto, D. (2023). Adequacy and Suitability of Green Open Space in Medan Kota District. *Jurnal Ilmiah Global Education*, 4(2), 747–758. https://doi.org/10.55681/jige.v4i2.849

Zubair, A. M., Tjaronge, W. M., & Ramli, M. I. (2017). *Pengaruh Ketersediaan Ruang Terbuka Hijau Terhadap Iklim Mikro di Kota Makassar*. https://core.ac.uk/download/pdf/77630754.pdf

Zulkarnaen G, E., Harakan, A., & Hawing, H. (2016). Prinsip-Prinsip Pembangunan Berkelanjutan Dalam Implementasi Pengembangan Ruang Terbuka Hijau di Kecamatan Ujung Pandang Kota Makassar. *Jurnal Ilmu Administrasi*, 5(1), 1–14. https://journal.umgo.ac.id/index.php/Publik/article/view/150

Indexing and Abstracting

GEOFISIKA
UNIVERSITAS HASANUDDIN

ISSN 2579-5546